Investigation and Optimization of Transverse Non-Linear Beam Dynamics in the High-Energy Storage Ring HESR

Dissertation

zur

Erlangung des Doktorgrades (Dr. rer. nat.)

der

Mathematisch-Naturwissenschaftlichen Fakultät

der

Rheinischen Friedrich-Wilhelms-Universität Bonn

vorgelegt von

Dominic Markus Welsch

aus

Bonn

Bonn 2009

Angefertigt mit Genehmigung der Mathematisch-Naturwissenschaftlichen
Fakultät der Rheinischen Friedrich-Wilhelms-Universität Bonn

1. Gutachter: Prof. Dr. Rudolf Maier

2. Gutachter: Prof. Dr. Jens Bisplinghoff

Tag der Promotion: 10.03.2010

Erscheinungsjahr: 2010

To Britta and Max

Abstract

The High-Energy Storage Ring (HESR) is part of the upcoming Facility for Antiproton and Ion Research (FAIR) which is planned as a major extension to the present facility of the Helmholtzzentrum für Schwerionenforschung (GSI) in Darmstadt. The HESR will provide antiprotons in the momentum range from 1.5 to 15 GeV/c for the internal target experiment PANDA. The demanding requirements of PANDA in terms of beam quality and luminosity together with a limited production rate of antiprotons call for a long beam life time and a minimum of beam loss. Therefore, an effective closed orbit correction and a sufficiently large dynamic aperture of the HESR are crucial. With this thesis I present my work on both of these topics.

The expected misalignments of beam guiding magnets have been estimated and used to simulate the closed orbit in the HESR. A closed orbit correction scheme has been developed for different ion optical settings of the HESR and numerical simulations have been performed to validate the scheme. The proposed closed orbit correction method which uses the orbit response matrix has been benchmarked at the Cooler Synchrotron COSY of the Forschungszentrum Jülich.

A chromaticity correction scheme for the HESR consisting of sextupole magnets has been developed to reduce tune spread and thus to minimize the emittance growth caused by betatron resonances. The chromaticity correction scheme has been optimized through dynamic aperture calculations. The estimated field errors of the HESR dipole and quadrupole magnets have been included in the non-linear beam dynamics studies. Investigations concerning their optimization have been carried out. The ion optical settings of the HESR have been improved using dynamic aperture calculations and the technique of frequency map analysis. The related diffusion coefficient was also used to predict long-term stability based on short-term particle tracking.

With a reasonable reduction of the quadrupole magnets field errors and a different choice of tunes, the dynamic aperture was improved by roughly a factor two. The inner area of the dynamic aperture where the particle motion is stable on a long-term scale was increased to include more than 3σ beam size and the specified maximum closed orbit deviations.

Contents

1 Introduction **1**

2 Theory **3**
2.1 Linear beam dynamics 3
2.1.1 Charged particles in electro-magnetic fields 3
2.1.2 Co-moving coordinate system 4
2.1.3 Hamiltonian 4
2.1.4 Multipolar expansion of magnetic fields 6
2.1.5 Linear equation of motion and betatron functions . 7
2.1.6 Matrix formalism 9
2.1.7 Dispersion and Chromaticity 10
2.1.8 Momentum compaction and transition energy . . . 11
2.1.9 Orbit response matrix 12
2.1.10 Influence of electron coolers toroid magnets on closed orbit 14
2.2 Non-linear beam dynamics 16
2.2.1 Symplectic Maps 16
2.2.2 Driving terms 18
2.2.3 Tracking code 20
2.2.4 Dynamic aperture 20
2.2.5 KAM theorem 21
2.2.6 Frequency map analysis 22

3 The High-Energy Storage Ring HESR **24**
3.1 Antiproton beams at FAIR 24
3.1.1 HESR at FAIR 24
3.1.2 Injection chain for antiprotons 25
3.1.3 PANDA experiment 26
3.2 HESR design 27
3.2.1 Layout 27
3.2.2 Magnets 29
3.2.3 Beam parameters 31
3.2.4 Electron cooler 32
3.2.5 Ion optical properties 34
3.3 Comparison with COSY 35

4 Closed orbit correction **38**
4.1 Closed orbit correction system for HESR 38
4.1.1 Alignment errors 38
4.1.2 Simulation of orbit distortions 39
4.1.3 Orbit correction elements 41
4.1.4 Closed orbit correction for HESR 42
4.1.5 Orbit correction including field errors 45
4.1.6 Closed local orbit bumps for HESR 46
4.2 Closed orbit correction at COSY 49
4.2.1 COSY settings 49
4.2.2 Measuring orbit response matrix 49
4.2.3 Comparison of measured and calculated orbit response matrix 50
4.2.4 Orbit correction 51
4.3 Discussion of results 51

5 Dynamic aperture and frequency map analysis **54**
5.1 Dynamic aperture calculations 54
5.2 Arrangement of sextupole magnets for chromaticity correction 55
5.3 Field errors of the HESR magnets 56
5.4 The $\gamma_{tr} = 6.2$ lattice 58
5.4.1 Tune scans 59
5.4.2 Design tunes 63
5.4.3 Optimization 71
5.5 The $\gamma_{tr} = 13.3$ lattice 75
5.5.1 Tune scans 75
5.5.2 Design tunes 75
5.5.3 Optimization 78
5.6 Multipole correction 79
5.7 Discussion of the results 80

6 Summary and outlook **81**

Chapter 1

Introduction

Experiments with particle accelerators have proven to be an essential instrument for nuclear and particle physics to investigate the structure and the interaction of matter. Such investigations are usually based on scattering experiments where particle beams with known energy are directed onto targets where interactions take place. The reaction products can be observed and measured with particle detectors. This information is used to reconstruct the reactions and to determine properties of elementary particles and the underlying interactions in the subatomic regime. The kind of accelerated particles and their energy are determined by experimental setup and the physical process under investigation.

The Facility for Antiproton and Ion Research (FAIR) has been proposed by the Helmholtzzentrum für Schwerionenforschung (GSI) in Darmstadt and will provide a multitude of different particle beams (e.g. antiproton beams, beams with rare isotopes or with heavy ions) for a wide range of scientific experiments [1, 2]. The FAIR project is planned to be a major extension for the present accelerator facility at GSI in which the High-Energy Storage Ring (HESR) [3] is is one of the new particle accelerators dedicated to antiproton physics. It will deliver antiprotons in the momentum range from 1.5 to 15 GeV/c for the internal target experiment PANDA [4]. The institute for nuclear physics (IKP) of the Forschungszentrum Jülich is the leading institute of a consortium which plans the HESR.

For the HESR, a long beam life time and a minimum of beam loss is critical. This is on one hand due to the demanding requirements of PANDA in terms of beam quality and luminosity and on the other due to the use of antiproton beams for which the production rate is a limiting factor. Therefore an effective closed orbit correction and a sufficiently large dynamic aperture are crucial. Investigations and concluding results concerning both topics are covered by this thesis.

In chapter two, the theoretical basis of this thesis is described. A first part of it covers linear beam dynamics. The basic concepts of accelerator physics like twiss parameters and chromaticity are explained. For closed orbit correction, the orbit response matrix method will be used and is therefore discussed together with the ways of its applications. The second part of this chapter is dedicated to non-linear beam dynamics. Driving terms are introduced to explain the influence of magnets on betatron resonances affecting the beam motion. In order to quantify stability of beam motion, the dynamic aperture is extensively used. The calculation of the dynamic aperture is described and the technique of frequency map analysis is introduced which is based on the KAM theorem. The definition of the related diffusion coefficient completes this chapter.

The High-Energy Storage Ring HESR with its internal target experiment PANDA as well as the embedding in FAIR is discussed in chapter three. The HESR layout is described together with the HESR magnets and their alignment. Since PANDA has strong requirements on beam quality and luminosity, the beam parameters and the modes of HESR operation are presented. The ion optical properties of the HESR are listed. Finally, the HESR is compared with the Cooler Synchrotron COSY [5, 6] of the Forschungszentrum Jülich to justify benchmarking experiments.

The fourth chapter deals with closed orbit investigations. Magnet alignment errors are estimated for the HESR to simulate the closed orbit. A closed orbit correction scheme is developed to correct the resulting closed orbit deviations. Numerical simulations are used to validate the closed orbit correction scheme. Local closed orbit bumps are investigated since the transverse position of the antiproton beam and its angle have to be adjustable at various location in the HESR. The measurement of the orbit response matrix at COSY and the results of its application for a closed orbit correction are discussed.

Chapter five contains non-linear beam dynamics studies. A chromaticity correction scheme is developed for the HESR and its optimization is described. The field errors of the main HESR magnets are presented and used for non-linear beam dynamics calculations. The non-linear beam dynamics is investigated for the two main experimental setups of the HESR. This is done by using dynamic aperture calculations and frequency map analysis which are used to optimize the ion optics of the HESR and the field errors of the main HESR magnets.

In the last chapter the results of this thesis are summarized and discussed. An outlook on a possible continuation of this thesis is given.

Chapter 2

Theory

Electro-magnetic fields are used in particle accelerators to guide and accelerate charged particles. Under the assumption of single particle trajectories, which means that no interaction between particles take place, the only forces being considered are those created by the external electromagnetic field of the accelerator. Electric fields are used to accelerate and decelerate particles. To guide a beam of charged particles, electric and magnetic fields can be applied although the use of electric fields is restricted to low beam energies. The motion of particles is solely determined by the setup of the electro-magnetic field of the accelerator and can be classified into linear and non-linear beam dynamics.

2.1 Linear beam dynamics

Linear beam dynamics restricts the influence of electro-magnetic fields to constant or linear forces. Ideally, all particles travelling through an accelerator move on a single trajectory which is solely determined by the setup of the electro-magnetic field of the accelerator. If this reference trajectory is curved, bending forces are necessary to deflect the charged particles. In reality, most particles will not move of the reference trajectory. Therefore, a focussing force has to be applied.

The bending and the focussing forces can be accomplished with electromagnetic fields.

2.1.1 Charged particles in electro-magnetic fields

All electro-magnetic forces acting on charged particles with charge q and velocity $\vec{v}$ are described by the *Lorentz* force

$$\vec{F}_{\text{Lorentz}} = q(\vec{E} + \frac{\vec{v}}{c} \times \vec{B}) \tag{2.1}$$

where the electrical and the magnetic fields are denoted by $\vec{E}$ and $\vec{B}$ and the speed of light by c. The *Lorentz* force is conservative and holds independently of the considered coordinate system.

2.1.2 Co-moving coordinate system

A righthanded and orthogonal co-moving coordinate system (x, y, s) shown in Figure 2.1 is customarily used in accelerator physics [7]. The local curvature of the trajectory is denoted with ρ whereas the angle $\theta = \frac{2\pi}{C}$ corresponds to the angular advance in a ring accelerator with C being its circumference. A trajectory of a single particle can be expressed in deviations from the reference trajectory in all three directions (x, y, s). The horizontal plane is defined to be the (x, s)-plane because particle accelerators are typically built planar.

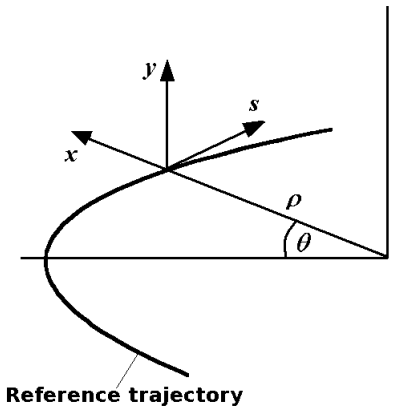

Figure 2.1: Co-moving coordinate system for charged particles in a ring accelerator. The direction of movement is along s. The transverse deviations are given in x and y. The local radius of curvature is denoted by ρ whereas the angular advance is θ.

2.1.3 Hamiltonian

The particle motion is at all times determined by six coordinates consisting of three generalized coordinates $q_i(t)$ and three conjugate momenta $p_i(t)$ where
$i = x, y, s$. All six coordinates define the phase space of the particle motion. If only conservative forces are applied, the phase space volume is constant although not necessarily in the same shape. This is described by Liouville's theorem.

The Hamiltonian $\mathcal{H}(q_i, p_i, t)$ which describes the system under investigation connects the time derivatives of conjugate coordinates:

$$\dot{p} = -\frac{\partial \mathcal{H}}{\partial q}, \; \dot{q} = \frac{\partial \mathcal{H}}{\partial p}. \tag{2.2}$$

These differential equations are known as Hamilton equations.

A charged particle in presence of electro-magnetic fields is influenced by two kinds of potentials: a vector potential $\vec{A}(\vec{q}, t)$ and a scalar potential

$\phi(\vec{q},\, t)$. These potentials are connected to the electrical and magnetic fields by

$$\vec{E} = -\vec{\nabla}\phi - \frac{1}{c}\frac{\partial \vec{A}}{\partial t},\ \vec{B} = \vec{\nabla} \times \vec{A}. \tag{2.3}$$

In the laboratory frame, the Hamiltonian has the following form

$$\mathcal{H}(q_i,\, p_i,\, t) = \frac{1}{2m}\left(\vec{p} - \frac{q}{c}\vec{A}(\vec{q},\, t)\right)^2 + q\phi(\vec{q},\, t). \tag{2.4}$$

If the beam energy is constant and only magnetic fields are used, the Hamiltonian can be restricted to the vector potential. After a transformation of the Hamiltonian to the co-moving frame for which the phase space coordinates are $(x,\, p_x,\, y,\, p_y,\, -p_t,\, ct)^T$ and depend on s, it reads

$$\begin{aligned}\mathcal{H}(x,\, p_x,\, y,\, p_y,\, -p_t,\, ct;\, s) = &-\left[1 + h_{ref}(s)x\right] \\ \times &\left\{\frac{q}{p_0}A(s) + \sqrt{1 - \frac{2}{\beta}p_t + p_t^2 - \left[p_x - \frac{q}{p_0}A_x(s)\right]^2 - \left[p_y - \frac{q}{p_0}A_y(s)\right]^2}\right\}\end{aligned} \tag{2.5}$$

where

$$p_t \equiv -\frac{E - E_0}{p_0 c},\ h_{ref}(s) \equiv \frac{1}{\rho_{ref}(s)},\ \beta \equiv \frac{v}{c} \tag{2.6}$$

and t being the absolute time of flight. Its canonical momentum p_t depends on the difference of particle kinetic energy E and the reference kinetic energy E_0 as well as on the reference momentum p_0. The local radius of curvature along the reference trajectory is denoted with ρ_{ref}. A change of variables to introduce the relative momentum deviation

$$\delta \equiv \frac{p - p_0}{p_0} \tag{2.7}$$

leads to the Hamiltonian

$$\begin{aligned}\mathcal{H}(x,\, p_x,\, y,\, p_y,\, \delta,\, ct;\, s) = &-\left[1 + h_{ref}(s)x\right] \\ \times &\left\{\frac{q}{p_0}A(s) + \sqrt{(1+\delta)^2 - \left[p_x - \frac{q}{p_0}A_x(s)\right]^2 - \left[p_y - \frac{q}{p_0}A_y(s)\right]^2}\right\}\end{aligned} \tag{2.8}$$

where the conjugate coordinate to δ is denoted with T and is given by the canonical transformation

$$-cT = -\frac{\beta\,(1+\delta)\,ct}{\sqrt{1 + \beta^2\,(2\delta + \delta^2)}}. \tag{2.9}$$

This implies that the conjugate coordinate of δ and the time of flight are not equal.

A transformation of variables to the so called action-angle variables J_i and ϕ_i which are defined by

$$J_i = \frac{1}{2\pi} \oint p_i dq_i = const. \tag{2.10}$$

over one oscillation period leads to a Hamiltonian which depends only on the action J_i and not on the angle ϕ_i. The following relations fulfill the last equation

$$\begin{array}{rcl} q_i & = & \sqrt{2J_i} \cdot \cos(\phi_i) \\ p_i & = & -\sqrt{2J_i} \cdot \sin(\phi_i)\,. \end{array} \tag{2.11}$$

2.1.4 Multipolar expansion of magnetic fields

For simplicity, all magnetic fields are assumed to be orthogonal to the direction of movement. This means that all magnets have only transverse components. The vector potential $\vec{A}(x, y, s)$ can be reduced to the longitudinal component $A_s(x, y, s)$. The charge-free *Laplace* equation of this potential A_s in a cylinder symmetrical coordinate system (r, φ, s) is given by

$$\triangle A_s = \frac{\partial^2 A_s}{\partial r^2} + \frac{1}{r}\frac{\partial A_s}{\partial r} + \frac{1}{r^2}\frac{\partial^2 A_s}{\partial \varphi^2} + \frac{\partial^2 A_s}{\partial z^2} \equiv 0. \tag{2.12}$$

The potential can be expanded in a *Taylor* series for $r = 0$ in this coordinate system to

$$A_s(r, \varphi, s) = \frac{cp_0}{q} \sum_{n>0} \frac{1}{n!} A_n(s) r^n e^{in\varphi}. \tag{2.13}$$

The sub index n must be positive to circumvent non-physical singularities for $r \to 0$. The coefficients A_n can be derived from the *Laplace* equation.

The real and the imaginary part represent a solution and they differ by a rotation only. Particle accelerators are typically built planar which motivates the notion of upright (imaginary part) and skewed (real part) magnets. The so called harmonics b_n (imaginary part) and a_n (real part) of a magnetic field are represented by the coefficients $A_n(s) = b_n(s) + ia_n(s)$. The expansion of the magnetic field in harmonics is given by

$$B_y(s) + iB_x(s) = B\rho \sum_{n>0} \left[b_n(s) + ia_{n(s)}\right] \left(re^{i\varphi}\right)^n. \tag{2.14}$$

The sub index n represents a multipole component with $(2n + 2)$ poles and $B\rho = \frac{cp_0}{q}$ is known as magnetic rigidity. Field errors of magnets can also be expressed in harmonics. They are usually given in terms of 10^{-4} and are expanded for a specific radius R_0 [8]

$$B_y(s) + iB_x(s) = 10^{-4} B_{R_0} \sum_{n=0}^{\infty} \left[b_n(s) + ia_n(s)\right] e^{in\varphi} \left(\frac{r}{R_0}\right)^n \tag{2.15}$$

where B_{R_0} is the main magnetic field at the radius of expansion.

For $n = 0$, there is no dependence of the magnetic field on the radius r which refers to a constant magnetic field. The trajectory of a particle travelling through such a magnetic field is bent. This kind of magnetic field is related to a dipole magnet. An ideal upright dipole magnet has a vertical magnetic field component only. For $n = 1$, the magnetic field has a linear dependence on the radius and is related to a quadrupole magnet used to focus the beam. It is evident that an upright quadrupole magnet can focus the beam in one transverse plane only whereas in the other plane the beam is defocused. Therefore at least two quadrupole magnets forming a doublet have to be used to get a net focussing effect in both transverse planes.

Magnetic fields with $n \geq 2$ are related to non-linear beam dynamics. The influence of these magnetic field cannot be avoided in an accelerator since on hand it is not possible to design and build magnets having only one single magnetic field geometry (field errors). On the other hand, higher-order magnetic multipoles may be helpful or even necessary e.g. for chromaticity correction.

2.1.5 Linear equation of motion and betatron functions

The expansion of the *Hamiltonian* to the second order in the vector potential and thus in the magnetic field, neglecting momentum deviations and combining the Hamilton's equations, leads to the homogeneous differential equation of motion[1]

$$u'' + K(s)u = 0 \tag{2.16}$$

where $K(s) = \frac{1}{\rho_u^2(s)} + k_u(s)$ is the local property of the magnets and u a transverse coordinate (x or y). The functions $\rho(s)$ and $k(s)$ are also periodic and depend on the local radius of curvature and the focussing strength. The homogeneous equation of motion is similar to the one of the harmonic oscillator. Thus a periodic solution can be found by the application of the Floquet's theorem with the ansatz [9]

$$u(s) = \sqrt{\varepsilon}\sqrt{\beta_u(s)}\cos(\psi(s) - \psi_{u,0}). \tag{2.17}$$

The integration constants ε and $\psi_{u,0}$ are defined by the system under investigation. The position dependent variable $\beta_u(s)$ is called betatron amplitude. The second order derivative of $u(s)$ reads

$$\begin{aligned} u''(s) = &+\sqrt{\varepsilon}\frac{\beta_u\beta_u'' - \frac{1}{2}\beta_u'^2}{2\beta_u^{\frac{3}{2}}}\cos\left(\psi_u - \psi_{u,0}\right) - \sqrt{\varepsilon}\frac{\beta_u'}{\sqrt{\beta_u}}\sin\left(\psi_u - \psi_{u,0}\right)\psi_u' \\ &- \sqrt{\varepsilon}\sqrt{\beta_u}\sin\left(\psi_u - \psi_{u,0}\right)\psi_u'' - \sqrt{\varepsilon}\sqrt{\beta_u}\cos\left(\psi_u - \psi_{u,0}\right)\psi_u'^2. \end{aligned} \tag{2.18}$$

[1] This kind of equation of motion for periodical systems like accelerator rings are called *Hills* differential equations

Putting both u and u'' into equation 2.16 and sorting for sine and cosine terms, the coefficients have to vanish for all phases:

$$\frac{1}{2}\left(\beta_u\beta_u'' - \frac{1}{2}\beta_u'^2\right) - \beta_u^2\psi_u'^2 + \beta_u^2 K(s) = 0 \tag{2.19}$$

$$\beta_u'\psi_u' + \beta_u\psi_u'' = 0. \tag{2.20}$$

Integrating the latter equation, the phase $\psi_u(s)$ is give by

$$\psi_u(s) = \int_0^s \frac{d\tilde{s}}{\beta_u(\tilde{s})} + \psi_{u,0}. \tag{2.21}$$

The phase difference of two locations is called phase advance. The set of the betatron amplitude[2] β_u, the phase $\psi_u, 0$ and two additional parameters

$$\alpha_u = -\frac{1}{2}\beta_u' \qquad and \tag{2.22}$$

$$\gamma_u = \frac{\left(1+\alpha_u^2\right)}{\beta_u} \tag{2.23}$$

is called "twiss parameters". The twiss parameters describe the motion of particles around the reference trajectory which is called betatron oscillation. For ring accelerators, the number of oscillations per turn is called tune Q_u

$$Q_u = \frac{\psi_{u,ring}}{2\pi} \tag{2.24}$$

where $\psi_{u,ring}$ is the phase advance per turn.

Equation 2.19 can be rewritten in a simplified form:

$$\beta_u'' + 2K\beta_u = 0 \Longleftrightarrow K\beta_u - \gamma_u = \alpha_u'. \tag{2.25}$$

The phase of u and u' has to be eliminated to find the invariant of the particle motion:

$$\gamma_u u^2 + 2\alpha_u u u' + \beta_u u'^2 = \varepsilon_u \tag{2.26}$$

where ε is named *Courant-Snyder* invariant or single particle emittance. This emittance is the invariant of the particle motion and is a conserved quantity for a constant particle energy. The single particle emittance decreases during acceleration and increases during deceleration. This dependence on the particle energy is called adiabatic damping. To compare emittances for different particle energies, an energy-independent emittance $\varepsilon_{u,normalized}$ is introduced

$$\varepsilon_{\mathrm{u,normalized}} = \beta\gamma\varepsilon_u. \tag{2.27}$$

Equation 2.26 corresponds to the equation of an ellipse with the area $\pi\varepsilon$. Figure 2.2 shows the phase space ellipse of the motion of a single particle. The phase space ellipse changes its shape and rotates with the twiss

[2] also called beta function

parameters while the particle moves along its trajectory. A beam emittance can be defined to parametrize an ensemble of particles in a beam. It covers the whole phase space area of all single particle emittances. The emittance of a beam can be specified e.g. in standard deviations or as a 90% beam emittance[3]. The choice strongly depends on the particle distribution of the beam.

The transverse beam width at a location s depends on the transverse beam emittance ε_u and the local beta function $\beta_u(s)$:

$$\sigma_u = \sqrt{\beta_u \varepsilon_u}. \tag{2.28}$$

It can be specified according to the beam emittance and the phase space distribution.

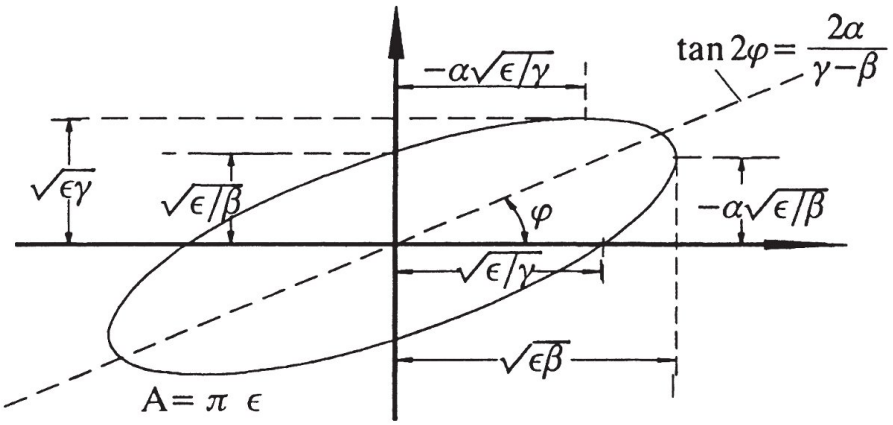

Figure 2.2: Phase space ellipse of the motion of a single particle for one transverse plane. The area A of the phase space ellipse is given by $A = \pi\varepsilon$ where ε is the emittance.

2.1.6 Matrix formalism

The linear transverse equations of motion including momentum deviations in first order can be written as

$$\begin{aligned} x' &= \tfrac{p_x}{1+\delta} + \mathcal{O}(2) \\ p_x' &= \tfrac{1}{\rho(s)}\delta - \left(\tfrac{1}{\rho^2(s)} + k_x(s)\right) x + \mathcal{O}(2) \\ y' &= \tfrac{p_y}{1+\delta} + \mathcal{O}(2) \\ p_y' &= k_y(s) y + \mathcal{O}(2) \end{aligned} \tag{2.29}$$

where a vertical radius of curvature has been assumed to be negligible. A linear transfer map can be constructed by the integration of these equations and represents a linear coordinate transformation. Under the assumption of a stepwise constant Hamiltonian, a matrix representation M

[3] contains 90% of the particles inside the beam

of each element in the accelerator can be found. Symplecticity of these matrix representations is crucial since it guarantees that matrices are energy conserving and do not introduce an artificial energy change during the coordinate transformation. A matrix $\tilde{M}$ is symplectic if it fulfills

$$\tilde{M}S\tilde{M}^T = S \tag{2.30}$$

where

$$S = \begin{bmatrix} 0 & 1 & 0 & 0 \\ -1 & 0 & 0 & 0 \\ 0 & 0 & 0 & 1 \\ 0 & 0 & -1 & 0 \end{bmatrix}. \tag{2.31}$$

The matrix S is the symplectic unit matrix and is a reflection of the structure of the Hamilton's equations.

The concatenation of transfer matrices is performed by the usual matrix multiplication

$$M_{1\to 3} = M_{2\to 3}M_{1\to 2}. \tag{2.32}$$

The concatenation of all matrix representations of a ring accelerator creates the one-turn map. Some of the global properties like the tunes can be derived from this map.

The 4×4 matrices based on equation 2.29 act on the four-dimensional phase space with the coordinates $\vec{x} = (x,\, p_x,\, y,\, p_y)^T$. They are sufficient to describe pure transverse linear motion. The inclusion of longitudinal motion leads to the necessity to increase the dimensionality to 6×6. The 6×6 transfer matrices act on a six-dimensional phase space and a matrix representation of physical elements can be found e.g. in chapter 5 of reference [10].

2.1.7 Dispersion and Chromaticity

The deflection of a particle beam using a dipole magnet is dependent on the momentum. This means that the deflection angle of a dipole magnet is different for each particle in a non-monochromatic[4] beam. The perturbation is given by $\frac{\delta}{\rho}$ where the momentum deviation should be small ($\delta \ll 1$). The linear part of the transverse equation of motion reads

$$u'' + K(s)u = \frac{\delta}{\rho(s)}. \tag{2.33}$$

Particles with a momentum deviation move along dispersion trajectories $x_D = D_x^{(1)}\delta$ where $D_u^{(1)}(s)$ denotes the periodical horizontal[5] linear dispersion function:

$$D_u^{(1)}(s) = \frac{\sqrt{\beta_x(s)}}{2\sin(\pi Q_x)} \oint \frac{\sqrt{\beta_x(\tilde{s})}}{\rho(\tilde{s})} \cos\left(\psi_x(\tilde{s}) - \psi_x(s) - \pi Q_x\right) d\tilde{s}. \tag{2.34}$$

[4] monochromatic: all particles have the same momentum

[5] The vertical dispersion is negligibly small in planar accelerator rings

Also the focussing strength of quadrupole magnets is dependent on the momentum of particles. This momentum dependency leads to changes of the phase advances and in second consequence of the tunes. This effect is the so called natural chromaticity ξ_0 which is given by

$$\xi_{u,0} = \frac{\partial Q_u}{\partial \delta} = -\frac{1}{4\pi} \oint k_u(s)\beta_u(s)ds. \tag{2.35}$$

The momentum spread of the circulating beam introduces a tune spread which can lead to particle loss for example due to resonances. The correction of chromaticities is used on one hand to minimize the induced tune spread and on the other hand to prevent instabilities like the head-tail instability [11]. The most efficient way to correct chromaticity is the use of sextupole magnets [12]. Ideally they are placed close to quadrupole magnets where the chromatic effects occur. A local correction is not always possible for example due to space restrictions or cost-related reasons. A global chromaticity correction can be achieved by sextupole magnets at places with non-zero dispersion:

$$\begin{aligned} \frac{\partial Q_x}{\partial \delta} &= \frac{1}{4\pi} \oint \beta_x(s)r(s)D_x(s)ds \\ \frac{\partial Q_y}{\partial \delta} &= -\frac{1}{4\pi} \oint \beta_y(s)r(s)D_x(s)ds, \end{aligned} \tag{2.36}$$

where $r(s)$ is the sextupole gradient.

2.1.8 Momentum compaction and transition energy

The trajectory of a particle and its length L changes with the particles momentum due to dispersion. The momentum compaction factor α_c is a measure for the relative change of the trajectory length in dependence of the momentum deviation:

$$\alpha_c = \frac{\triangle L/L}{\delta} = \frac{1}{L} \oint \frac{D(s)}{\rho(s)} ds. \tag{2.37}$$

The time T which a particle needs for one turn

$$T = \frac{L}{\beta c} \tag{2.38}$$

is also changed

$$\frac{\triangle T}{T} = \frac{\triangle L}{L} - \frac{\triangle \beta}{\beta} = -\left(\frac{1}{\gamma^2} - \alpha_c\right)\delta \tag{2.39}$$

where $\frac{\triangle T}{T}$ denotes the relative change. This momentum dependence of the travelling time for one turn results in a spread Δf of the revolution frequency $f = \frac{1}{T} = \frac{\beta c}{C}$.

The phase of on-momentum particles and the accelerating radio frequency signal has to be kept fixed to accelerate particles. This boundary condition depends on the revolution frequency f_{RF} of the radio frequency signal, the velocity of particles and is given by

$$f_{RF} = h\frac{\beta c}{C} \tag{2.40}$$

where h is the integer harmonic number which reflects the number of possible bunches in the accelerator. If particles are off-momentum, they oscillate in the longitudinal phase space around the reference phase. This oscillation is called synchrotron oscillation. The phase of the radio frequency signal has to be chosen that off-momentum particles with longer travelling time are affected by a higher acceleration voltage compared to the on-momentum particles and vice versa. This is the so called phase focussing.

The derivative of the revolution frequency with respect to the momentum deviation crosses zero for a certain beam energy which is called transition energy E_{tr}. This non-physical energy is independent of the particle mass and depends only on the ion optics of the accelerator and its geometry. At the transition energy the phase focussing vanishes leading to an increase of the momentum deviation of particles. If the momentum deviation becomes larger than the momentum acceptance of the accelerator, particle loss is inevitable.

The ratio of the transition energy and the particles energy at rest is related to momentum compaction factor by

$$\gamma_{tr} = \frac{E_{tr}}{E_{rest}} = \frac{1}{\sqrt{\alpha_c}}. \tag{2.41}$$

Its value is close to the horizontal tune in case of a regular lattice. The frequency spread of the beam is related to its momentum spread via the so called frequency slip factor

$$\eta = \frac{1}{f_0}\frac{df}{d\delta} = \frac{1}{\gamma^2} - \frac{1}{C}\frac{dC}{d\delta} = \frac{1}{\gamma^2} - \frac{1}{\gamma_{tr}^2}. \tag{2.42}$$

2.1.9 Orbit response matrix

Besides dispersion, other effects like alignment errors or multipole field errors of magnets affect the trajectories of particles, resulting in deviations from the reference trajectory. The trajectory of the reference particle is also deviated but is still closed. Therefore it is called *closed orbit* and all other particles oscillate around this closed orbit.

The method using the orbit response matrix [13] can be used to correct the closed orbit. The matrix entries R_{di} reflect changes of an orbit deviation Δu_d at beam position monitors [14] at location d due to changes

in deflection strength $\Delta\theta'_i$ of orbit correction dipole magnets located at position i and are given by

$$R_{di} = \frac{\Delta u_d}{\Delta\theta'_i} = \sqrt{\beta_{u,i}\beta_{u,d}}\frac{\cos\left(\pi Q_u - \psi_{u,d\to i}\right)}{2\sin\left(\pi Q_u\right)} \tag{2.43}$$

where $\psi_{u,d\to i}$ denotes the phase advance between both locations d and i. For places with a non-zero dispersion, a correction term $-\frac{D_{u,d}D_{u,i}}{\alpha_c C}$ can be added to the right hand side of equation 2.43. D_u denotes the dispersion function, α_c the momentum compaction factor and C the circumference of the accelerator.

The orbit response matrix depends on the transverse tune Q_u, on the beta function β_u at beam position monitors and correction dipole magnets and on the phase differences $\Delta\psi_u$ of their locations. It can either be measured or it can be calculated from a computer model which mathematically describes the particle accelerator under investigation [15].

The orbit response matrix can be used in an iterative process to successively optimize the closed orbit. Its application can be performed in two ways. One possibility is to use the orbit response matrix as it is in an feed-forward process

$$\vec{S} = R \cdot \vec{\Theta} \tag{2.44}$$

where $\vec{S}$ is a vector containing all orbit deviations at beam position monitors and $\vec{\Theta}$ a vector with deflection strengths of orbit correction dipole magnets. The best correction can be achieved by variation of $\vec{\Theta}$ to reproduce the measured orbit deviations at the beam position monitors, e.g. with a χ^2 minimization. Then, the vector $-\vec{\Theta}$ contains the proper settings of all orbit correction dipole magnets to correct the closed orbit deviations. The orbit response matrix can include errors due to measurement errors or due to deviations between the computer model and the real accelerator and explains why an iterative process is recommended. A thorough investigation concerning the comparison of both orbit response matrices (measured and calculated) can lead to an improvement of the accelerator model. The other possibility to apply the orbit response matrix is via its inversion

$$\vec{\Theta} = R^{-1}\vec{S}. \tag{2.45}$$

Each method has its advantages and disadvantages. While the feed-forward method is always applicable, the inversion of R is not. If R is not square or is degenerated, a pseudo-inverse has to be constructed e.g. using SVD[6]. On the other hand side, the inversion has to be calculated once only and matrix vector multiplications should be much faster than variation methods, especially if convergence of the iterative process is slow.

[6] Singular Value Decomposition

2.1.10 Influence of electron coolers toroid magnets on closed orbit

If a beam of ions moves through a particle accelerator, the ions will occupy a certain hypervolume in the multi-dimensional phase space. There exist several techniques to reduce the size of the occupied phase space which are referred as beam cooling [16]. One of this techniques is the electron cooling.

To cool a circulating ion beam, a nearly monochromatic and parallel electron beam is caused to overlap with the ion beam. The velocity of electrons has to match the average velocity of the ions in the circulating beam. If the point of observation is transferred to a frame which moves with the electron velocity, all electrons will be at rest forming a grid. The ions in the circulating beam will pass through the electron beam from all directions and with a variety of velocities. The ions will be affected by Coulomb scattering at the resting electrons and will loose a certain amount of energy which is transferred to the electrons. The loss of energy corresponds to transverse and longitudinal cooling at the rest frame. Ideally, all ions in the circulating beam will have the same velocity and no transverse momentum after the electrons will have been removed. Since the electrons are constantly renewed, the ions are cooled during each passing through the electron cooler.

An electron cooler itself usually consists of an electron gun and a collector (see Figure 2.3) as well as of beam transportation devices. The interaction region where electrons and ions are overlapping is located inside a solenoid magnet which has a longitudinal magnetic field. At both end of the interaction region, there are toroid magnets used to guide the electron beam in and out of the circulating ion beam. Toroid magnets are basically bent solenoid magnets with an additional dipole field to compensation centrifugal force. They affect not only the electron beam but also the circulating ion beam. The deflection is differently large for each transverse direction.

In the following, it is assumed that the toroidal bending is vertical. The equation for the vertical deflection of the circulating beam can be derived from simple geometry [17]:

$$x' = -\frac{B_0 R_e}{B\rho} \ln\cos\left(\varphi_{Toroid}\right) \tag{2.46}$$

where B_0 denotes the toroidal magnetic field strength at the reference radius R_e of the electrons and φ_{Toroid} is the bending angle of the toroid magnet itself. The magnetic rigidity of the circulating ion beam is given by $B\rho$. In addition to the magnetic field of the toroid magnet, the dipole

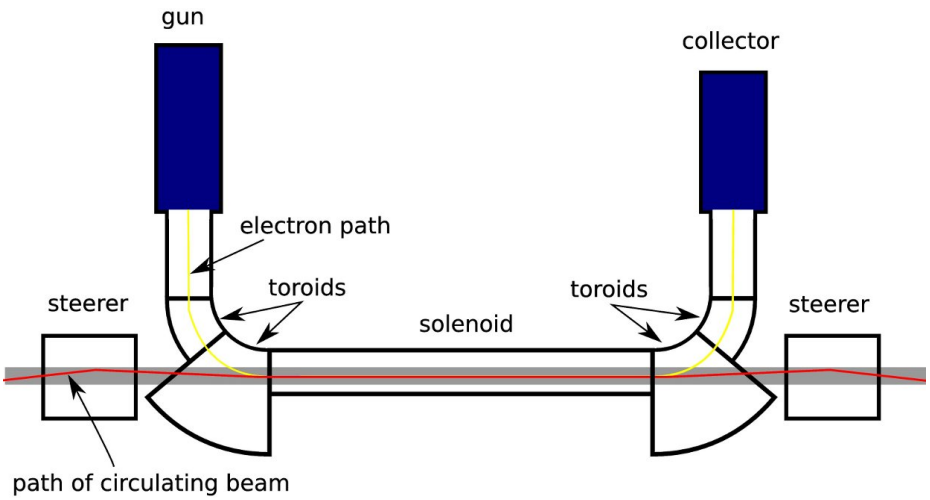

Figure 2.3: Schematic view of an electron cooler. The circulating beam (red) travels from left to right. The electrons of the electron beam (yellow) are generated in the electron gun and accelerated. The electron beam travels through both toroid magnets below the electron gun and the interaction straight inside the solenoid magnet. Behind the latter, the electron beam is bent upwards by the second two toroids, decelerated and dumped in the electron collector. In the lower two toroid magnets, both beams are merged and after the cooling section separated again. These toroid magnet are dimensioned large enough to include the vacuum chamber of the circulating beam (gray). Next to the electron cooler, there are correction dipole magnets (steerer) to correct the deflections of the circulating beam caused by the lower two toroid magnets.

field contributes to the horizontal deflection adding up to

$$y' = \frac{\int B_\perp ds + \int B_{dip} ds}{B\rho} \quad \text{where} \tag{2.47}$$

$$\int B_\perp ds = -\int_0^{\varphi_{Toroid}} \frac{B_0^2 R^2}{B\rho} \ln\left(\cos\left(\varphi\right)\right) d\varphi \quad \text{and} \tag{2.48}$$

$$B_{dip} = \frac{\sqrt{T_e\left(2E_e + T_e\right)}}{qcR} \tag{2.49}$$

where $E_e = m_e c^2$ denotes the electrons energy at rest and T_e their kinetic energy. Whereas the horizontal deflection angle x' scales linearly with the beam momentum via the magnetic rigidity $B\rho = \frac{cp}{q}$, the vertical one does not. The vertical deflection angle y' scale differently since the integral $\int B_\perp ds$ depends on the magnetic rigidity itself.

2.2 Non-linear beam dynamics

The stability of the particle motion is of major importance. Particle motion can become non-linear e.g. in presence of higher-order multipoles like the necessary sextupole magnets or field errors. These non-linearities make the beam behavior unpredictable and lead to the necessity of particle tracking. Furthermore, the higher-order multipoles can drive resonances which restrict the area of stable motion in phase space. Generally, dynamic aperture calculations are used to find the stable area in multi-dimensional phase space.

2.2.1 Symplectic Maps

A more generalized form of transport matrices are transfer maps which are not necessarily linear and per definition symplectic.

The Poisson bracket which is defined by

$$[f(\vec{x}),\, g(\vec{x})] \equiv \sum_{i=1}^{n} \left[\frac{\partial f(\vec{x})}{\partial x_i} \frac{\partial g(\vec{x})}{\partial p_i} - \frac{\partial f(\vec{x})}{\partial p_i} \frac{\partial g(\vec{x})}{\partial x_i} \right]. \tag{2.50}$$

can be used to express the total time derivative for any function $f(\vec{x}; s)$ of the phase space variables $\vec{x} = (x,\, p_x,\, y,\, p_y,\, \delta,\, ct)^T$ as

$$\frac{df(\vec{x})}{ds} = -\,[\mathcal{H},\, f(\vec{x}; s)] + \frac{\partial f(\vec{x}; s)}{\partial s} \tag{2.51}$$

where time was replaced by s and $\mathcal{H}$ denotes the Hamiltonian. The total time derivative is reduced to the Poisson bracket solely

$$\frac{df(\vec{x})}{ds} = -\,[\mathcal{H},\, f(\vec{x}; s)] \tag{2.52}$$

if the function $f(\vec{x}; s)$ is not explicitly dependent on s. One important feature of the Poisson bracket is the invariance under canonical transformations (e.g. to action-angle variables $[J, \phi]$). The Poisson bracket posses also the three properties which define a Lie algebra [18]: it is antisymmetric and distributive and also fulfills the Jacobi's identity. Thus it can be written in Lie operator form

$$: f(\vec{x}) : g(\vec{x}) \equiv [f(\vec{x}),\, g(\vec{x})] \tag{2.53}$$

which changes equation 2.52 to

$$\frac{df(\vec{x})}{ds} = - : H : f(\vec{x}). \tag{2.54}$$

It can be shown that two Lie operators are equal if the underlaying functions only differ by an arbitrary constant. Thus the Lie operators also form a Lie algebra.

A map acting on functions (of phase space coordinates) for a Hamiltonian which commutes at different times can be expressed as

$$\mathcal{M}_{\vec{\xi}_{0\to 1}} = \exp\left(: -\int_{s_0}^{s_1} \mathcal{H}(s)ds :\right) \tag{2.55}$$

since the Hamiltonian is the generator of an infinitesimal coordinate transformation. The corresponding transfer map $\vec{\xi}$ acting on phase space coordinates is given by

$$\vec{x}_1 = \vec{\xi}_{0\to 1}(\vec{x}_0) \tag{2.56}$$

Assuming a stepwise constant Hamiltonian, a functional map of an element with length L reads

$$\mathcal{M}_{\vec{\xi}_{0\to 1}} = \exp\left(: -L\mathcal{H} :\right). \tag{2.57}$$

Concatenation of functional transfer maps is done in reverse order compared to concatenation of transfer matrices

$$\mathcal{M}_{\vec{\xi}_{0\to 1}}\mathcal{M}_{\vec{\xi}_{1\to 2}} \equiv \mathcal{M}_{\vec{\xi}_{0\to 2}}. \tag{2.58}$$

Non-linearities are introduced by thin non-linear kicks. A kick describes the transfer between transverse and longitudinal momenta induced by a magnetic field. "Thin" means in this context that the length of the magnetic field is infinitesimally small. The thin non-linear kicks are connected by linear maps. A one-turn functional map looks then like

$$\mathcal{M}_{\vec{\xi}_{0\to n}} = \mathcal{M}_{\vec{\xi}_{0\to 1}} e^{:V_1:}\mathcal{M}_{\vec{\xi}_{1\to 2}} e^{:V_2:}\mathcal{M}_{\vec{\xi}_{2\to 3}} \dots e^{:V_{n-1}:}\mathcal{M}_{\vec{\xi}_{n-1\to n}} \tag{2.59}$$

where V_i represent a thin non-linear kick at position i and n is the number of elements in the accelerator. With the introduction of

$$\hat{V}_i \equiv \mathcal{A}_0\mathcal{M}_{\vec{\xi}_{0\to i}} V_i = \mathcal{R}_{0\to i} V_i, \tag{2.60}$$

all thin kicks can be shifted to the beginning of the lattice. The operator $\mathcal{R}$ is the rotation operator. The one-turn map reads then

$$\mathcal{M}_{\vec{\xi}_{0\to n}} = \mathcal{A}_0^{-1} e^{:\hat{V}_1:} e^{:\hat{V}_2:} \dots e^{:\hat{V}_{n-1}:}\mathcal{R}_{0\to n}\mathcal{A}_n. \tag{2.61}$$

After that, all thin kicks can be lumped into a single kick by the Baker-Campbell-Hausdorff (BCH) theorem for non-commuting operators

$$e^a e^b = e^{a+b+[a,\,b]/2+\dots} \tag{2.62}$$

and the one-turn map finally looks like

$$\begin{aligned}\mathcal{M}_{\vec{\xi}_{0\to n}} &= \mathcal{A}_0^{-1} e^{:h:}\mathcal{R}_{0\to n}\mathcal{A}_n \\ &= \mathcal{A}_0^{-1} \exp\left(: \sum_{i=1}^{N} \hat{V}_i + \frac{1}{2}\sum_{i<j}^{N} \left[\hat{V}_i,\, \hat{V}_j\right] + \dots :\right) \mathcal{R}_{0\to n}\mathcal{A}_n\end{aligned} \tag{2.63}$$

2.2.2 Driving terms

The driving terms represent the contribution of multipoles to specific effects, e.g. betatron resonances. To exemplify driving terms, they will be derived for sextupole magnets in first order concerning their contribution to the sextupole betatron resonances.

The vector potential for a thin sextupole magnet is given by

$$V_i = \frac{q}{p_0} A_s\left(s_i\right) = -\frac{b_{2,i}}{3}\left(x^3 - 3xy^2\right) \tag{2.64}$$

where s_i is an arbitrary location. The thinness of sextupole magnets implies a step wise constant potential $A_s\left(s_i\right)$. With

$$\mathcal{A}_i x = \sqrt{\beta_{x,i}} x + D_{x,i}^{(1)} \delta \tag{2.65}$$

where $D_x^{(1)}$ represents the first-order horizontal dispersion, the transformation acts like

$$\begin{aligned} \tfrac{1}{3}\mathcal{A}_i(x^3 - 3xy^2) &= \tfrac{1}{3}\sqrt{\beta_{x,i}}\left(x + D_{x,i}^{(1)}\delta\right)^3 - \left(\sqrt{\beta_{x,i}}x + D_{x,i}^{(1)}\delta\right)\beta_{y,i}y^2 \\ &= \sqrt{\beta_{x,i}}\left(D_{x,i}^{(1)}\right)^2 x\delta^2 + \tfrac{1}{3}\beta_{x,i}^{3/2}x^3 - \sqrt{\beta_{x,i}}\beta_{y,i}xy^2 \\ &\quad + \left(\beta_{x,i}x^2 - \beta_{y,i}y^2\right) D_{x,i}^{(1)}\delta + \mathcal{O}(\delta^3). \end{aligned} \tag{2.66}$$

There are no terms with first-order vertical dispersion. The eigenvalues of the rotational operator $\mathcal{R}$ in terms of a resonance basis

$$h_x^{\pm} \equiv \sqrt{2J_x} e^{\pm i\phi_x} = x \mp i p_x \tag{2.67}$$

are

$$\mathcal{R}_{i\to j} h_x^{\pm} = \mathcal{R}_{i\to j}\sqrt{2J} e^{\pm i\phi_x} = \sqrt{2J} e^{\pm i(\phi_x + \psi_{i\to j,\,x})} = e^{\pm i\psi_{i\to j,\,x}} h_x^{\pm} \tag{2.68}$$

where $\psi_{i\to j}$ is the phase advance between locations i and j. Expressing x and y in terms of the resonance basis, applying the rotational operator, and sorting for orders in x and y delivers

$$\begin{aligned} \mathcal{R}_{0\to i}x &= \tfrac{1}{2}\left(h_x^+ e^{i\psi_{xi}} + c.c.\right), \\ \mathcal{R}_{0\to i}x^2 &= \tfrac{1}{4}\left(h_x^{+2} e^{i2\psi_{xi}} + c.c. + 4J\right), \\ \mathcal{R}_{0\to i}x^3 &= \tfrac{1}{8}\left(h_x^{+3} e^{i3\psi_{xi}} + 3h_x^{+2}h_x^- e^{i\psi_{xi}} + c.c.\right), \\ \mathcal{R}_{0\to i}xy^2 &= \tfrac{1}{8}\left(h_x^+ h_y^{+2} e^{i(\psi_{xi}+2\psi_{yi})} + h_x^+ h_x^{-2} e^{i(\psi_{xi}-2\psi_{yi})}\right. \\ &\quad \left. + 2h_x^+ h_y^+ h_y^- e^{i\psi_{xi}} + c.c.\right). \end{aligned} \tag{2.69}$$

The Lie generator $:h:$ can be determined to have in first-order the following form

$$h^{(1)} \equiv \sum_{|\bar{I}|} h_{\bar{I}} h_x^{+i_1} h_x^{-i_2} h_y^{+i_3} h_y^{-i_4} \delta^{i_5} \tag{2.70}$$

where $\bar{I} = [i_1, i_2, i_3, i_4, i_5]$ and $\left|\bar{I}\right| \equiv i_1 + i_2 + i_3 + i_4 + i_5$. The first-order driving terms can be extracted by comparison of equations 2.66 and 2.69 and collecting geometric[7] terms. The geometric driving terms are

$$\begin{array}{rcrcl} h_{21000} & = & h^*_{12000} & = & -\frac{1}{8}\sum_{i=1}^{N}(b_{2,i}L)\beta_{x,i}^{3/2}e^{i\psi_{x,i}}, \\ h_{30000} & = & h^*_{03000} & = & -\frac{1}{24}\sum_{i=1}^{N}(b_{2,i}L)\beta_{x,i}^{3/2}e^{i3\psi_{x,i}}, \\ h_{10110} & = & h^*_{01110} & = & \frac{1}{4}\sum_{i=1}^{N}(b_{2,i}L)\beta_{x,i}^{1/2}\beta_{y,i}e^{i\psi_{x,i}}, \\ h_{10200} & = & h^*_{01020} & = & \frac{1}{8}\sum_{i=1}^{N}(b_{2,i}L)\beta_{x,i}^{1/2}\beta_{y,i}e^{i(\psi_{x,i}+2\psi_{y,i})}, \\ h_{10020} & = & h^*_{01200} & = & \frac{1}{8}\sum_{i=1}^{N}(b_{2,i}L)\beta_{x,i}^{1/2}\beta_{y,i}e^{i(\psi_{x,i}-2\psi_{y,i})}. \end{array} \tag{2.71}$$

The driving terms marked with an asterisk are the complex conjugates. Since driving terms are in general complex numbers, the individual contribution of all sextupole magnets is as well. Thus the driving terms can be written as

$$h_{jklmq} = \sum_{i=1}^{N} A_{jklmq,i}e^{i\phi_{jklm,i}} \tag{2.72}$$

where $A_{jklmq,i}$ and $\phi_{jklm,i}$ represent the amplitude and the phase of the driving term at the locations of the sextupole magnets. The indices are related to their dependencies e.g. on the beta functions or on the betatron phases

$$\begin{array}{rcl} A_{jklmq,i} & \propto & \beta_{x,i}^{(j+k)/2}\beta_{y,i}^{(l+m)/2}\left(D_{x,i}^{(1)}\right)^q \\ \phi_{jklm,i} & \propto & (j-k)\,\psi_{x,i} + (m-l)\,\psi_{y,i}. \end{array} \tag{2.73}$$

Driving terms with $q > 0$ are chromatic ones. For example, the driving terms h_{11001} and h_{00111} depend linearly on dispersion and beta functions, but not on the betatron phases. Both driving terms are related to chromaticity and reflect equations 2.36. Driving terms are geometric for $q = 0$. Those have pure oscillatory character and drive betatron resonances. The frequencies of the resonances are determined by the other four indices with

$$(j-k)\cdot Q_x + (l-m)\cdot Q_y \tag{2.74}$$

Considering this, the driving terms in equation 2.71 contribute to betatron resonances with the frequencies:

$$Q_x,\ 3Q_x,\ Q_x,\ Q_x + 2Q_y,\ Q_x - 2Q_y. \tag{2.75}$$

All of these driving terms are first-order driving terms only. According to BCH theorem and the corresponding expansion of the symplectic map in equation 2.63, two sextupolar potentials and thus driving terms contribute in second order to octupole resonances and so forth.

[7] non-chromatic

2.2.3 Tracking code

Tracking codes are used to simulate particle trajectories. They are based on transfer maps either linear or non-linear. The maps have to be symplectic to track particles in a realistic way without an artificial and non-physical energy change. They represent a physical element or if concatenated even whole sections of an accelerator. Such a transfer map performs a coordinate transformation and lets a particle or a bunch of particles "travel" through an accelerator. In between two adjacent coordinate transformations certain actions can be performed for example calculation of space charge forces[8] [19] or application of non-linear kicks.

The tracking code which has been used for this thesis is named SIMBAD [20] and it is based on ORBIT [21].

SIMBAD SIMBAD is a symplectic tracking code which uses linear maps. It is able to read transfer matrices produced by the linear modelling code MAD[9] version 8 [22] or X [23]. SIMBAD tracks six-dimensional phase space coordinates using these matrices. Non-linearities are included by non-linear kicks performed between coordinate transformations. These non-linear kicks represent field errors and sextupole magnets. Furthermore phase space coordinates can be dumped into an output file. Those turn by turn data can be analyzed afterwards (e.g. with frequency map analysis). SIMBAD is written in C++ with a modular structure and is therefore designed to be extendable. To speed up computation, SIMBAD uses an implementation of the message passing interface (MPI) standard to run on multiple cores, processors and/or computers.

2.2.4 Dynamic aperture

The dynamic aperture is commonly referred as the transition border from regular, stable motion to irregular, unstable or chaotic motion. Symplectic tracking codes are used to find the trajectories of particles over a certain number of turns. The dynamic aperture is mostly defined as the border of multi-dimensional phase space area of the starting coordinates of particles which survive a predefined number of turns [24]. The number of turns which particles have to survive is related to the time scale. For the so called short-term dynamic aperture, it is sufficient to track several hundred up to a few thousand turns to observe betatron resonances [25] arising. Betatron resonances are commonly referred by the condition

$$m \cdot Q_x + n \cdot Q_y = p \tag{2.76}$$

where m, n, and p have to be integer and the resonance order is given by $|m| + |n|$. Resonances with n being even are commonly referred as

[8] Force of charged particles acting on other charged particles within the beam or bunch

[9] Methodical Accelerator Design

normal or upright whereas with n being odd as skew resonances. Since the resonances are tune dependent, they can be drawn in a tune diagram in which the vertical tune is plotted against the horizontal one. The density of resonances in the tune diagram can be reduced by the introduction of symmetry to the accelerator lattice [26], i.e. some resonances can be suppressed. For an accelerator lattice with M equal periods, the integer p in the resonance condition can be replaced by $p = M \cdot r$ where r has also to be integer. The long-term dynamic aperture is typically in the order of 10^9 turns to proof long-term stability. The long-term dynamic aperture has according to the Nekhoroshev theorem an inverse logarithmic dependence on the number of turns ([27, 28]).

For all dynamic aperture calculations, computation time is the major restriction. Starting particles in a dense six-dimensional phase space over several million turns can easily take weeks, months or even years. Thus, a proper choice of starting coordinates is inevitable. There is a trade-off between accuracy (number of particles, density of phase space coordinates), number of turns, and computation time.

There are other approaches which help to find limiting resonances, for example the analysis of resonance driving terms or the frequency map analysis.

2.2.5 KAM theorem

The KAM theorem goes back to the work of **K**olmogorov, **A**rnold, and **M**oser [29]. For a system which can be described by a Hamiltonian $\mathcal{H}$ with an integrable part $\mathcal{H}_0$ and a small perturbation $\varepsilon\mathcal{H}_1$ the KAM theorem states that the motion is regular and confined to so called KAM tori if three conditions are fulfilled [30]:

1. Linear independence of frequencies $\omega_i = \frac{\partial \mathcal{H}}{\partial J_i}$
2. Smoothness condition of the perturbation [31]
3. Sufficient distance of initial condition from a resonance

The KAM tori can be observed in phase space as circles if the scales of the axes are properly chosen and the motion is regular. If a perturbation is present and small enough to fulfill the three conditions, the KAM tori will be deformed. Such a deformation can be e.g. triangular for sextupolar perturbations.

In a phase space plot of a disturbed motion, three regions can be identified. The inner region of stable motion is filled with KAM tori. Islands which represent fixpoints of the motion can appear in this stable region between the KAM tori. Inside those thin chaotic layers, conditions three is violated. Further outside, there is a transition to the second region of chaotic motion. In this region the second and the third condition is violated and no KAM tori can be observed. Islands can appear at

fixpoints. The last transition to the region of unbound motion is reached if condition one is not fulfilled.

There are in principle two kinds of fixpoints: elliptic and hyperbolic ones. Elliptic fixpoints are stable and particles are able to reach them forming islands potentially surrounded by KAM tori. The hyperbolic fixpoints are unstable forming empty spots.

2.2.6 Frequency map analysis

Although the frequency map analysis was developed for celestial mechanics, it is now widely used for studies from atomic physics [32] to galactical dynamics [33] and nowadays even in accelerator physics [26]. This technique is based on a revised Fourier analysis which constructs the so-called frequency map from the space on initial conditions to the tune space. To do this, the NAFF algorithm [34] or a variant of it like SUSSIX [35] searches for quasiperiodic approximation of the transverse motion over a finite time span or turns T. Starting a particle with two initial conditions ($x'_0 = y'_0 = 0$), the discrete trajectory is recorded in a four-dimensional surface of section $x(t)$, $x'(t)$, $y(t)$, $y'(t)$. Applying the refined Fourier technique, the quasiperiodic approximation, truncated to order N, of the form $z_w(t) = w(t) + iw'(t)$ reads

$$z_u(t) = a_u e^{iQ_u t} + \sum_{k=1}^{N} a_{\vec{m}_k} e^{i<\vec{m}_k, \vec{Q}>t},$$

where $\vec{Q} = (Q_x, Q_y, 1)$ is the fundamental frequency vector, $\vec{m}_k = (m_{1k}, m_{2k}, m_{3k})$ is a multi-index, $< \vec{m}_k, \vec{Q} >= m_{1k}Q_x + m_{2k}Q_y + m_{3k}$, and the complex amplitude $a_{\vec{m}_k}$ is ordered by decreasing magnitudes.

The frequency map F^T itself is defined as the mapping of initial coordinates to the transverse tunes

$$\begin{array}{rccc} F^T: & \mathbb{R}^2 & \rightarrow & \mathbb{R}^2 \\ & (x,\, y) & \mapsto & (Q_x,\, Q_y). \end{array} \tag{2.77}$$

The initial transverse momenta can be neglected and thus arbitrarily chosen (e.g. $x'_0 = y'_0 = 0$) because the image of F^T is largely independent of them in the frequency plane [36]. The revised Fourier technique converges with $1/T^4$ [26] when a Hanning window is applied [37] (FFT converges with $1/T$ [38]). That reduces the number of turns necessary to the convergence to typically 1000, which saves computation time considerably.

If the approximation is a regular KAM solution, the frequency map F^T is invariant by time translations which means that the tunes are fixed over time. If this is not the case, the time variation of the tunes is related to the orbit diffusion[10] and hence can be used as a stability criterion. Thus

[10] The general term is Arnold diffusion

the study of the regularity of the frequency map can provide information about resonances and non-linear behavior.

A stability criterion or a measure of stability related to the orbit diffusion is the so called diffusion coefficient D. The diffusion coefficient is defined as the root mean square of tune differences of two adjacent finite periods of time (e.g. 1000 turns)

$$D = \log_{10}\left[\sqrt{\left(Q_x^{(2)} - Q_x^{(1)}\right)^2 + \left(Q_y^{(2)} - Q_y^{(1)}\right)^2}\right] \tag{2.78}$$

where Q_x and Q_y are the transverse tunes calculated from (1) the first time period and (2) the second time period. A diffusion coefficient of $D \leq -7$ is considered to belong to stable motion whereas a diffusion coefficient of $D \geq -2$ is related to strongly chaotic and unbound motion [39].

Chapter 3

The High-Energy Storage Ring HESR

The High-Energy Storage Ring HESR is part of the upcoming Facility of Antiproton and Ion Research at the Helmholtzzentrum für Schwerionenforschung and is dedicated to antiproton physics. It is a ring accelerator which is able to store, accelerate and provide antiprotons in a momentum range from 1.5 to 15 GeV/c for the internal target experiment PANDA [40, 4]. The HESR is designed by a consortium. Its members are Institut für Kernphysik at Forschungszentrum Jülich (Germany) as leading laboratory, GSI in Darmstadt (Germany), The Svedberg Laboratory in Upsala (Sweden), Soltan Institute for Nuclear Studies in Warsaw (Poland), CAD/CAM Engineering Center in Tbilisi (Georgia), National Institute for Research and Development in Electrical Engineering ICPE-CA in Bucharest (Romania), and IAP in Sumy (Ukraine).

3.1 Antiproton beams at FAIR

As the name states, a whole branch of the Facility for Antiproton and Ion Research is dedicated to antiproton physics from production over storage to experimental use. A central part of this branch is the HESR with its internal target experiment PANDA.

3.1.1 HESR at FAIR

FAIR is an international project and will be a major extension of the present facility of the Helmholtzzentrum für Schwerionenforschung (GSI) in Darmstadt. It offers forefront science for European and international users in various fields which include radioactive ion beams, antiproton physics, compressed baryon matter, plasma physics, and atomic physics. The new facility itself consists of different experimental sites which enable unprecedented experimental possibilities. A schematic overview is shown in Fig. 3.1.

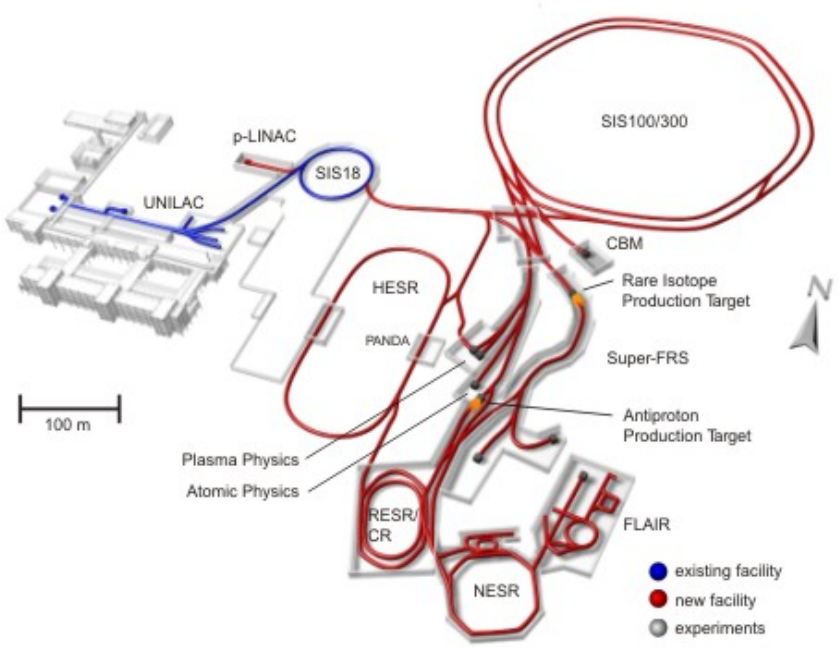

Figure 3.1: Schematic view of the FAIR site. The new accelerators are drawn in red, the present GSI accelerators in blue and experiments in gray. Important for the HESR are the following parts in the injection chain: p-LINAC, SIS18, SIS100, antiproton production target, CR, RESR. The HESR is aligned along an north-south axis. On the right hand side of the HESR, there is the PANDA experiment. The gray building on the left hand side of the HESR will house the electron cooler. The upper direct injection way from the SIS18 to the HESR is a possible upgrade which will allow the operation with protons moving in the opposite direction of antiprotons.

The international PANDA collaboration with a rich scientific program is working on a new experiment with antiprotons in the energy range between the Anti-Proton Decelerator AD [41] and the Tevatron [42] regime. The HESR with its special equipment like multi harmonic radio frequency cavities [43], electron cooling [44] and stochastic cooling devices [45] make high precision experiments feasible which have not been possible before. Besides PANDA, other experimental groups namely PAX and ASSIA expressed their interest in using the HESR for spin physics related experiments [46, 47, 48]. Thus, sufficient space is reserved in the HESR design to allow an upgrade for polarized beams [49, 50].

3.1.2 Injection chain for antiprotons

A high-intensity proton beam of $35\,mA$ and pulse length of $36\,\mu s$ is accelerated in the new proton linac [51] to $70\,MeV$. The repetition rate is $4\,Hz$. The proton beam is then injected into the existing SIS18 [52].

Per cycle, roughly $2 \cdot 10^{12}$ protons are accelerated to $2\,GeV$ and then injected into SIS100 [53]. After a stacking of eight injections from SIS18, up to $4 \cdot 10^{13}$ protons per cycle are accelerated to an energy of $29\,GeV$. Afterwards the bunches are compressed to $25\,ns$, ejected, and shot on an antiproton production target [54]. The beam guiding system behind the antiproton production target is capable of transporting antiprotons with a beam energy of $3\,GeV$ and a maximum relative momentum spread of $\Delta p/p = 3\%$ which corresponds to approximately $2 \cdot 10^8$ antiprotons. The antiprotons are separated and guided to the collector ring CR [55] where the antiprotons are collected and beam cooled for $10\,s$ using a stochastic cooling system to reduce the beam emittance. After the beam cooling, the beam is rotated in the longitudinal phase space (bunch rotation) to achieve a lower momentum spread. The cooled and rotated antiproton beam is then injected into the RESR [56] where it is further cooled using the RESR stochastic cooling system. The described injection chain can provide antiprotons with a production rate of $\dot{N}_{\bar{p}} = 2 \cdot 10^7\,s^{-1}$.

3.1.3 PANDA experiment

PANDA (Anti**P**roton **An**nihilation at **Da**rmstadt) is a universal detector and will be used to study interactions between antiprotons and fixed target protons and nuclei over the whole momentum range of the HESR. The target is planned to be a frozen H_2 pellet jet target. The scientific program of the PANDA collaboration includes several measurement which will address fundamental questions of QCD mostly in the non-perturbative regime [4].

The study of QCD bound states is of fundamental importance as it will help to improve the quantitative understanding of the theory. Precision measurements are necessary to distinguish between different approaches. The PANDA measurements include charmonium, D meson and baryon spectroscopy. This will be carried out by the study of the creation mechanism of quark-antiquark pairs and their arrangement to hadrons. Also hadrons in nuclear matter are part of the PANDA physics program. The origin of hadron masses in the context of spontaneous chiral symmetry breaking in QCD is going to be studied by medium modifications of hadrons embedded in hadronic matter. Part of this investigation is also related to the partial restoration of the chiral symmetry in hadronic matter. Since earlier experiments related to this topic have been restricted to the light quark sector, PANDA is an extension to the charm sector for hadron with open and hidden charm. PANDA also competes with planned dedicated hypernuclei facilities. The availability of antiprotons beams at FAIR will allow an efficient way to produce hypernuclei with more than one strange hadron which opens new perspectives for nuclear structure spectroscopy. Also the study of forces between hyperons and a nucleus is planned. The possibility of high-intensity antiproton beam in

the HESR allows the production of large numbers of D-mesons which can be used to observe rare weak decays to study electroweak physics.

All measurements will profit firstly from the high yield of antiprotons induced reactions and secondly from the fact that all non-exotic quantum number combinations for directly formed states are allowed, whereas states with exotic quantum number can be observed in production. Significant progress beyond the present understanding of all topics is expected due to improvements in statistics and precision of the data.

3.2 HESR design

The HESR is designed as a storage ring with a racetrack shape. Its magnetic rigidity ranges from 5 to 50 Tm which corresponds to the momentum range of 1.5 to 15 GeV/c. With its circumference of 575 m it covers an area of 120 m by 250 m.

3.2.1 Layout

The HESR layout is shown in Figure 3.2. Both arcs have a length of 155.5 m. They are designed to be symmetric. The straight sections have a length of roughly 132 m. Each straight section has a larger installation, namely the electron cooler and the PANDA experiment with target, and are therefore named after those.

Target straight section The target straight section will house the internal experiment PANDA with its target and other experimental installations. For detection purposes, the target will be embedded inside of a solenoid magnet. Another solenoid magnet will be installed in front of the target solenoid magnet for compensation purposes. A large aperture dipole magnet is part of the experimental installations of PANDA to separate secondary particles at small laboratory angles. This PANDA dipole magnet affects not only the charged particles created by reactions of the antiprotons at the target but also the circulating antiproton beam. Therefore, a chicane including two additional dipole magnets is necessary to compensate the deflections of the PANDA dipole magnet. Furthermore, parts of the stochastic cooling namely the pick-ups as well as the injection equipment and the accelerating radio frequency cavities will be installed in the target straight section. There are two injection points planned. The first one will be used to inject protons and antiprotons from the RESR. The second injection from SIS18 which is planned as an upgrade which allows protons to circulate in the opposite direction without changing the polarity of the magnets installed in the HESR.

Cooler straight section The electron cooler will be part of the other straight section. At both ends of the electron cooler, compensation solenoid

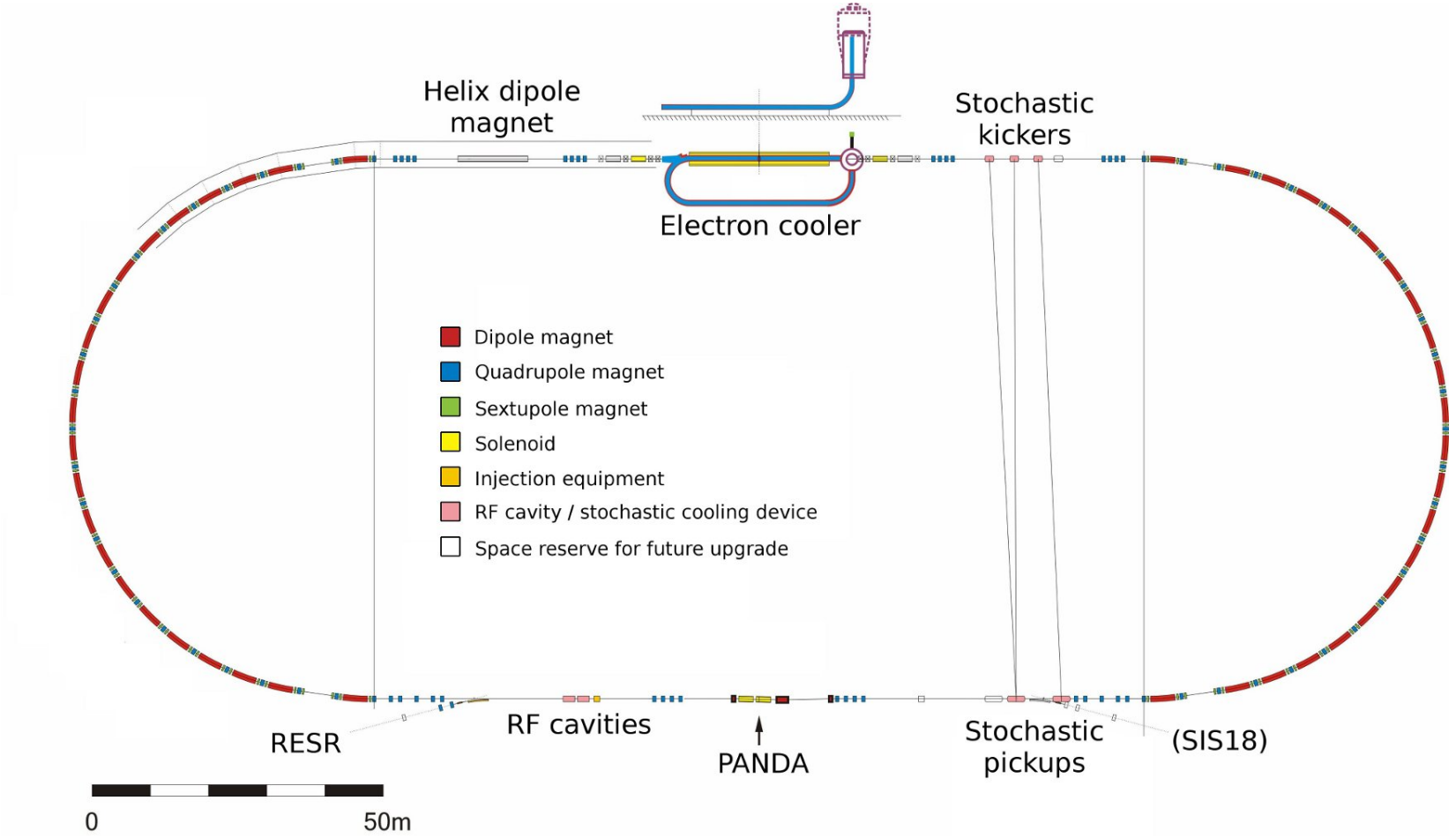

Figure 3.2: A schematic view of HESR lattice. The injection from the RESR is on the lower left and from SIS18 (upgrade) on the lower right. The lower straight houses the PANDA experiment with its three dipole magnets of the chicane, the target (arrow), the solenoid magnet around the target and the compensation solenoid magnet. Injection septa and kickers, the radio frequency cavities left of PANDA, and the stochastic cooling pickups right of PANDA are also installed in this straight. The upper straight section houses the electron cooler. Compensation solenoid magnets as well as upgrade space reserve for a Siberian snake for polarized antiprotons is indicated left and right of the cooler. The helix dipole magnet is part of the cooler upgrade. The upper straight houses also the stochastic cooling kickers. The signal lines of the stochastic cooling system are drawn. At the upper left corner, the HESR tunnel is indicated.

magnets are foreseen to compensate the effects of the cooler solenoid magnet. Next to the compensation solenoid magnets, sufficient space is reserved for an upgrade of the electron cooler for a Siberian snake [50]. This upgrade consists of skew quadrupole magnets and additional solenoid magnets. For a full Siberian snake, a helix dipole magnet is needed in addition to the solenoidal fields. It is planned to be located downstream of the electron cooler. An H^0 detector is included in the HESR design and detects hydrogen atoms created by recombination of electrons and protons in the electron cooler. Since the count rate is a measure of the beam overlap, the H^0 detector will be used for commissioning and optimization of the electron cooler. Without the injection branch from SIS18, protons have to move in the same direction as antiprotons. This implies a change of polarity of all magnets due to the different charge and the location of the H^0 detector being also downstream of the electron cooler from the view of antiprotons. The stochastic kickers will be installed at the beginning of this straight section.

Arcs The design of the arcs is based on regular FODO[1] structures. There are two demands which require a change to the FODO setup. The straight sections have to be dispersion-free and the transition energy has to be adjustable in the range from $\gamma_{tr} = 6.2$ to $\gamma_{tr} = 15$. While a regular FODO lattice uses two quadrupole magnet families (one horizontal and one vertical) to adjust the phase advance of the arcs, the revised design include four quadrupole magnet families: Three horizontal and one vertical. One horizontal and the vertical quadrupole magnet family is used to adjust the tunes. The second horizontal quadrupole family is dedicated to the adjustment of the transition energy. The second last dipole magnet at each end of the arcs has been removed. This missing dipole magnet concept form together with the third horizontal quadrupole magnet family a dispersion suppressor. Since the straight sections have to be dispersion-free, sextupole magnets for chromaticity correction must be placed in the arcs. Due to the design of the arcs, the places for sextupole magnets and orbit correction devices are limited to 48 per arc.

3.2.2 Magnets

The main magnet types [57] will be discussed in this chapter. All magnets of the HESR will be normal-conducting and therefore iron-dominated.

Dipole magnet The HESR dipole magnet is a laminated room-temperature magnet. Its yoke has a length of $4.126\,m$ and a width of $1.142\,m$. The yoke itself has to be bent due to space restrictions of the HESR tunnel. Since the HESR design of the arcs requires 44 dipole magnets, each dipole

[1] A regular structure where dipole magnets (O) are located between horizontally focussing (F) and defocusing (D) quadrupole magnets

magnet has to deflect the beam by 8.182° which corresponds to a local curvature of 29.432 m. The maximum magnetic field strength is 1.7 T for a beam momentum of 15 GeV/c. A current of 2930 A is necessary to reach the maximum magnetic field. Since the magnetic field scales linearly with the momentum, the lowest magnetic field is in the order of 0.17 T. However, the dipole magnets are designed for a nominal magnetic field of 1 T which corresponds to a momentum of 8.9 GeV/c because the main PANDA experiment will operate at this momentum.

Quadrupole magnet The design of the HESR quadrupole magnet is based on the COSY one [58] although the yoke of the HESR quadrupole magnet consists of four parts whereas the COSY quadrupole magnet has a two-part yoke. The length of the iron yoke is 0.58 m whereas the effective length is 0.6 m. The other dimensions of the yoke are 1.06 m in width and also in height. The aperture is with 100 mm large enough to fit in the vacuum chamber which has a diameter of 89 mm. The maximum gradient for operation has a design value of 20 T/m. This corresponds to a current of 426 A. Depending on the acceleration strategy to overcome the transition energy, the gradient of 20 T/m might not be sufficient. From the design of the HESR quadrupole magnet, a gradient of 25 T/m is possible although not desired to be used regularly due to saturation effects. The current necessary to achieve this gradient is larger than 700 A. The number of quadrupole magnets in the HESR is 84.

Sextupole magnet The HESR lattice includes 52 places for sextupole magnets in the arcs which are going to be used for chromaticity correction. Furthermore there are four places within each straight section reserved for sextupole magnets or higher-order multipoles for resonance manipulation if that will become necessary. The sextupole magnet design foresees a two-part yoke. The yoke has a length of 0.3 m. The sextupole magnet design has equal dimensions in width and height of 0.45 m. The diameter of the aperture is 140 mm. This is 40% larger than the aperture of a quadrupole magnet. The purpose of the large aperture of the sextupole magnet is to house a beam position monitor which besides others is caused by the space restrictions in the arcs. With a current of 290 A, a sextupole magnet generates are gradient of 45 T/m^2. This corresponds to an overall integrated sextupole magnet strength of 0.25 m^{-2}.

Orbit correction dipole magnets The orbit correction dipole magnets can deflect the circulating antiproton beam in one plane only. Because of the mounting, the design differs slightly for horizontally and vertically deflecting ones. There are two main types of orbit correction dipole magnets. This first type has a deflection strength of 1 $mrad$ at 15 GeV/c for orbit correction purposes. The second type can deflect 2 $mrad$ at 15 GeV/c where 1 $mrad$ is used for orbit correction and the other one for

wanted displacements of the beam to e.g. bypass obstacles or direct the beam onto the target. The doubling of the deflection strength is performed by increasing the windings per coil from 22 to 44. The maximum deflection strength corresponds to a current of roughly $304\,A$. The gap height is with $100\,mm$ equal to the diameter of the quadrupole magnets aperture

3.2.3 Beam parameters

The quality of the antiproton beam delivered by the RESR is depending on the number of accumulated antiprotons. The transverse beam emittance and the momentum spread grow with the number of antiprotons. The rms values are given by [3]

$$\begin{aligned} \epsilon_{x,y} &= \frac{1 mm\, mrad}{\beta\gamma}\left(\frac{N}{N_0}\right)^{4/5} \\ \frac{\sigma_p}{p} &= \frac{1.33\cdot 10^{-3}}{\beta\gamma}\left(\frac{N}{N_0}\right)^{2/5}, \end{aligned}$$

where N denotes the number of injected antiprotons and $N_0 = 3.5\cdot 10^{10}$ the reference number.

There are two defined modes of operation: A high luminosity mode and a high resolution mode. The high luminosity mode will provide a luminosity of up to $2\cdot 10^{32} cm^{-2} s^{-1}$ with 10^{11} antiprotons in the beam and a momentum spread of $\sigma_p/p \approx 10^{-4}$. To achieve this high luminosity, a pellet target of frozen hydrogen with an areal density of $4\cdot 10^{15}$ atoms$/cm^2$ is planned to be used. For the high resolution mode the momentum resolution of $\sigma_p/p \geq 4\cdot 10^{-5}$ is only available with a reduced number of antiprotons in the order of 10^{10}. Its upper momentum limit is defined at $8.9\,GeV/c$ where the main PANDA experiment takes place.

To prevent an unbound beam blow up due to interactions with the target, beam cooling is used. This is especially important for the high resolution mode due to the strong demands concerning the momentum spread. Simulations of beam equilibria for both cooling methods have been performed [59, 60, 61]. The beam loss and beam luminosity are more important for the high luminosity mode. To estimate the luminosity, the HESR cycle has been determined [62]. The beam loss is dominated by hadronic interactions, Coulomb single scattering, and the energy loss caused by the scattering at the target.

The beam parameter at injection and the experimental requirements of PANDA for the antiproton beam as well the beam parameters for both operation modes are listed in Table 3.1.

Beam parameters at injection	
Transverse Emittance	$1\,mm\,mrad$ (norm., rms) at $3.5 \cdot 10^{10}\ \bar{p}$
Relative momentum spread	$1.33 \cdot 10^{-3}$(norm., rms) at $3.5 \cdot 10^{10}\ \bar{p}$
Bunch length	$200\,m$
Momentum	$3.8\,GeV/c$
Injection method	Within a single turn (kicker injection)

Experimental beam requirements by PANDA	
Kind of particles	antiprotons
Antiproton production rate	$2 \cdot 10^7\ s^{-1}$
Momentum range	1.5 to $15\,GeV/c$ (0.83 to $14.1\,GeV$)
Number of antiprotons	$10^{10}$to 10^{11}
Areal target density	$4 \cdot 10^{15}$ atoms/cm^2
Beam size at target	$\approx 1\,mm$ (rms)

Beam parameters of mode	high luminosity	high resolution
Maximum luminosity	$2 \cdot 10^{32}\,cm^{-2}s^{-1}$	$2 \cdot 10^{31}\,cm^{-2}s^{-1}$
Momentum spread (rms)	$\sigma_p/p \geq 4 \cdot 10^{-5}$	$\sigma_p/p \approx 10^{-4}$
Momentrum range	1.5 to $15\,GeV/c$	1.5 to $8.9\,GeV/c$

Table 3.1: Beam parameter for the injection, requirements of PANDA, and both modes of operation

3.2.4 Electron cooler

Since this thesis covers the calculations of an local close orbit correction concerning the deflections caused by the bending toroid magnets of the electron cooler [63, 3], the latter is here of particular interest. It will be used together with stochastic cooling to achieve the demanding requirements of PANDA. The electron cooler is capable to cool the antiproton beam in the momentum range from 1.5 to $8.9\,GeV/c$. This corresponds to an electron energy in the range from $400\,keV$ to $4.5\,MeV$ since the velocity of the electrons and that of the antiprotons have to match. The design of the electron cooler includes the possibility for a later upgrade to a maximum electron energy of $8\,MeV$. This upgrade will allow electron cooling over the whole momentum range of the HESR. The circulating antiproton beam can be pre-cooled with the stochastic cooling system. The voltage of the electron cooler will be kept constant during one cycle to achieve the desired stability of the electron energy. This implies that the electron cooler can only be used at injection energy when this coincides with the experimental energy. The electron cooler has to compensate heating effects introduced by the interaction of the circulating antiproton beam with the internal PANDA target. Such a compensation can only be performed with magnetized cooling using a sufficiently strong longitudinal magnetic field [64, 65, 66]. The necessary magnetic field strength inside

the interaction straight was chosen as $0.2\,T$ to allow a larger diameter of the electron beam. The resulting electron beam radius in the cooling section was determined to be in the order of $5\,mm$. The $24\,m$ long cooling interaction straight matches the requirements since the cooling rate is proportional to the product of the electron cooler length and the electron current. A maximum electron current of $1\,A$ was selected according to the recommendations in [64, 65, 66]. A controlled misalignment angle between the antiproton and the electron beam avoids too small beam spots.

A schematic view of the HESR electron cooler is shown in Figure 3.3. It presents the beam path of the electrons which includes the bends caused by toroid magnets. The toroid magnets at both end of the interaction straight affect also the circulating antiproton beam. The design parameters of both relevant toroid magnets are equal although the toroid magnets are differently aligned.

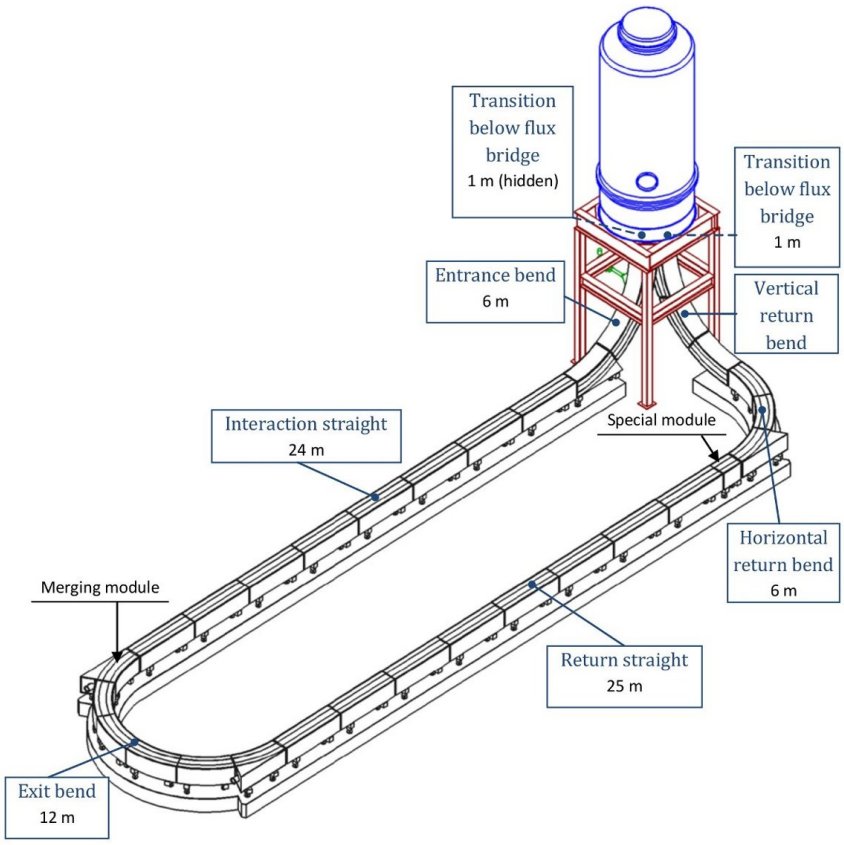

Figure 3.3: The layout of the HESR electron cooler consists of a high voltage terminal and a beam path utilizing solenoid and toroid magnets. The cooler tank houses besides the electron gun and the acceleration column also the collector. The toroid magnets which are part of the electron guiding system can be seen. Below the tank, there is a vertical bend whereas a horizontal one is at the end of the interaction straight.

3.2.5 Ion optical properties

Transition energy and defined ion optical settings The adjustability of the transition energy in the range from $\gamma_{tr} = 6$ to $\gamma_{tr} = 15$ is important for the stochastic cooling system. The frequency slip factor η has to be sufficiently small to reduce unwanted mixing from the stochastic pickup to kicker [67] and changes with the beam energy. Therefore two essential ion optical settings with $\gamma_{tr} = 6.2$ and $\gamma_{tr} = 13.3$ have been defined which are suitable for a certain range of the beam energy. The $\gamma_{tr} = 6.2$ setting will be used for a beam energy above the injection energy of $3\,GeV$. This means that the $\gamma_{tr} = 6.2$ lattice will be used for the main PANDA experiment at $8.9\,GeV/c$. The $\gamma_{tr} = 13.3$ setting is designed for the lower momentum range of the antiproton beam. The ion optical setting for injection is based on the $\gamma_{tr} = 6.2$ layout but with reduced beta functions around the target since no focussing at the target is needed during injection. The ion optics for both lattice settings are shown in Figure 3.4.

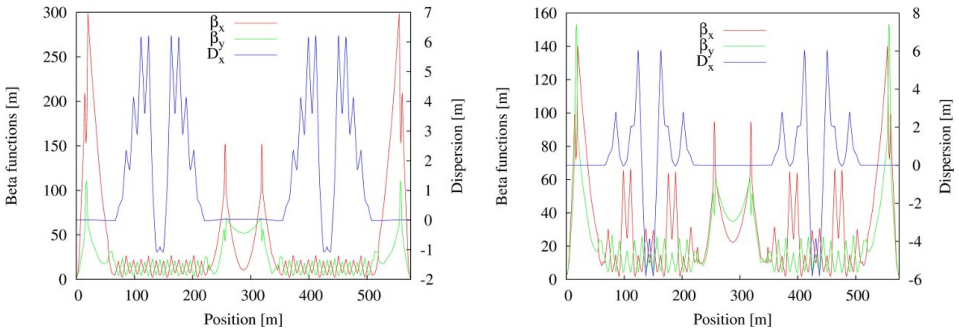

(a) The $\gamma_{tr} = 6.2$ lattice **(b)** The $\gamma_{tr} = 13.3$ lattice

Figure 3.4: Ion optics of the HESR for both lattices a) $\gamma_{tr} = 6.2$ and b) $\gamma_{tr} = 13.3$. The target is located at the origin. The center of the electron cooler is at $s \approx 288\,m$. Both plots show the modulation of the horizontal dispersion (blue) function to achieve dispersion-free straight sections. The beta functions (red and green) are much larger around the target than in the arcs which is caused by the focusing at the target. The comparison of both ion optics reveals the differently large maximum beta functions around the target. Also the dispersion functions have different shapes.

Beta functions The beta functions can be adjusted at several points in the HESR, e.g. at the target or at the electron cooler.

The beta functions at the target are adjustable in the range from 1 to $20\,m$ to match the energy dependent beam size to the target size. Proper beam target overlap requires a constant beam size of roughly $1\,mm$ (rms). The necessary focusing leads to an increase of the beta functions in the adjacent quadrupole triplets.

The beta functions at the electron cooler interaction region are adjustable in a range from 20 to 200 m. This is necessary to match the size of both beams because the transverse dimensions of the antiproton beam change significantly with the energy through adiabatic damping whereas the electron beam radius is fixed at 5 mm.

Natural chromaticity The natural chromaticity introduced by momentum dependence of the focussing of the quadrupole magnets ranges for the HESR from -10 to -15. It is $\xi_x = -14.82$ and $\xi_y = -10.31$ for the $\gamma_{tr} = 6.2$ lattice. For the $\gamma_{tr} = 13.3$ lattice, the natural chromaticity is with $\xi_x = -14.53$ horizontally slightly smaller whereas it is larger for the vertical one: $\xi_y = -11.13$.

3.3 Comparison with COSY

Alike the HESR, the Cooler Synchrotron COSY of the Forschungszentrum Jülich is a storage ring with an electron cooler and a stochastic cooling system. It can store and accelerate polarized and unpolarized proton and deuteron beams in a momentum range from approximately 0.30 (0.54 for deuterons) up to 3.7 GeV/c [68, 69]. An overview of COSY with its internal and external experiments is shown in Figure 3.5.

COSY has, similar to the HESR, a race track shape and consists of two symmetric arcs and two straight sections. It has a circumference of 183.4 m and is approximately a factor three shorter than the HESR. The straight sections have a length of 40 m each. The ion optics of the straights are adjustable to perform an identity mapping where the phase advance is then $\psi = 2\pi$. Each arc is constructed out of three unit cells and both arcs are mirror-symmetric. Each unit cell itself consists of two mirror-symmetric halfcells using a FODO arrangement.

Although the injection types of COSY and HESR differ (COSY has a stripping injection whereas the HESR uses a kicker injection), there are many similarities between the two accelerators. Both feature the same beam cooling techniques and have an electron cooler and a stochastic cooling system. Although the HESR will have only one experiment installed and COSY has several internal and external experiments. The WASA experiment [73] installed in COSY is of particular interest for the HESR development since it has a pellet target like PANDA. All of these similarities justify the use of COSY as a benchmarking facility for the HESR. Thus, several on-going experiments at COSY cover hardware and experimental techniques which are relevant for HESR design and future operation.

New cavities have been designed and built for example a barrier bucket cavity [43] to compensate the mean energy loss induced by the internal pellet target. Cooling hardware has also been developed. The stochastic cooling system for the HESR will use hardware e.g. stochastic pick-

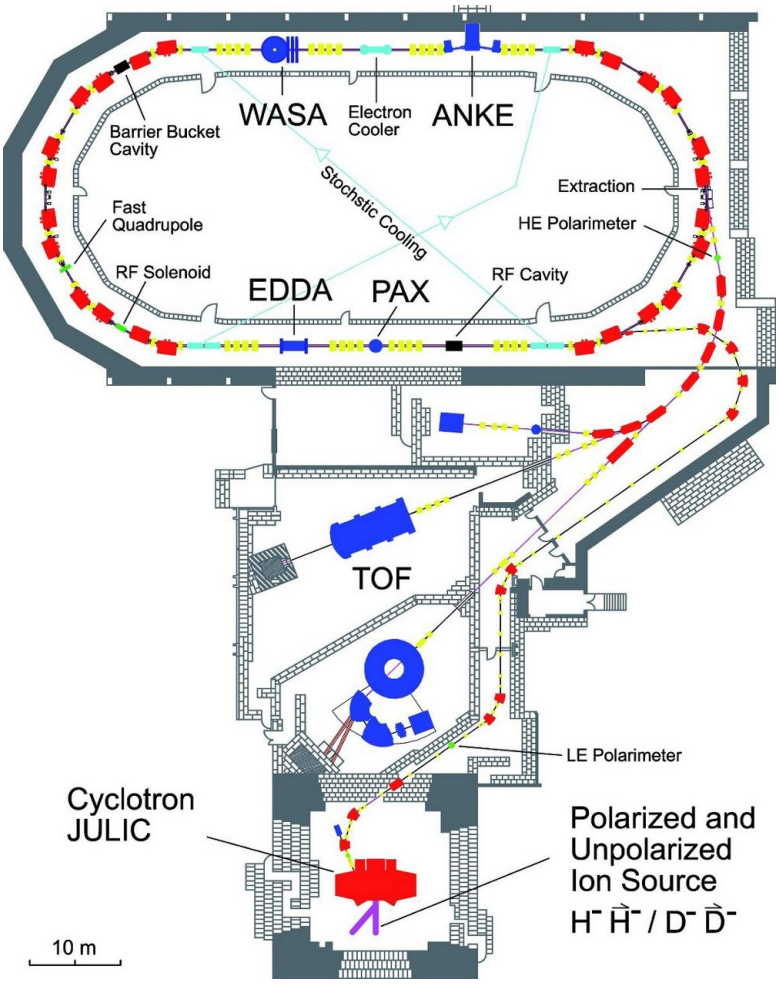

Figure 3.5: Schematic overview of cooler synchrotron COSY. The location of the ion sources for polarized and unpolarized beams are indicated. The cyclotron Julic is used for pre-acceleration. The electron cooler and the stochastic cooling devices of COSY are shown and the signal lines of the stochastic cooling system are indicated. The positions of the accelerating radio frequency cavities and the barrier bucket cavity as well as fast quadrupole and radio frequency solenoid magnet for polarization preservation and manipulation are designated. The locations of the internal experiments EDDA [70, 71], ANKE [72], WASA [73] including its pellet target and PAX [47] are marked. Injection, extraction and the external experiment TOF [74] are shown as well.

ups with slot coupler [43] which have not been used at COSY before. Therefore prototypes have been built and tested at COSY. Besides new hardware, stochastic cooling techniques like the time-of-flight cooling have been successfully applied and compared to notch-filter cooling [67]. The combination of a barrier bucket cavity together with stochastic cooling to compensate beam-target interaction was verified to be effectively working. As a step toward the high energy electron cooler planned for the HESR,

a $2\,MeV$ electron cooler is going to be built and installed into COSY to investigate the cooling forces and possibilities at high energies [75]. Also hardware related to beam diagnostics like a beam profile monitor was tested at COSY [76].

The proposed orbit response matrix method for closed orbit corrections at the HESR has been applied at COSY. Since COSY has an electron cooler like the HESR, the local toroid magnet compensation bumps have to be taken into account for closed orbit correction, resulting in similar conditions as for the HESR. The orbit response matrix method could be validated as it is described in chapter 4.2.

Chapter 4

Closed orbit correction

Alignment errors of accelerator components like magnets have been estimated and used to calculate closed orbit deviations. An orbit correction concept has been developed to allow efficient closed orbit corrections in the HESR. The orbit response matrix method is proposed for closed orbit corrections in the HESR and has been used to correct the closed orbit at COSY. Furthermore, the flexibility of local closed orbit bumps at various locations has been checked.

4.1 Closed orbit correction system for HESR

4.1.1 Alignment errors

Magnets have to be aligned in three spatial and three rotational degrees of freedom. All deviations from the ideal alignment lead to orbit distortions. For simulation purposes the assumed Gaussian distribution of alignment errors was reasonably truncated at $2.5\,\sigma$ [77]. A uniform and Gaussian distribution have already been compared [78] and thus this was not checked again. Alignment errors have been applied to all elements in the HESR including beam guiding magnets like dipole or quadrupole magnets, beam position monitors, and orbit correction dipole magnets. The alignment errors of COSY are shown in Table 4.1 and have been used for the simulations for the HESR. The angular errors have been calculated based on the spatial errors and on the element dimensions.

The COSY accelerator is surrounded by concrete walls and a concrete roof, the so called COSY tunnel, inside the COSY hall. There are two central reference points in the center of COSY hall. These reference points are used to create an alignment grid inside the COSY tunnel. This grid has been used to align all magnets and elements of COSY. The alignment grid for the HESR will be created differently. FAIR will have a primary alignment grid on the surface which will be transferred to the accelerators [80]. The HESR tunnel will be surrounded by soil instead of being inside a hall. Thus, there will be no central reference points as for COSY. Instead,

Magnet type	$ds\,[mm]$	$dx\,[mm]$	$dy\,[mm]$
Dipole magnet	1.0	0.2	0.2
Quadrupole magnet	0.2	0.5	0.2
Sextupole magnet	0.5	0.5	0.2
Correction dipole magnet	0.2	0.5	0.8

Table 4.1: Alignment errors of elements based on COSY alignment accuracy [79]. The MAD-X nomenclature has been adopted. The alignment errors are given in the local co-moving coordinate system which means that ds is a shift along the beam axis whereas dx and dy are transverse misalignments.

there will be a certain number of reference points transferred from the primary to the local alignment grid inside the HESR tunnel. The local alignment grid in the HESR tunnel will base on these transferred reference points. The number of the reference points necessary to achieve the desired alignment accuracy can be estimated by simulations but was not done so far. The individual elements and magnets will be aligned using a laser tracker system on the local alignment grid. The final, global accuracy is not known by now since simulations of tunnels, detailed lattices etc. have to be performed first.

4.1.2 Simulation of orbit distortions

The simulation of the orbit deviations has been performed using MAD-X. Since MAD-X is not capable to calculate twiss parameters and closed orbit with respect to field errors, the field errors of magnet have been neglected in the first step. Alignment errors have been applied to all elements according to Table 4.1. The pseudo-random number generator has been fed with a variety of different seeds resulting in different closed orbits. An example of ten orbits calculated with different seeds is shown in Figure 4.1. The largest orbit deviations occur around the target and have a value of up to approximately $0.1\,m$. Anywhere else in the HESR, the maximum closed orbit deviations are with less than $0.04\,m$ a factor 2.5 smaller. This differences are caused by the very large beta functions of several $100\,m$ around the target. Nevertheless, the resulting uncorrected orbits are approximately one order of magnitude smaller than of the superconducting version of the HESR [78]. This can be traced back to the fact that the alignment of superconducting magnets is not as precise as of normal-conducting ones. Whereas normal-conducting magnets can be aligned in a direct way, superconducting magnets have to be aligned first inside a cryostat which also has to be aligned itself.

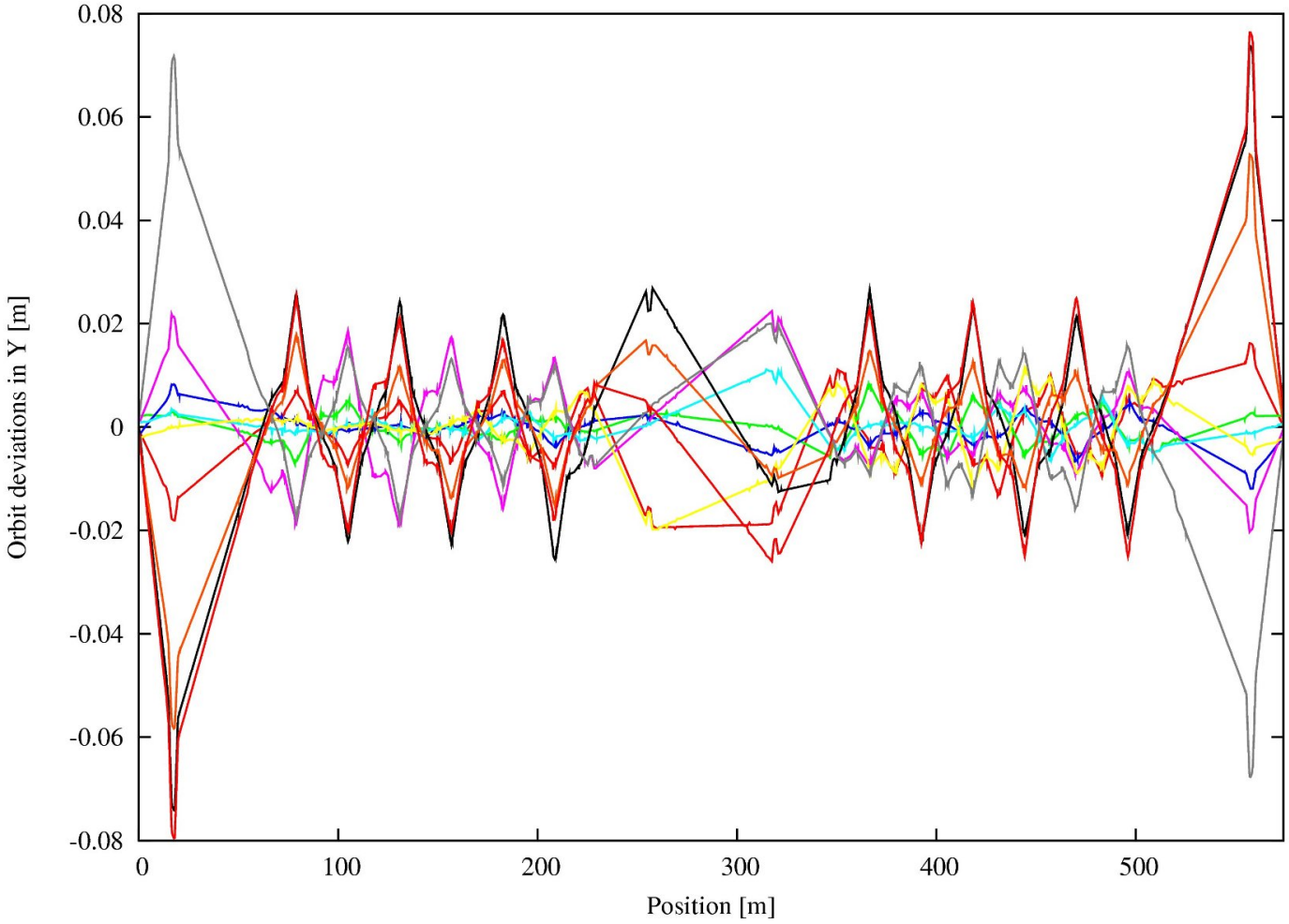

Figure 4.1: Example of uncorrected closed orbits in the vertical plane Y calculated with ten different seeds. The calculations are based on the $\gamma_{tr} = 6.2$ lattice. The origin is set to the target. The middle of the electron cooler solenoid magnet is located at $287.5\,m$. The $24\,m$ long cooler solenoid magnet is easy to identify since it does not include orbit correction dipole magnets. The largest deviations are located around the target which is caused by large beta functions. Everywhere else in the HESR, the closed orbit deviations are considerably smaller.

4.1.3 Orbit correction elements

While the design of the orbit correction dipole magnets allows a deflection of the beam in one transverse direction only, the proposed beam position monitors can measure in both transverse directions.

Accuracy of beam position monitors and orbit correction dipole magnets Beam position monitors can measure the position of a circulating beam with a certain accuracy. This accuracy is affected by two kinds of measurement errors. The first kind is an offset error which is independent of the beam position whereas the second kind is a scaling error. This scaling error affects the measurement accuracy depending on the beam position. The measurement errors applied to the simulation of closed orbit correction for the HESR [81] are listed in Table 4.2. Both error types are assumed to be *Gaussian* distributed because they shall represent simulated measurement errors of the beam position.

	Accuracy
Scaling	0.1
Offset [mm]	0.1

Table 4.2: Measurement accuracy of beam position monitors

The orbit correction dipole magnets are also misaligned (see Table 4.1). Other errors like calibration errors are not taken into account. This is no limitation because an iterative and converging method like the application of an orbit response matrix is able to compensate this. Errors of polarity of beam position monitors and orbit correction dipole magnets are easy to identify with a comparison between a measured and a calculated orbit response matrix. Thus there is no need to simulate this kind of error.

Location of beam position monitors and orbit correction dipole magnets The type of beam position monitors which will be used in the HESR is able to measure the orbit in both transverse planes. As it was described in paragraph 3.2.2, they will be integrated into the sextupole magnets. To find the best locations for beam position monitors and orbit correction dipole magnets, some constraints have to be considered. On one hand the efficiency of pairs of beam position monitors and orbit correction dipole magnets scales with the square root of beta function and with the cosine of the phase advance in between them (see equation 2.43). For chromaticity correction the efficiency of a sextupole scale with the horizontal dispersion.

Arcs Due to space restrictions, there are 48 possible locations per arc for sextupoles with beam position monitors and orbit correction dipole magnets. This implies that the phase advances are fixed and thus are not

as important as the beta functions and the horizontal dispersion. The locations for beam position monitors were chosen through the sextupoles and do not break the described mirror symmetry of both arcs.

To be precise, calculations have shown that the number of necessary beam position monitors is by four lower in each arc than the number of sextupole magnets required for chromaticity correction. Beam position monitors will also be included in the additional sextupoles to have a common design.

Straight sections The straight sections have different characteristics concerning the ion optical properties. The beta functions differ due to different requirements of e.g. PANDA target or electron cooler. The distribution of correction elements within the straights is guided by the beta functions. This results in the correction elements being placed close or within the quadrupole triplets. The mirror symmetry of the straights is maintained whereever this is possible.

Number and distribution of correction elements The proposed orbit correction scheme consists of 64 beam position monitors and 48 orbit correction dipole magnets.. The orbit correction elements are distributed as follows:

- 26 beam position monitors per arc
- 6 beam position monitors per straight
- 6 horizontal and 6 vertical orbit correction dipole magnets per arc
- 6 horizontal and 6 vertical orbit correction dipole magnets per straight.

4.1.4 Closed orbit correction for HESR

The orbit response matrix method is used for closed orbit corrections in the HESR. A computer program has been written to calculated the ideal orbit response matrix from the MAD-X closed orbit calculations. "Ideal" means that no alignment and field errors of magnets are taken into account. The orbit response matrix is inverted using SVD since this algorithm and the necessary vector matrix multiplication is fast and easy to implement in a control system for an automated closed orbit correction. After the inverted ideal orbit response matrix has been prepared, the computer program generates the alignment errors and runs MAD-X to calculate the resulting distorted closed orbit. The deviations from the reference trajectory are determined at the locations of the beam position monitors. To simulate measured close orbit deviations, the computer program applies the measurement errors of the beam position monitors. The necessary deflection strengths are calculated and checked if they exceed a pre-defined maximum correction strength. If that is the case, all values

are scaled to fit the boundary condition. The scaled correction strengths are applied to the MAD-X input which is used to calculate the resulting closed orbit again.

This iterative process converges within a few iterations and is stopped if the relative change of the calculated deflection strengths from one step to the other becomes smaller than 10^{-7}. When a predefined maximum closed orbit deviation is reached, the iteration process is stopped before convergence to save computation time.

The closed orbit correction system has to fulfill the following requirements [78]. Firstly, the maximum deflection strength of orbit correction dipole magnets shall not exceed $1\,mrad$ which is a typical value, e.g. for SIS100/300. Secondly, the orbit deviations shall be corrected to below $5\,mm$ maximum closed orbit deviation. The number of iterations necessary to correct a closed orbit was always below ten.

The simulated closed orbits which were shown in Figure 4.1 have been corrected with the described closed orbit correction procedure. The corrected closed orbit are shown in Figure 4.2 with the same color code. The scale of the plot shows that all of the corrected closed orbits presented in the Figure are confined within the requested $5\,mm$ range. The closed orbit corrections have been performed for 10000 different seeds and for both defined ion optical settings. To compare correction results, the maximum deviation of the corrected closed orbits is used. The results are summarized in Table 4.3.

Lattice	$\gamma_{tr} = 6.2$	$\gamma_{tr} = 13.3$
$X_{mean}\,[mm]$	3.34 ± 0.54	3.35 ± 0.54
$X_{min}\,[mm]$	1.88	1.92
$Y_{mean}\,[mm]$	3.51 ± 0.71	3.42 ± 0.68
$Y_{min}\,[mm]$	1.70	1.59

Table 4.3: Statistical summary of closed orbit correction simulations for different seeds and ion optical settings. The index *mean* indicates the mean value evaluated over all maximum closed orbit deviations and *min* the smallest value. The statistics for both defined ion optical settings have been calculated from corrections with 10000 different seeds.

The minimum values of the maximum closed orbit deviations do not belong to the same seeds. The closed orbit correction scheme and the applied procedure work for both ion optical settings. For all 10000 seeds, the maximum closed orbit deviations has been corrected to below the $5\,mm$ boundary. Since the optimization of the closed orbit correction was stopped whenever the maximum closed orbit deviation became smaller than the requested $5\,mm$ boundary, the closed orbits can be further optimized. It also explains why the underlying distribution is not Gaussian. In Figure 4.3, the latter is shown in the histograms which are related to resulting maximum closed orbit deviations.

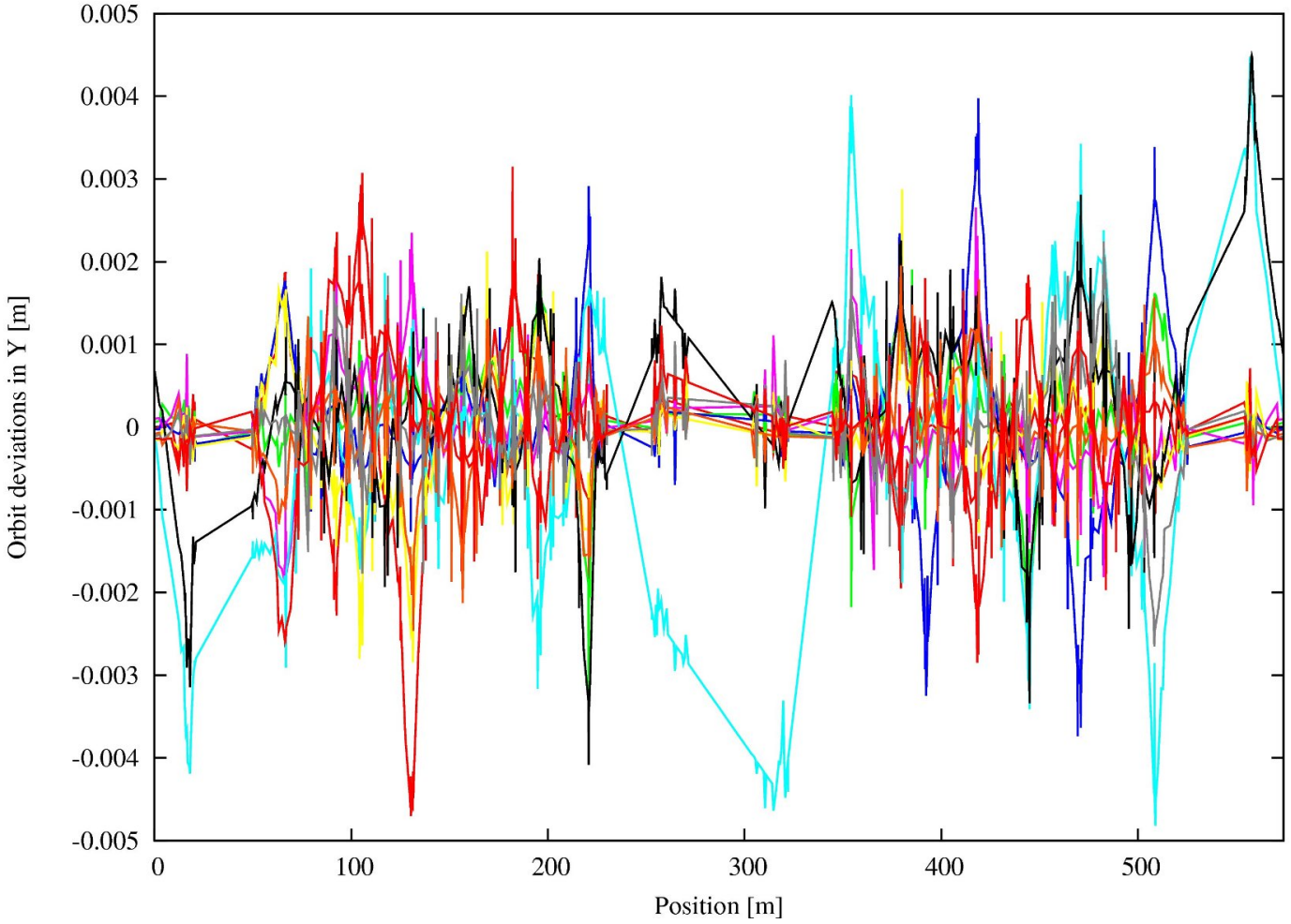

Figure 4.2: Example of corrected closed orbits in vertical plane Y with ten different seeds. For comparison reasons, the seeds and colors are the same as for the uncorrected ones shown in Figure 4.1. The calculations are based on the $\gamma_{tr} = 6.2$ lattice again. The origin is set to the target. The middle of the electron cooler solenoid magnet is located at $287.5\,m$. The corrected closed orbits are within the desired range of $\pm 5\,mm$.

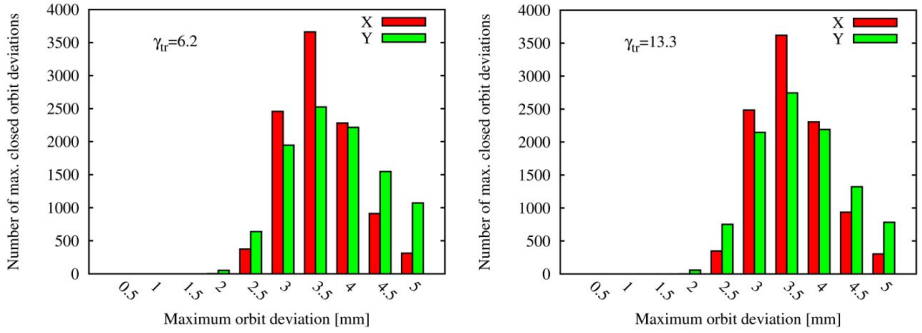

(a) $\gamma_{tr} = 6.2$ **(b)** $\gamma_{tr} = 13.3$

Figure 4.3: Histograms of maximum deviation of 10000 corrected closed orbits for both ion optical settings, a) the $\gamma_{tr} = 6.2$ lattice and b) the $\gamma_{tr} = 13.3$ lattice. The scale of the abscissa marks the maximum deviation of corrected closed orbits where the numbers represent the upper limit of a range, e.g. 5 corresponds to the range of 4.5 to 5. The ordinate shows the number of maximum closed orbit deviations for the given ranges. Both histograms show that the distributions are not Gaussian.

The comparison of both histograms show that the distributions look very similar. This indicates that the closed orbit correction system perform almost equally well for both investigated ion optical settings.

4.1.5 Orbit correction including field errors

The influence of field errors on the closed orbit cannot be investigated using the regular MAD-X version since it takes field errors into account only for tracking. There exist an extended version of MAD-X which contains the PTC[1] module [82]. PTC is capable to calculate the closed orbit with respect to field errors and alignment errors and has been used to investigate the relevance of field errors. Closed orbit correction simulations including field errors have been performed according to the following procedure:

1. Simulate and correct the closed orbit without field errors (MAD-X)
2. Retrieve the strengths needed for the closed correction dipole magnets
3. Use PTC with field errors and apply the correction strengths to the orbit correction dipole magnets
4. Determine the resulting maximum closed orbit deviations

This investigation was done for a smaller amount of seeds (500 per ion optical setting) which is sufficient for a cross check. The field errors which

[1] Polymorphic Tracking Code

have been used can be found in chapter 5.3. The dipole errors at $1.7\,T$ main field have been used for the $\gamma_{tr} = 6.2$ lattice and at $0.17\,T$ for $\gamma_{tr} = 13.3$ one. The used quadrupole errors are the ones for a current of $550\,A$ ($\gamma_{tr} = 6.2$) and $200\,A$ ($\gamma_{tr} = 13.3$). It could be shown that the resulting closed orbits are slightly changed by the field errors. For those exceeding the $5\,mm$ border, further optimization with MAD-X has been performed. This was sufficient to fulfill the $5\,mm$ constraint even when including field errors.

The dipole field can be influenced by the surrounding magnets, which cause a shortening of the effective field length. Furthermore, ripples of the power supplies and remanence effects also influence the close orbit. Since these effects are dynamic, i.e. they change during a cycle, they have not been investigated. The closed orbit corrections and simulations are only performed for static accelerator settings and magnet properties. Such investigations concerning dynamical changes of the accelerator and magnets will be carried out at a later stage.

4.1.6 Closed local orbit bumps for HESR

In the HESR, a good beam alignment is necessary at various locations, e.g. at the target. This adjustments of the beam position and angle are achieved using so called local closed orbit bumps. For the HESR, the local closed orbit consist typically of four correction dipole magnets used to align the beam as necessary. Since the orbit bumps are local and closed, they will not affect the global closed orbit outside of its boundaries. These orbit bumps have to provide enough flexibility to adjust the beam in the desired way. Except for the toroid magnet compensation and for the H^0 closed orbit bump, a deflection angle of $1\,mrad$ is sufficient for all necessary correction dipole magnets used for local closed orbit bumps.

At the target To maximize the interactions of the circulating beam with the internal PANDA target, a good beam target overlap is crucial. Two beam position monitors are planned to be located near the target to determine beam position and angle. Using a local closed orbit bump, it is possible to optimize beam target overlap by adjusting the location of the beam until the count rate of the PANDA detector reaches a maximum. The beam has to be adjustable in the range from $+5$ to $-5\,mm$ to provide enough flexibility. Simulations have shown that $1\,mrad$ is sufficient to achieve this even with a worst case estimate concerning the $5\,mm$ closed orbit deviations. The simulation has been performed with an angle adjustment to $0°$. During the simulations, it could be observed that the orbit is not fully closed and there was a slight change of the global closed orbit. This is due to the simulation where the deflection strengths are calculated from the ideal computer model whereas for the closed orbit alignment er-

rors are taken into account. Such deviations can be minimized by an optimization of the computer model.

At injection The beam location and its angle with respect to the reference trajectory have to be very accurate at the injection kicker. If the injected and the circulating beam are not properly matched, this mismatch would leads to unwanted emittance growth. There are basically two ways to match the beams. The first approach is to adjust the closed orbit of circulating beam to the parameters of the injected beam. This implies that the closed orbit is changed completely and at all locations in the HESR. The other way is to setup a local closed orbit bump around the injection kicker. This is more preferable since this approach does not change the global closed orbit.

At the H^0 detector For proper beam cooling in the electron cooler, a good overlap of the circulating and the electron beam is important. For commissioning and optimization of the electron cooler, a circulating proton beam will be used together with an H^0 detector. Inside the cooling section, protons and electrons can recombine to atomic hydrogen. Before the atomic hydrogen reaches the H^0detector, the electrons are removed inside the surrounding material of the H^0 detector and the protons are counted. The count rate is a measure of the alignment accuracy of the two beams.

The designated place of the H^0 detector will be in between the two quadrupole triplets behind the electron cooler. The circulating beam has to be deflected around the H^0 detector to prevent the latter from counting the protons of the beam. The are two possible solutions to install the H^0 detector. The first possibility is to introduce a kink to the beam pipe and to install the H^0 detector outside. The second possibility is to place the H^0 detector within the beam pipe and to deflect the circulating beam around it. The latter is investigated due to a simpler setup and lesser modifications to the beam pipe.

It is assumed in the following that both transverse phase space ellipses lie within the electron cooler which implies $|\alpha_{x,y}| \ll 1$. The beta functions at the electron cooler are adjustable to keep the diameter of the circulating beam constant (see Table 4.4). The resulting $1\,\sigma$ radius of the atomic hydrogen beam at the detector is smaller than or equal to $10.29\,mm$. The maximum $1\,\sigma$ radius (at $1.5\,GeV/c$) of the circulating beam is in the range of $3.66\,mm$ at the detector. For injection energy ($3.8\,GeV/c$), the $1\,\sigma$ radius of the H^0 beam is much smaller (approximately $4\,mm$).

p $[GeV/c]$	ε $[mmmrad]$	β $[m]$	$u_{\max,1\sigma}$ $[mm]$	$p_{\mathrm{u,max},1\sigma}$ $[mrad]$	$u_{H_0,1\sigma}$ $[mm]$
1.5	0.637	19.6	3.53	0.18	10.29
3.8	0.250	50.0	3.54	0.07	4.00
8.9	0.107	116.0	3.52	0.03	3.52
15	0.064	196.0	3.54	0.02	3.54

Table 4.4: Preferred beta functions at electron cooler where p denotes the momentum, ε the transverse geometric emittance and β the beta functions at the electron cooler. The resulting beam radius and angle as well as the resulting H^0 beam radius at the H^0 detector are also shown. In the last three columns "u" represents the coordinates x or y.

Compensation of toroid magnet deflections at the electron cooler
Toroid magnets are part of the beam guiding system of an electron cooler and are bent solenoid magnets with an additional dipole field to compensate the centrifugal force. With these, the electron beam is deflected into and out of the beam pipe of the circulating beam. Since the magnetic rigidities of antiprotons and electrons differ, the deflection of antiprotons is smaller than that of electrons. The deflections caused by the toroid magnets are larger for lower momenta. The toroid magnet design parameters are given in Table 4.5.

Bending radius of electron beam	$R_0 = 4\,m$
Magnetic strength on	$B_0 = 0.2\,T$
Bending angle of toroid magnets	$\varphi_0 = 30°$

Table 4.5: Design parameters of electron cooler toroid magnets

To compensate the deflections, four additional correction dipole magnets have to be included in the HESR lattice, two on each side of the electron cooler. The inner ones should be placed very close to the toroid magnets to keep the orbit deviations introduced by transverse momenta as small as possible. Due to space restrictions, the inner correction dipoles should be designed to deflect the circulating beam in both transverse planes. The strengths of the correction dipole magnets for 1.5 GeV/c beam momentum have to be 28.75 $mrad$ and 3.32 $mrad$ for both planes of the the inner correction dipole magnets and 1.42 $mrad$ and 0.05 $mrad$ for both planes of the outer ones. Depending on the distance between extrapolated toroid magnet deflection and inner steerers, these values will increase. To give an example: If the distance is 0.3 m, the strengths increase to 31.03 $mrad$ and 3.58 $mrad$ for the inner steerers and 1.98 $mrad$ and 0.06 $mrad$ for the outer ones. The strength of the inner steerers increases faster than that of the outer steerers.

The toroid at the entrance of the electron cooler below the cooling tower has a vertical bent whereas the toroid at the end of the interaction

straight has a horizontal one (see Figure 3.3). The solutions at both end differ by a rotation of 90°. Therefore, it is sufficient to obtain one solution only.

4.2 Closed orbit correction at COSY

During a PAX [47, 83] beam time, an orbit response matrix was measured and applied to correct the closed orbit afterwards.

4.2.1 COSY settings

Two main settings have been used [84]. The first one use dispersion suppression in the straight sections. The other setting was without dispersion adjustments in the straight sections. The proton beam energy was set to $45.01\,MeV$ which corresponds to a momentum of $294.08\,MeV/c$. The proton beam was electron cooled. The tunes were set to different values in the range from 3.568 to 3.623 depending on the dispersion setting as it is shown in Table 4.6. The ion optics for the $D \neq 0$ setting are shown in Figure 4.4.

Dispersion setting	$D \neq 0$	$D = 0$
Q_x	3.620	3.580
Q_y	3.582	3.623

Table 4.6: Tune settings during experiment

4.2.2 Measuring orbit response matrix

The $D \neq 0$ setting was used during the orbit response matrix measurements. Neglecting coupling and because of time limitations, only the uncoupled orbit response matrices for both transverse planes have been measured. For both measurements, 29 beam position monitors were available including those in the electron cooler. All 20 horizontal orbit correction dipole magnets, two horizontal back-leg-windings on ANKE dipole magnets, and both compensation dipole magnets next to the electron cooler toroid magnets (deflecting horizontally only) where used for the measurement of the horizontal orbit response matrix. For the measurement of the vertical orbit response matrix, 17 orbit correction dipole magnets were available.

The measurement procedure was to deflect the beam in both transverse planes (left and right; up and down) with a change of 5% in terms of current. The 5% variation was used if no beam loss was indicated by the BCT[2] signal. Otherwise the adjustment of the deflection current

[2] Beam current transformer

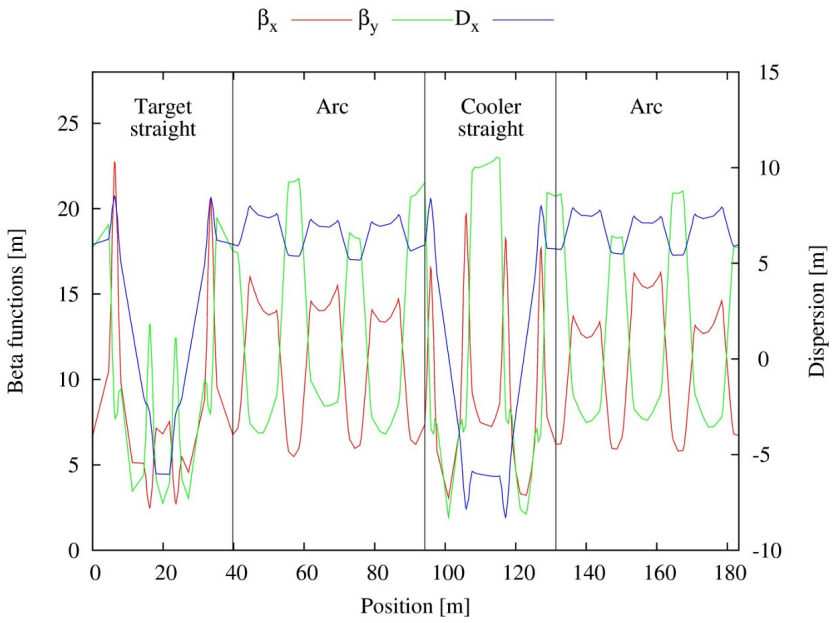

Figure 4.4: COSY ion optics with $D \neq 0$ in straights. The main sections are indicated. The center of the electron cooler is at $s = 111.5\,m$.

was reduced. The closed orbit changes at the beam position monitors normalized to a 1% variation of current correspond to the entries in the orbit response matrix. Thus the measured COSY orbit response matrices can be used to calculate orbit changes in term of current changes of the deflecting devices.

4.2.3 Comparison of measured and calculated orbit response matrix

As described in chapter 2.1.9 the orbit response matrix can be calculated from a computer model of the accelerator. A comparison with a measured orbit response matrix can provide useful information of and optimization capabilities for the model. Besides extensive optimization and calibration routines like LOCO [85], an easy and simple check is the ratio of corresponding matrix elements. If the ratio is equal to one for all indices, the model describes the accelerator perfectly. A column or row with negative values indicate that the corresponding correction element has wrong polarity. To compare both matrices, the measured orbit response matrix was renormalized to deflection angles in *mrad* using the calibration table of the COSY control system.

The check of the COSY orbit response matrix showed that the ratio averaged over all matrix elements is in the order of 92%. The deviations are mainly introduced by small values of matrix elements where small differences between both matrices lead to large ratios.

4.2.4 Orbit correction

Although the orbit response matrix was measured for one specific machine setting, its application for other machine settings ($D = 0$) worked as well. The orbit response matrix was used as it is which means that it was not inverted but a χ^2 minimization was used. This kind of application takes more time for calculation but is easier and faster to set up.

One problem which occurred was related to the electron cooler. A usual machine setup would be planned to correct the closed orbit first and to set up the toroid magnet compensation for the electron cooler afterwards. Instead, the local closed orbit bump for the electron cooler was set up with an uncorrected closed orbit and could not be adjusted afterwards. Thus, the closed orbit correction using the orbit response matrix was used to correct the closed orbit while artificially maintaining the toroid magnet compensation. This application of the orbit response matrix with local boundary conditions led to a not fully corrected closed orbit. A distortion of the local closed orbit bump around the electron cooler could not be prevented and caused worse beam overlap of the proton and electron beams resulting in weaker cooling. The orbit correction had to be stopped after two iterations since the cooling capabilities were compromised after the third iteration.

Figure 4.5 shows the results of the orbit correction for both planes as well as the distortion of the local closed orbit bump around the electron cooler.

4.3 Discussion of results

Based on the alignment errors of COSY, closed orbit simulations have been performed for HESR. They show that the uncorrected closed orbit deviations can be nearly as large as $100\,mm$ which is more than twice the beam pipe radius of $44.5\,mm$. The largest closed orbit deviations occur near the target and are caused by the large beta functions in the surrounding triplets. Anywhere else is the HESR, the closed orbit deviations are by more than a factor two smaller and at least close to the beam pipe radius. The maximum closed orbit deviations are roughly one order of magnitude smaller than for the superconducting version of the HESR.

To limit the closed orbit deviations, a closed orbit correction has been developed and tested by various simulations. The boundary conditions of $1\,mrad$ maximum deflection strength at $15\,GeV/c$ and a resulting maximum closed orbit deviation of less than $5\,mm$ have been satisfied. Statistical investigations have also shown that the developed closed orbit correction system works almost equally well for both ion optical settings, the $\gamma_{tr} = 6.2$ and the $\gamma_{tr} = 13.3$ lattice. The necessary closed orbit bumps have been checked to not exceed an additional $1\,mrad$.

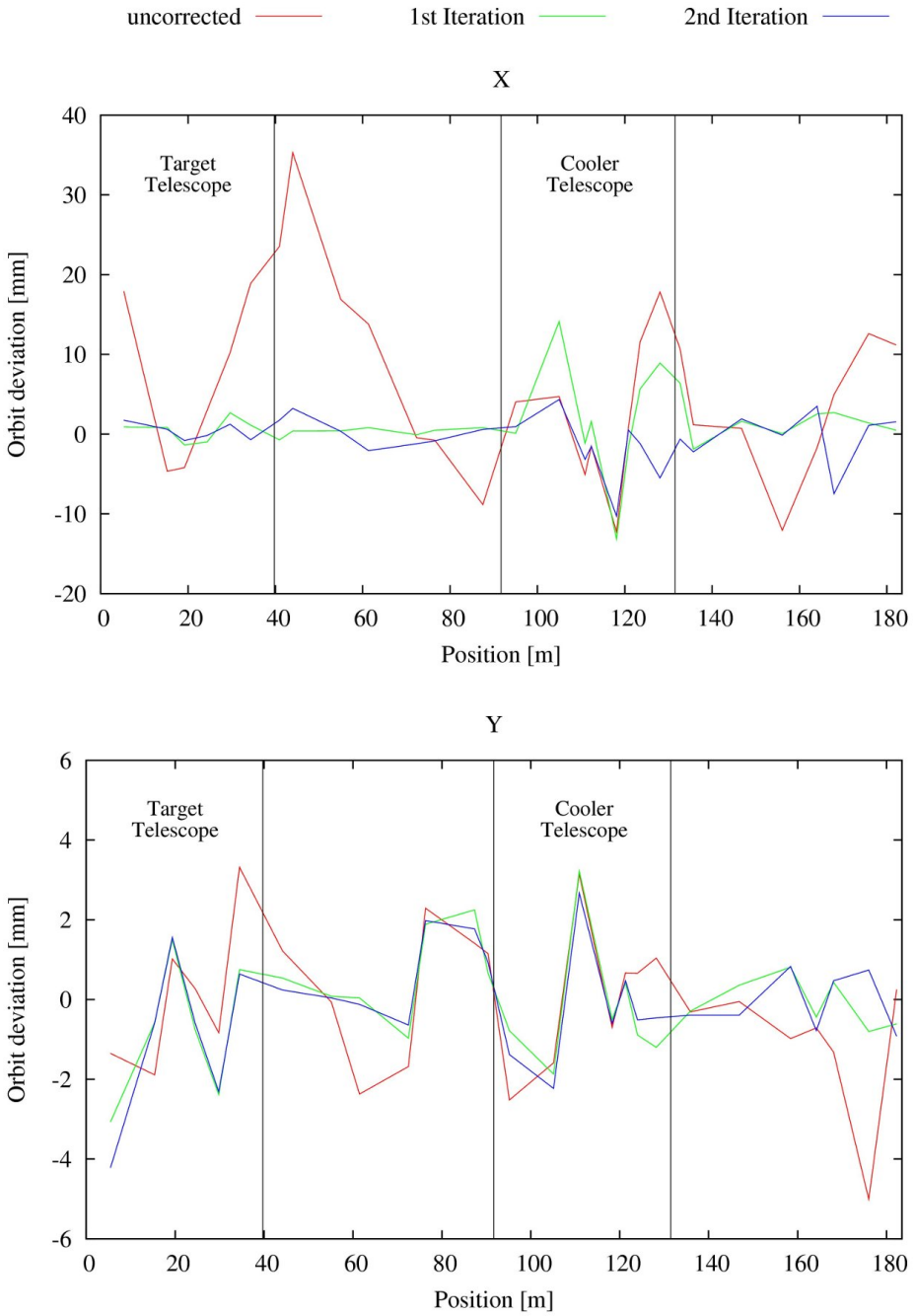

Figure 4.5: Horizontal (top) and vertical (below) closed orbit correction for COSY. The electron cooler is located at nearly 111 m. The toroid magnet compensation from approximately 104 m to about 120 m around the electron cooler becomes distorted. The vertical orbit is in general much better. The third iteration is not shown because it could not be used due to the weak electron cooling.

The orbit response matrix has been measured for COSY. Its application has shown that the correction method proposed for the HESR performs as expected except for the toroid magnet compensation. A correction of the maximum closed orbit deviations below $7.5\,mm$ was not possible due to the toroid magnet compensation at the electron cooler. The compensation bump could not be adjusted and had to be artificially maintained during the orbit correction. On one hand, this restricted the number of iterations to two. The third iteration compromised the cooling capabilities of the electron cooler and could not be used. On the other hand, there was no possibility to correct all orbit deviations larger than the intended $5\,mm$ due to overcompensation and the use of a global correction scheme with the local boundary conditions. Therefore, it is necessary for future closed orbit corrections at COSY and the HESR to adjust the local closed orbit bump around the electron cooler after each iteration as it was done for the HESR closed orbit simulations.

Chapter 5

Dynamic aperture and frequency map analysis

This chapter contains the calculations of dynamic aperture and frequency map analysis. The choice of sextupole locations for chromaticity correction is discussed.

5.1 Dynamic aperture calculations

Dynamic aperture calculations are always connected with a trade-off between computation time and accuracy. Tracking a whole six dimensional phase space can take easily weeks, months, and even year depending on its density and number of turns. Thus a proper reduction of the problem is inevitable.

Several restrictions had to be made to fit within the available computation time and power:

- The phase space of start coordinates of all particles has been restricted to the x,y-plane which is a common procedure [24]. Cross checks have been performed to prove this restriction to be valid.

- The dynamic aperture calculations are limited to the short term regime which ranges from several hundreds to a few thousands of turns. This is justified by the kind of investigation performed in this thesis. The betatron motion and related resonances which are driven by field errors of the magnets develop in this range of turns [25]. Furthermore 2000 turns are sufficient to calculate the diffusion coefficient [26].

- The relative momentum deviation is also taken into account but for discrete values only. Calculations have been performed for on-momentum particles and off-momentum particles with a maximum relative momentum deviation of $\pm 3\sigma$.

The particle tracking starts at the place of the geometric acceptance limit which is located in the triplets around the target at the maximum beta functions. This allows a immediate comparison of the dynamic aperture with the geometric acceptance limit.

The calculation of the dynamic aperture is performed in the following way. The linear lattice is calculated by MAD-X and read into SIMBAD. The non-linearities caused by the field errors and sextupole magnets are introduced via thin non-linear kicks. The individual field errors of magnets are created by a pseudo random number generator and are Gaussian distributed. The seed of the generator can be and has been changed for statistical analysis. A grid of initial coordinates of particles is created in the x,y-plane. Using SIMBAD, particles are tracked through the HESR non-linear computer model for a specified amount of turns. The initial coordinates of surviving particles are transformed into transverse emittances using the twiss parameters. The boundary condition of equal transverse emittances restricts the dynamic aperture to be the largest circle covering the stable area in this emittance-based, two dimensional phase space.

The dynamic aperture calculations have been used to develop and optimize a chromaticity correction scheme using sextupoles and to optimize the field errors of the beam guiding magnets. There will be other non-linearities in the HESR which are not covered by this thesis e.g. space charge effects [19] or the non-linear kicks caused by the electron cooler's beam [86, 87]. They both act on longer time scales compared to the rising of betatron resonances.

5.2 Arrangement of sextupole magnets for chromaticity correction

Chromaticity leads to a tune spread induced by the momentum spread of the beam. Thus a chromaticity correction scheme had to be developed for the HESR [88]. Chromaticity can be corrected at places with non-zero dispersion only, which means that all sextupole magnets for chromaticity correction have to be installed in the arcs. Sextupole magnets are the lowest multipole creating non-linear forces. The non-linear effect on beam dynamics should be as small as possible or compensated if feasible to prevent the dynamic aperture from shrinking.

The use of driving term techniques did not lead to the desired results. This can be explained considering what follows. The dynamic aperture defines the border to the chaotic motion and thus is far away from the area where those techniques can be applied [89]. Furthermore, the sextupole magnets contribute to ten first order driving terms. All phase dependent driving terms require two families of sextupole magnets to be properly controlled. This adds up to 12 families of sextupole magnets for correction of the first order chromaticities and the geometric driving terms which drive

betatron resonances. This does not even regard e.g. second order dispersion. However, the HESR lattice does not provide for example the proper phase advances necessary for a driving term approach and there are not enough sextupole magnets to justify a splitting into the desired number of sextupole magnet families. Instead of a driving term approach, the effect of pairs of sextupole magnets on the dynamic aperture is evaluated. This means that the investigation searches for pairs of sextupole magnets whose effect the dynamic aperture is smallest. These pairs compensate best at design tunes for which this investigations have been performed. The calculations are based on the linear lattices ($\gamma_{tr} = 6.2$ and $\gamma_{tr} = 13.3$) and the sextupole magnets being the only non-linear elements.

The best compensating sextupole magnet pairs are different for both ion optical settings. Unfortunately, there are not enough of those pairs to fully correct chromaticities. Thus, additional pairs of sextupole magnets have to be included in the correction scheme. The simplest distribution of sextupole magnets consits of two families. One of these families contain only horizontal focussing sextupoles magnets and the other only vertical focussing ones. This is sufficient to correct chromaticities. If this distribution is further split to form a total of four families, the best compensating sextupole magnet pairs can be separated from the weaker compensating pairs. If lower currents are supplied to the weaker compensating sextupole magnet pairs, the negative effects on stability can be reduced.

The chromaticity correction scheme consists of 12 horizontal focussing and of 14 vertical focussing sextupole magnets per arc. The additional four sextupole magnets are necessary since the shape of the horizontal dispersion function is different for both ion optical settings (see Figure 3.4).

The dynamic aperture was calculated for both ion optical settings and with two and four sextupole families. The dynamic aperture of the $\gamma_{tr} = 6.2$ lattice could be increased from $817\,mm\,mrad$ to $1125\,mm\,mrad$ by using four families. The dynamic aperture of the $\gamma_{tr} = 13.3$ is in general much smaller. It is $79\,mm\,mrad$ for the design tunes. A different choice of tunes can help to increase this value. It is extremely complicated to determine if the tunes in general or the phase advances between the sextupole magnets are worse than for the $\gamma_{tr} = 6.2$ lattice. Even so, it is possible to improve the dynamic aperture with the same four sextupole families with different strengths. The maximum improvement achieved is in the order of 15% with a value of $91\,mm\,mrad$.

5.3 Field errors of the HESR magnets

Since no magnet can be designed and built to provide the desired ideal magnetic field configuration like a pure dipole field, field errors have to be taken into account.

Dipole magnet 3D field calculations have been used to estimate the field errors of the dipole magnets [90] and provide upright field components only (see Table 5.1). The dipole magnet is optimized for $1\,T$ which is reflected by the corresponding relative field errors being smaller than 10^{-4}. For different field straights, some relative field errors may increase by more than one order of magnitude.

	First design			Optimized design		
Component	$0.17\,T$	$1.0\,T$	$1.7\,T$	$0.17\,T$	$1.0\,T$	$1.7\,T$
4-pole	-0.03	0.01	0.10	-0.03	0.01	0.10
6-pole	-4.32	0.72	28.16	-1.57	0.88	3.52
8-pole	0.04	0.06	0.09	0.04	0.06	0.09
10-pole	-1.62	-0.05	6.03	-0.44	0.53	7.96
12-pole	0.01	0.01	0.01	0.01	0.01	0.01
14-pole	-0.06	0.10	0.43	0.03	0.13	0.79
16-pole	$< 10^{-2}$	$< 10^{-2}$	$< 10^{-2}$	$< 10^{-2}$	$< 10^{-2}$	$< 10^{-2}$
18-pole	0.06	0.04	-0.10	0.06	0.05	-0.23
20-pole	$< 10^{-2}$	$< 10^{-2}$	$< 10^{-2}$	$< 10^{-2}$	$< 10^{-2}$	$< 10^{-2}$

Table 5.1: Relative field errors of the bending dipole magnet retrieved from 3D calculations. All values are in units of 10^{-4}. Field errors are upright only. The field of $0.17\,T$ corresponds to $1.5\,GeV/c$, $1.0\,T$ to $8.9\,GeV/c$, and $1.7\,T$ to $15\,GeV/c$ respectively. The reference radius of this multipole expansion is $33\,mm$.

The first dipole magnet design inherited a sextupole field component with a relative strength of $b_2 = 28.16 \cdot 10^{-4}$ at $1.7\,T$ main field. Such a sextupole field component affects chromaticity heavily. The integrated sextupole field strength of a dipole magnet at $1.7\,T$ is with a value of nearly $0.75\,m^{-2}$ roughly three times larger than the maximum integrated strength of a single sextupole magnet (see paragraph 3.2.2). The resulting chromaticities were in the order of $\xi_x > 70$ and $\xi_y < -70$, which the dedicated sextupole magnets were not able to compensate.

Thus the dipole magnet design has been further optimized. Gaps have been introduced into the iron yoke to improve the relative sextupole field component at $1.7\,T$ main field. A reduction by roughly a factor eight to $b_2 = 3.52 \cdot 10^{-4}$ has been achieved [57]. The chromaticities changed to $\xi_x \approx -4.80$ and $\xi_y \approx -17.96$ for the improved sextupole field component at$1.7\,T$ main field. The sextupole field component at $0.17\,T$ decreased by roughly a factor three resulting in chromaticities which are very close to the natural chromaticities. A small drawback of the optimization of the dipole magnet design is the increase of the relative decapole field component by approximately 32% to $b_4 = 7.96 \cdot 10^{-4}$ at $1.7\,T$ main field. At $0.17\,T$ the relative decapole decreased by nearly by a factor four. In general, the relative field errors are smaller than $1 \cdot 10^{-4}$ except for the sextupole and decapole field components.

For the following dynamic aperture calculations which take field errors into account, the field errors for $1.7\,T$ and $0.17\,T$ have been used.

Quadrupole magnet The HESR quadrupole magnet design is based on the COSY quadrupole magnets. The estimated field errors of the HESR quadrupole magnets will be roughly 10% higher [58] than the measured field errors of the COSY quadrupole magnets shown in Table 5.2. The increase is caused by the four-part yoke of the HESR quadrupole magnets compared to the COSY ones having a two-part yoke. The increase is taken into account for all calculations.

	$200\,A$		$550\,A$	
Component	Normal	Skew	Normal	Skew
6-pole	0.37 ± 0.33	0.91 ± 0.21	1.75 ± 0.24	4.73 ± 0.67
8-pole	0.25 ± 0.63	2.05 ± 1.72	-1.13 ± 0.68	-0.02 ± 0.22
10-pole	-0.70 ± 0.28	0.91 ± 0.61	-0.13 ± 0.23	-0.09 ± 0.34
12-pole	-10.33 ± 0.82	10.28 ± 0.47	49.03 ± 2.14	13.37 ± 0.41
14-pole	-0.73 ± 0.20	2.82 ± 2.25	-1.17 ± 0.26	-1.17 ± 0.19
16-pole	3.19 ± 0.38	6.51 ± 0.58	3.08 ± 0.29	5.49 ± 0.54
18-pole	-0.09 ± 0.40	0.03 ± 0.66	0.02 ± 0.16	0.22 ± 0.15
20-pole	83.66 ± 0.83	2.99 ± 0.81	107.76 ± 0.62	3.34 ± 0.25

Table 5.2: Relative field errors of COSY quadrupole magnets. All values are given in units of 10^{-4}. The errors of quadrupole magnets do not include the 10% increase due to the iron yoke of the HESR type. The reference radius of this multipole expansion is $70\,mm$. The currents of $200\,A$ and $550\,A$ correspond to field gradients of approximately $3.6\,T/m$ and $10\,T/m$ respectively.

Although there exist measurements also for the current of $400\,A$ which is closer to the maximum current used in the HESR, it was preferred to use $550\,A$ for a worst case estimate due to saturation effects and the different gradients. The largest relative field errors are by far the errors of the 12- and of the 20-pole. For the highest current of $550\,A$ the normal 12-pole relative field component has a strength of $b_5 = 49.03 \cdot 10^{-4}$. The 20-pole relative field component is by more than a factor two larger than that of the 12-pole. All other field components are smaller than $5.5 \cdot 10^{-4}$ except from the skew 12-pole ($a_5 = 13.37 \cdot 10^{-4}$). For low currents near $200\,A$, the absolute value of normal and skew 12-pole relative field component are almost equal ($b_4 \approx -a_4 \approx 10 \cdot 10^{-4}$). The 20-pole is still dominant being approximately a factor eight larger than the 12-pole.

5.4 The $\gamma_{tr} = 6.2$ lattice

The most frequently used ion optical setting will be the $\gamma_{tr} = 6.2$ lattice. This is justified by the main PANDA experiment. Therefore a

simulation for $15\,GeV/c$ is a worst case estimate due to field errors and important for possible future upgrades. The geometric emittance is $\varepsilon = 0.0637\,mm\,mrad$ ($\varepsilon_{norm} = 1\,mm\,mrad$) at $15\,GeV/c$ or $\varepsilon = 0.107\,mm\,mrad$ at $8.9\,GeV/c$. The emittance at $15\,GeV/c$ is used in the following. The field errors which are taken into account are errors of the dipole magnet at $1.7\,T$ main field and of the quadrupole magnet at $550\,A$. The design tunes are $Q_x = 7.618$, $Q_y = 7.624$.

5.4.1 Tune scans

While the frequency map analysis indicate which resonances are driven at a specific tune setting, a tune scan provides information about strongest resonances over a whole area in the tune diagram. Since momentum spread and other effects can lead to coherent and incoherent tune spread, tune scans are also used to find tune areas with enough space and large dynamic aperture. Such a tune scan for $\frac{\Delta p}{p} = 0$ is shown in Figure 5.1.

The strongest resonance seen in the tune scan corresponds to the octupole resonance line $2 \cdot Q_x + 2 \cdot Q_y = 31$. This can be indeed a fourth order resonance driven mainly by the 12- and 20-pole field components of the quadrupole magnets. The resonance line which is referred as the skew octupole resonance $3 \cdot Q_x + Q_y = 31$ is presumably the eighth order resonance $6 \cdot Q_x + 2 \cdot Q_y = 62$. This reflects the fact that the skew field components of the quadrupole magnets are relatively small compared to the upright ones. The main contribution to the first fourth order resonance line at $2 \cdot Q_x + 2 \cdot Q_y = 31$ can also be the eighth order resonance $4 \cdot Q_x + 4 \cdot Q_y = 62$ or an overlap of both. A separation is almost impossible since different driving terms contribute to the resonances.

For example, the resonance line $2 \cdot Q_x + 2 \cdot Q_y = 31$ is a fourth order resonance. The corresponding first order octupole driving term is h_{20200}. The 12-pole first order driving terms which contribute to the very same resonance are h_{31200} and h_{20310}. For the 20-pole there are the four coorresponding driving terms h_{53200}, h_{42310}, h_{31420}, and h_{20530}. Other multipole field components can also contribute in first order. Since the resonance lines $4 \cdot Q_x + 4 \cdot Q_y = 62$ and $2 \cdot Q_x + 2 \cdot Q_y = 31$ overlap, even more driving terms are relevant. The driving terms h_{51400} and the h_{40510} are the corresponding first order 20-pole driving terms. Even so, all those driving terms contribute in first order solely. Higher orders can and do also contribute, e.g. two sextupole driving terms contribute to octupole driving terms and thus to fourth order resonances.

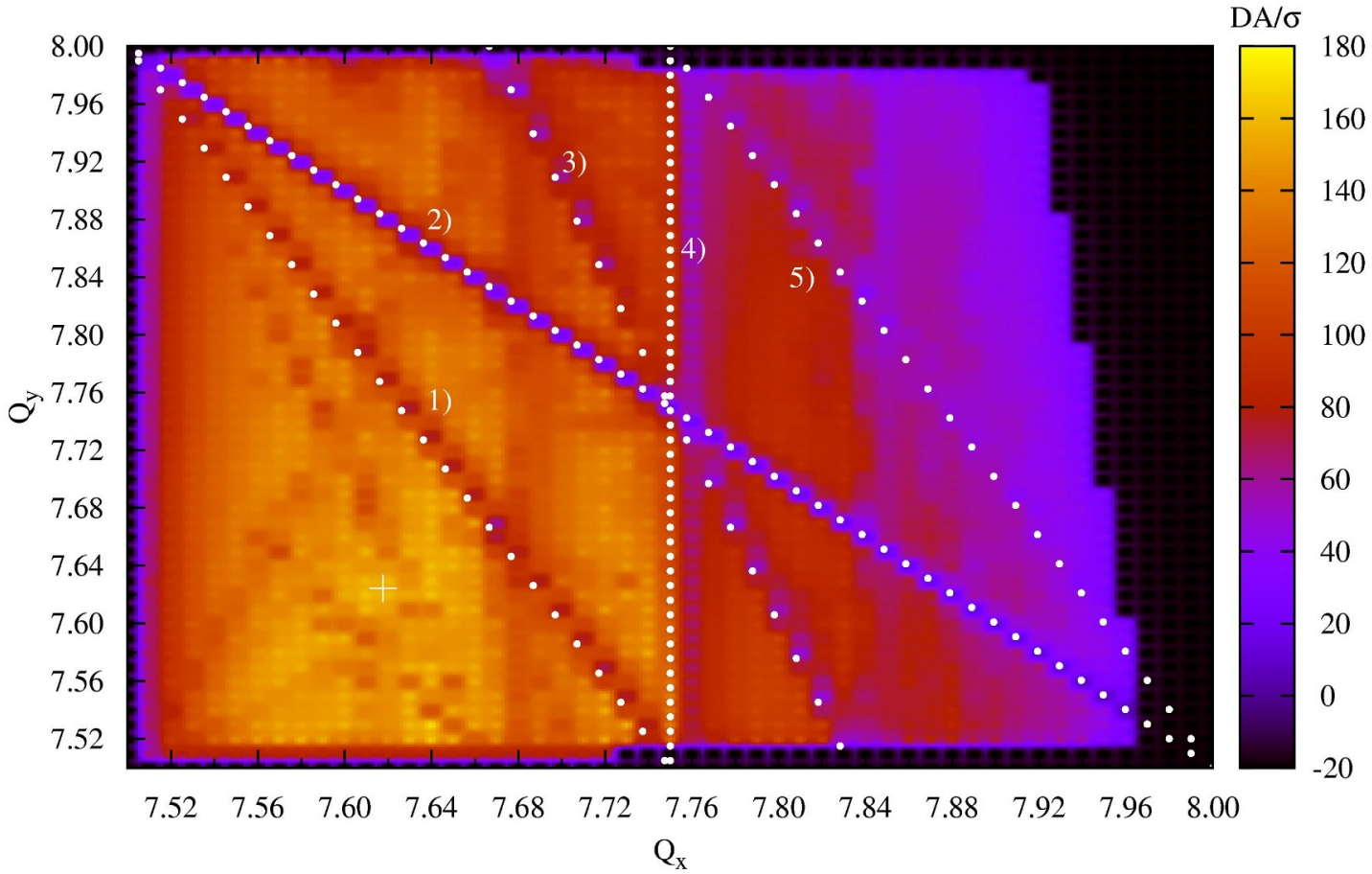

Figure 5.1: Tune scan for DA/σ and on-momentum particles tracked over 1000 turns. DA/σ is the dynamic aperture divided by the 1σ emittance. The value of -20 is artificial and represent an unstable linear lattice. It is used to separate unstable tunes of the linear modell from zero dynamic aperture. The strongest resonance lines have been identified and marked: 1) Skew Sextupole $2 \cdot Q_x + Q_y = 23$; 2) Octupole $2 \cdot Q_x + 2 \cdot Q_y = 31$; 3) Skew Octupole $3 \cdot Q_x + Q_y = 31$; 4) Octupole $4 \cdot Q_x = 31$; 5) 12-pole $4 \cdot Q_x + 2 \cdot Q_y = 47$. The design tunes are marked by a cross.

Coming back to the resonance identification, also the resonance line indicated as $2 \cdot Q_x + Q_y = 23$ belongs most likely not to a skew sextupole resonance. The next higher order resonance overlapping is the sixth order resonance $4 \cdot Q_x + 2 \cdot Q_y = 46$ which would correspond to the strong 12-pole component in the quadrupole magnets. A confirmation of this interpretation is provided by the other sixth order resonance $4 \cdot Q_x + 2 \cdot Q_y = 47$ which is marked as 5 in the tune scan.

The resonance line $4Q_x = 31$ can be observed slight shifted to the horizontal integer tune. From the resonance condition, it should be located at $Q_x = 7.75$ as the dotted line indicates. Instead, the resonance line is moved to approximately $Q_x = 7.76$. This is partly caused by the grid density of tunes and the data processing. A closer look reveals that the resonance seems to be shifted indeed and also asymmetric. The left shoulder of the resonance has a steeper fall than the right one. The same can be observed for the third order resonance $3Q_x = 23$ at $Q_x = 7.68$ which is one of the weaker resonances. Similar behavior could be observed during the development of the chromaticity correction scheme. Simulations with a single sextupole and a single octupole magnet have shown that this resonance line can be shifted depending on the octupole strength. Also the shapes of the shoulders and the depth of the resonance changed with the octupole magnet strength. This is caused by a frequency mixing which affects the resonance characteristics.

The dynamic aperture decreases when approaching the horizontal integer resonance $Q_x = 8$. This can be explained by a mismatch of the arcs and straight sections leading to large beta functions in the triplets around the target. This translates via increase of beam size together with the field errors in the quadrupole magnets to stronger non-linearities and results in a decrease of the dynamic aperture. The dynamic aperture shrinks until even the linear lattice becomes unstable due to the mismatch. This is denoted by a black area on the right hand side near the integer resonance. Since the design tune and thus the tune area of main interest is far from being integer, this constitutes no restriction.

The relation of geometric acceptance limit and dynamic aperture cannot be displayed in a two-dimensional tune scan. A reduction to a one-dimensional tune scan, e.g. with one of the tunes kept fixed, can be an appropriate way for such a comparison. Two examples of this kind of tune scans are shown in Figure 5.2.

The tune scan reflects the behavior of the linear lattice. The change of tunes lets the maximum beta functions grow due to the mismatch which reduces the geometrical acceptance limit until the linear lattice becomes unstable. This happens close to the integer or the half integer tune values in the case of the horizontal tune being fixed. It also shows a linear decrease of the geometric acceptance limit. For a fixed vertical tune it is different. The decrease is not linear and the transition to an unstable linear lattice occurs further away from the integer tune value. In general,

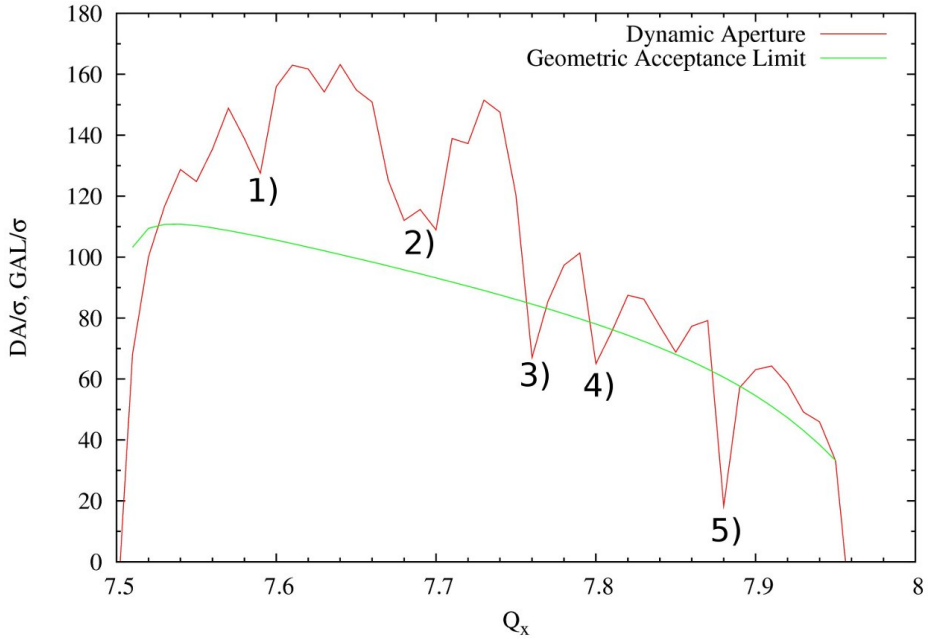

(a) Tune scan with vertical tune fixed at $Q_y = 7.62$

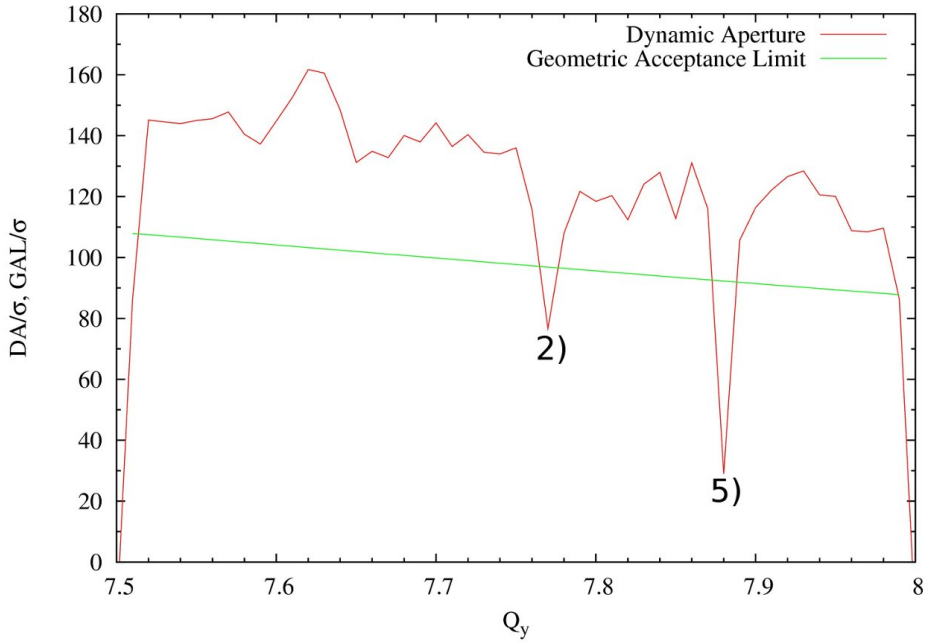

(b) Tune scan with horizontal tune fixed at $Q_x = 7.62$. The mark 2) refers in this case to resonance line $2 \cdot Q_x + Q_y = 23$ only.

Figure 5.2: Tune scan for one of the tunes kept fixed at $Q_{x,y} = 7.62$. The geometric aperture plotted in green shows the described increase of maximum beta functions until the linear lattice becomes unstable. Strongest resonance lines have been identified using 2D tune scan: 1) $6 \cdot Q_x + 4 \cdot Q_y = 77$; 2) overlap of resonances lines $2 \cdot Q_x + Q_y = 23$ and $3 \cdot Q_x = 23$; 3) $4 \cdot Q_x = 31$; 4) $3 \cdot Q_x + Q_y = 31$; 5) $2 \cdot Q_x + 2 \cdot Q_y = 31$

the linear lattice is clearly more sensitive to changes of the horizontal tune. The consideration of the geometrical acceptance limit is an advantage of this kind of data representation since it also provides information on the available acceptance margin. Although one-dimensional tune scans show a resonance structure, an identification of resonances is easier to perform using two dimensional tune scans. Although it is possible to estimate the depth and width of resonances from one dimensional tune scans, the direction of approaching the resonances and possible overlap make things difficult.

5.4.2 Design tunes

The design tunes of the $\gamma_{tr} = 6.2$ lattice are $Q_x = 7.618$, $Q_y = 7.624$ and therefore close to the $Q_x - Q_y = 0$ skew quadrupole difference resonance.

The frequency map analysis does not only provide information about tunes of single particles but also a stability criterion through the diffusion coefficient. The combination of tunes and diffusion coefficient in a single plot reveals the web of resonances[1] affecting particle stability. Furthermore the dynamic aperture is of another quality if combined with the diffusion coefficient since it transports resonance structures into the dynamic aperture plots. It also provide information about long-term stability.

Both types of plots are shown in Figure 5.3 for on-momentum particles ($\frac{\Delta p}{p} = 0$). The first plot shows the frequency map where a resonance knot can be seen at $Q_x = Q_y = 7.625$. A second resonance knot at $Q_x = Q_y = 7.666$ is too far away to be displayed. The strongest resonances have been identified and are marked by resonance lines. The resonance lines themselves can be identified by a tiplet of integers written at one end. A triplet is given in form of m, n, p which represents the resonance condition $m \cdot Q_x + n \cdot Q_y = p$. Resonances do not necessarily correlate with the order of a multipole driving it although first order effects are in general the strongest.

The resonance web is split by the skew quadrupole difference resonance $Q_x - Q_y = 0$ into a main part on the left hand side and an island on the right hand side. This resonance is one of the strongest resonances dragging particles on and leaving only few particles around it. It also crosses both mentioned resonance knots. The resonance knot at $Q_x = Q_y = 7.625$ is the closest to the design tunes. Most of the relevant resonances which cross this resonance knot are of eighth order.

This is reflected by eight hyperbolic fixpoints in the chaotic region of the horizontal phase space plots in Figure 5.4. The phase space plots show a thin chaotic layer inside the stable region. This layer is located at $15\,mm$ which is close to the transition of the very stable, dark blue area in the dynamic aperture plot to lighter blue. The KAM tori broaden in the

[1] so called Arnold web [29]

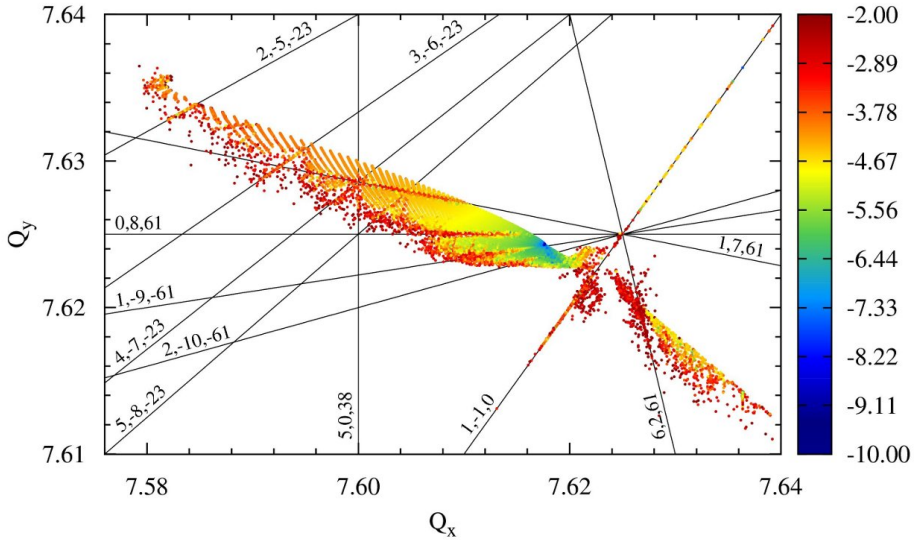

(a) Frequency Map with identified resonances

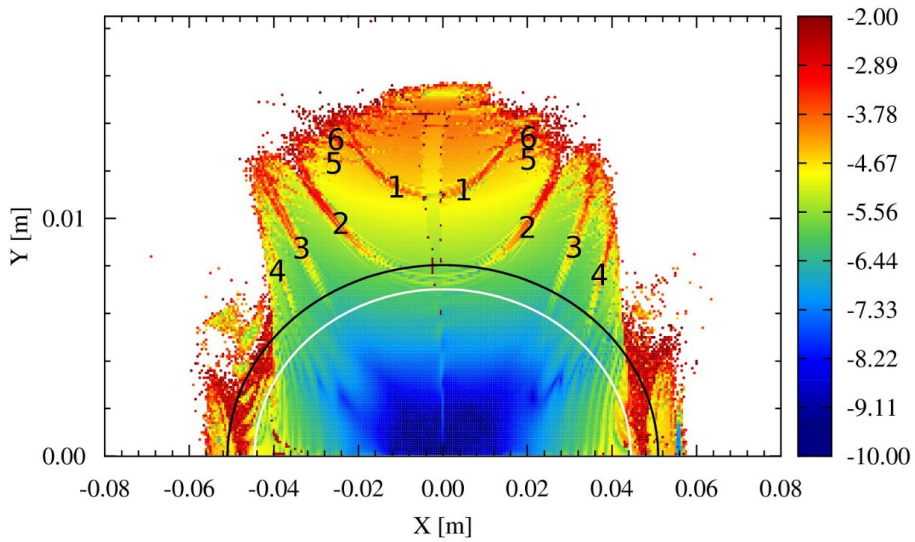

(b) Dynamic aperture

Figure 5.3: Frequency map and corresponding dynamic aperture for $\frac{\Delta p}{p} = 0$. The color scale represent the diffusion coefficient. The two curves in b) represent emittances at the geometrical acceptance limit (white) and at the dynamic aperture (black). The numbers in b) denote the resonances: 1) 1,7,61; 2) 0,8,61; 3) 1,-9,-61; 4) 2,-10,-61; 5) 5,-8,-23; 6) 4,-7,-23

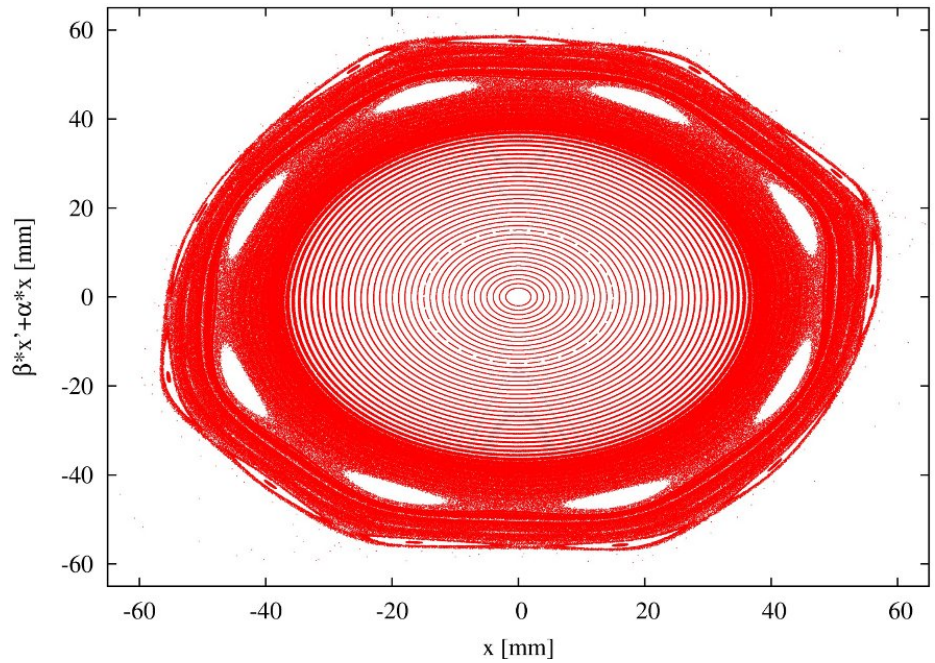

(a) Phase space with canonical variables

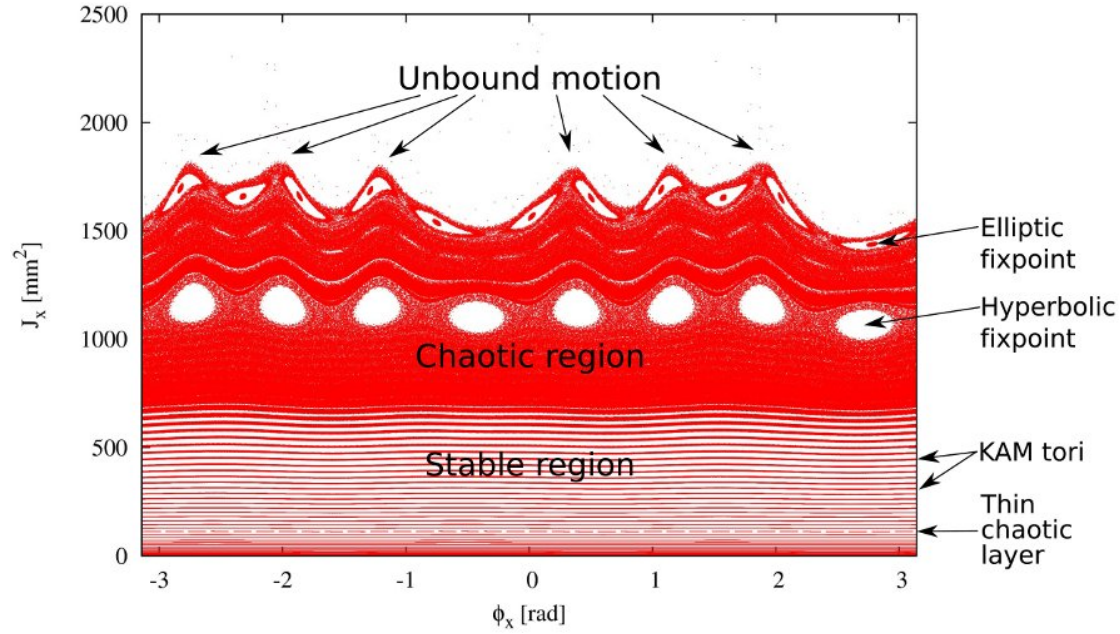

(b) Phase space with action-angle variables

Figure 5.4: Horizontal phase space plot for $\gamma_{tr} = 6.2$ lattice at design tunes. Particles with no initial momenta ($p_x = p_y = 0$), a fixed vertical coordinate of $y = 1\,mm$, and a positive x with a step size of $1\,mm$ are tracked over 50000 turns to fill the phase space. Plot a) shows the horizontal phase space where the axes are $\beta_x \cdot p_x + \alpha_x \cdot x$ versus x so that the regular KAM tori become circles and are not elliptic. Plot b) shows the same phase space but transformed to action-angle variables.

outer region of the stable area. The KAM tori open out at the transition to the chaotic region. This happens at nearly 36 mm where the first yellow stripe appears in the dynamic aperture plot. Besides the eight hyperbolic fixpoints, there are also eleven elliptic ones further outside. Based on the knowledge about the strong 20-pole field component of the quadrupole magnets, it is extremely probable that this eleven islands reflect a eleventh order resonance driven by this field components in second order. Also the strong 12-pole field components can be observed. The outer shape of the phase space plot a) is almost hexagonal. This is shown even more clearly in plot b) where from the six "hills" particles move away and enter the region of unbound motion. In this region the amplitude can grow without limit and the particles are going to be lost.

Figure 5.5 provide a closer look on the main part of Figure 5.3a and reveals the existence of weaker resonances within the resonance web.

The dynamic aperture plot demonstrates clearly the advantage of the diffusion coefficient when used together with dynamic aperture: The diffusion coefficient provide information about long-term stability even with a short-term dynamic aperture. Furthermore the resonance structure seen in the frequency map is transferred to the dynamic aperture. With the knowledge about the resonance lines in the frequency map, an identification in the dynamic aperture plot is straight forward. A mapping of those resonance lines which are easy to see in the dynamic aperture plot is listed in the caption of Figure 5.3.

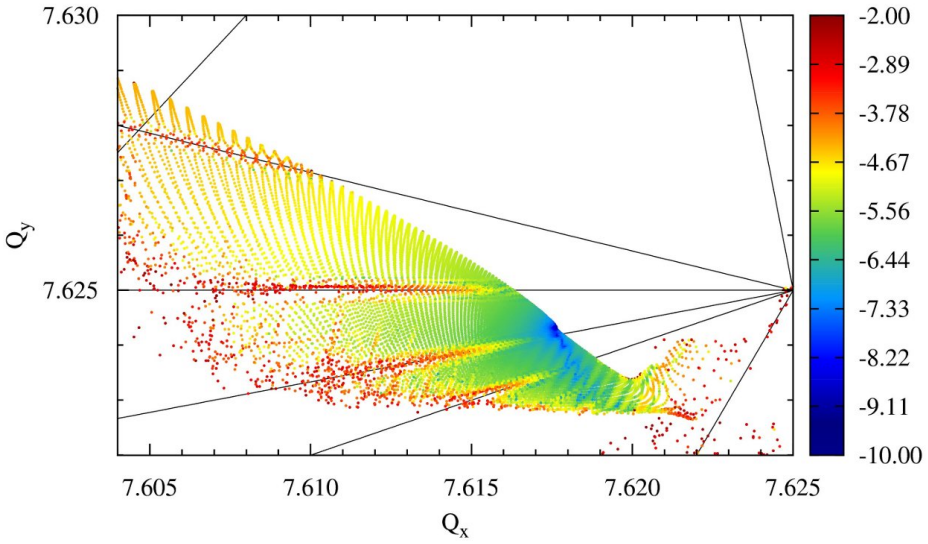

Figure 5.5: Enlarged view on main parts of frequency map of Figure 5.3a. The color scale represent the diffusion coefficient. The strong resonance lines are marked by black lines although without a triplet identification. Weaker resonances within the resonance web can also be observed.

The dynamic aperture plot does not show an island like the frequency map but presents two structures on the left and right of the "main" area with a more or less clear cut transition. These two structures contain particles on the island and on the skew quadrupole resonance. Although the dynamic aperture seems to be symmetric, there are some irregularities, e.g. the shapes of the structures left and right and of the upper left part. The geometrical acceptance limit is $6.63\,mm\,mrad$ (approximately $104\,\sigma$) and is marked with a white curve. The dynamic aperture is marked with a black curve. The emittance which corresponds to the dynamic aperture is $8.67\,mm\,mrad$ (roughly $136\,\sigma$).

There is an obvious deformation in the central and the upper region of the dynamic aperture plot. It is framed by dark red points reflecting chaotic behavior. The particles within this areas reside on a sextupole or a decapole resonance line. The strongest resonances which can be easily seen in the dynamic aperture plot are crossing the resonance knot at $Q_x = Q_y = 7.625$ and are marked with numbers 1 to 4. Stronger resonances hardly reach into the geometric acceptance limit.

A momentum deviation can lead among other things to tune shifts and to changes of the closed orbit due to dispersion. A value of $3 \cdot 10^{-4}$ was chosen for the momentum deviation, which corresponds to three times the rms momentum spread of the high luminosity mode. The results can be seen in Figures 5.6 and 5.7.

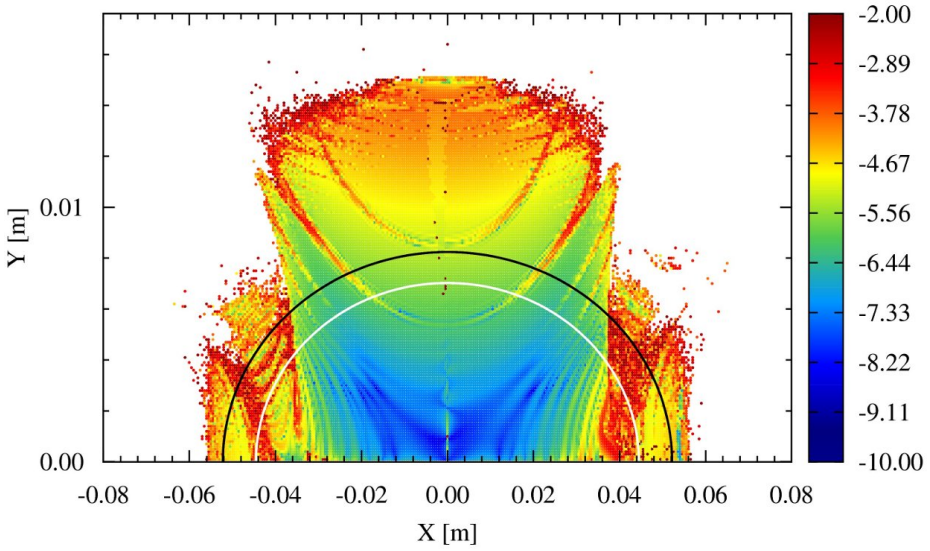

Figure 5.6: Dynamic aperture for off-momentum particles with a momentum deviation of $\frac{\Delta p}{p} = +3 \cdot 10^{-4}$. The color scale represent the diffusion coefficient. The geometric acceptance limit is given as a white line whereas the dynamic aperture as a black one.

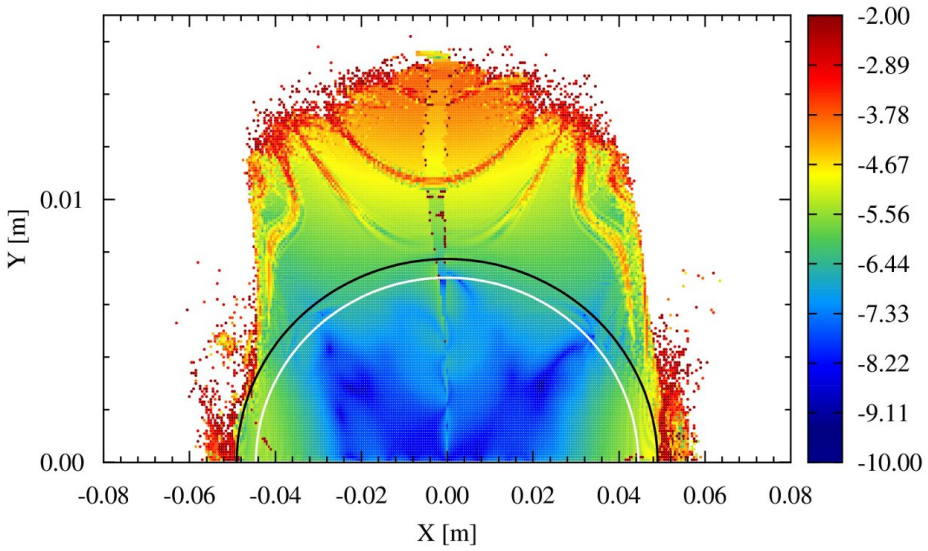

Figure 5.7: Dynamic aperture for off-momentum particles with a momentum deviation of $\frac{\Delta p}{p} = -3 \cdot 10^{-4}$. The color scale represent the diffusion coefficient. Some resonances are distorted. The geometric acceptance limit is given as a white line whereas the dynamic aperture as a black one.

For $\frac{\Delta p}{p} = 3 \cdot 10^{-4}$ the dynamic aperture is not reduced but increased to $9.12\,mm\,mrad$ (approximately $146\,\sigma$). Although the value of the dynamic aperture increased, the resonance line $8 \cdot Q_y = 61$ reaches into the geometric acceptance limit. The main part of the dynamic aperture is smaller in width. The unstable areas from the structures left and right are now within the geometrical acceptance limit. Furthermore the inner area with long-term stability decreased significantly.

The relative momentum offset of $\frac{\Delta p}{p} = -3 \cdot 10^{-4}$ also shows a changed situation. The dynamic aperture is reduced $8.03\,mm\,mrad$. The structures on both sides are smaller. The resonance line $1 \cdot Q_x + 7 \cdot Q_y = 61$ moved further into the unstable area at the top of the dynamic aperture plot. The resonance lines at the sides of the dynamic aperture plot are distorted. This distortion is caused by a folding inside the frequency map. Such a folding can appear if terms of higher degrees in the Hamiltonian become dominant over the quadratic terms. Stable areas can be folded on resonance lines which then provide particles a way of fast orbit diffusion [91]. The folding can be observed in the lower right corner of the main part in the frequency map. A view on this folded area in the frequency map is shown in Figure 5.8.

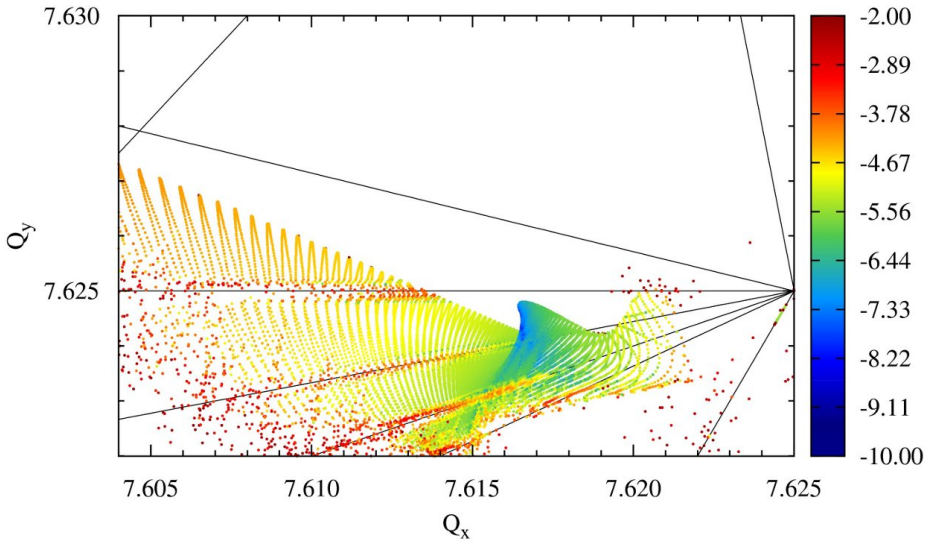

Figure 5.8: Folding of frequency map for $\frac{\Delta p}{p} = -3 \cdot 10^{-4}$. The color scale represent the diffusion coefficient.

The edge of the frequency map is folded near the $2 \cdot Q_x - 10 \cdot Q_y = -61$ resonance line. Due to the folding, two different areas are crossed by a resonance line in the same tune area. Figure 5.9 shows the dynamic aperture plot 5.7 again where particles are colored black if their tunes are confined within a tune range of $\Delta Q = 5 \cdot 10^{-4}$ around a specified resonance line. This has been done for the resonance lines $1 \cdot Q_x - 9 \cdot Q_y = -61$ and $2 \cdot Q_x - 10 \cdot Q_y = -61$. Plot a) does not highlight a deformation of a resonance line but clarifies that two separated areas in the dynamic aperture plot are crossed by a resonance line at the same location in tune space. The real resonance is the upper black area whereas the one below is inside the folded stable area. Plot b) shows how the resonance line $2 \cdot Q_x - 10 \cdot Q_y = -61$ is bent outwards.

The presented values of the dynamic aperture of the $\gamma_{tr} = 6.2$ lattice for the different momentum deviations have been determined for one specific set of field errors. The calculations have been repeated with 99 other seeds for the pseudo random number generator. The statistics for all 100 sets is given in Table 5.3.

$\Delta p/p$	$-3 \cdot 10^{-4}$	0	$3 \cdot 10^{-4}$
DA $[mm\,mrad]$	7.95 ± 0.09	8.54 ± 0.05	8.99 ± 0.04
DA $[\sigma]$	124.80 ± 1.41	134.04 ± 0.77	141.13 ± 0.63

Table 5.3: Statistics of dynamic aperture calculations with 100 different seeds

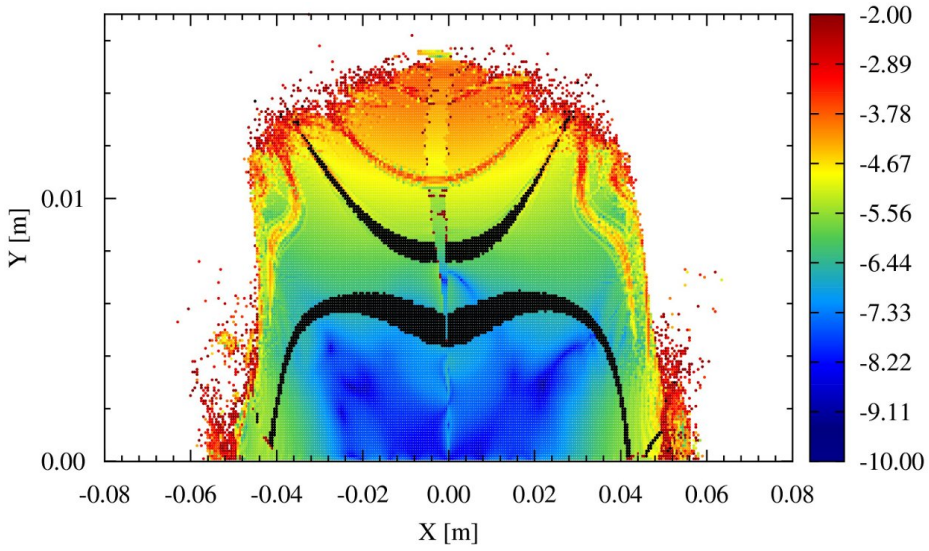

(a) $1 \cdot Q_x - 9 \cdot Q_y = -61$ (1,-9,-61)

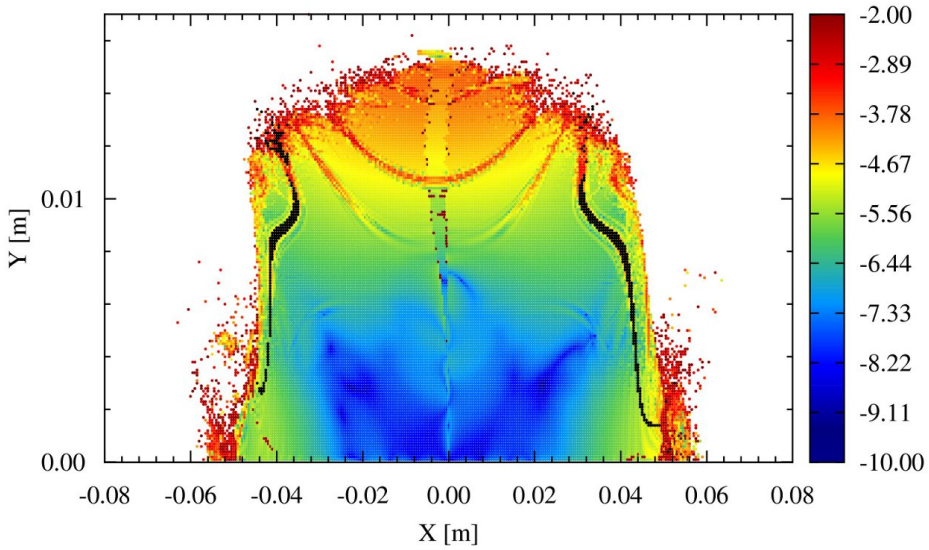

(b) $2 \cdot Q_x - 10 \cdot Q_y = -61$ (2,-10,-61)

Figure 5.9: Distortion of resonance lines in the dynamic aperture plot for $\frac{\Delta p}{p} = -3 \cdot 10^{-4}$. The color scale represent the diffusion coefficient. Black colored particles mark the specified resonance with a maximum distance of $5 \cdot 10^{-4}$ from the resonance in the frequency map.

5.4.3 Optimization

There are different ways to optimize the dynamic aperture. The two main ways are a different choice of tunes and the reduction of field errors. A third possibility though is the introduction of corrector magnets. These can be used to manipulate single resonances but introduce additional nonlinearities themselves. Therefore, this way of optimization is not always desirable.

Tunes As resonance driving terms depend on phase advances, a proper choice of tunes and thus also a change of phase advance can help to improve the dynamic aperture. In the following, two sets of tunes are suggested. At the tunes $Q_x = 7.615$, $Q_y = 7.605$, there exist no strong resonances which reach inside the geometric acceptance limit. At the other tunes at $Q_x = 7.568$, $Q_y = 7.582$, the dynamic aperture is increased by more than $1\,mm\,mrad$ (more than 15σ).

Figure 5.10a shows the dynamic aperture for on-momentum particles at the two different tune settings. For the first plot the tunes have been set to
$Q_x = 7.615$, $Q_y = 7.605$. The dynamic aperture could be determined to be $9.70\,mm\,mrad$ (approximately $152\,\sigma$). The dynamic aperture plot shows a structure at the upper end which is split in two pieces. The first guess that this structure is related to an island in the frequency plot which is split in half by a resonance could be verified to be true. The dynamic aperture plot shows also that none of the stronger resonances reaches inside the geometric acceptance limit. Although this is true even for off-momentum particles inside the $\frac{\Delta p}{p} = \pm 3 \cdot 10^{-4}$ boundary, the dynamic aperture changes with the momentum offset. The dynamic aperture is increased slightly to $9.88\,mm\,mrad$ for $\frac{\Delta p}{p} = 3 \cdot 10^{-4}$ and decreased by more than $0.5\,mm\,mrad$ to $9.07\,mm\,mrad$ for a momentum deviation of $\frac{\Delta p}{p} = -3 \cdot 10^{-4}$.

Dynamic aperture calculations have also been performed for the other tune setting at $Q_x = 7.568$, $Q_y = 7.582$. The dynamic aperture compared to the previous tunes is increased by 10.7% to $10.74\,mm\,mrad$ (approximately $169\,sigma$). For off-momentum particles, the dynamic aperture increases to $11.01\,mm\,mrad$ ($\frac{\Delta p}{p} = 3 \cdot 10^{-4}$) and $11.00\,mm\,mrad$ ($\frac{\Delta p}{p} = -3 \cdot 10^{-4}$). The dynamic aperture and frequency map for on momentum particles are shown in Figure 5.10b.

Field errors The investigations have shown that the field errors of the quadrupole magnet are dominant. The 12- and 20-pole field components of the quadrupole magnets are by far the strongest (see Table 5.2). In the following a series of reductions of both field errors has been performed. Since the quadrupole design has not been finished yet, this investiga-

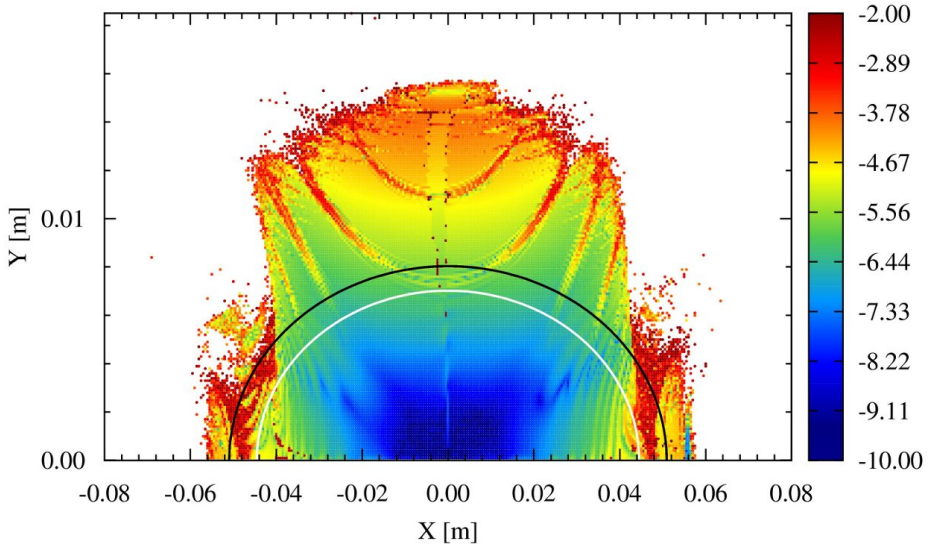

(a) Dynamic aperture for tunes $Q_x = 7.615$, $Q_y = 7.605$

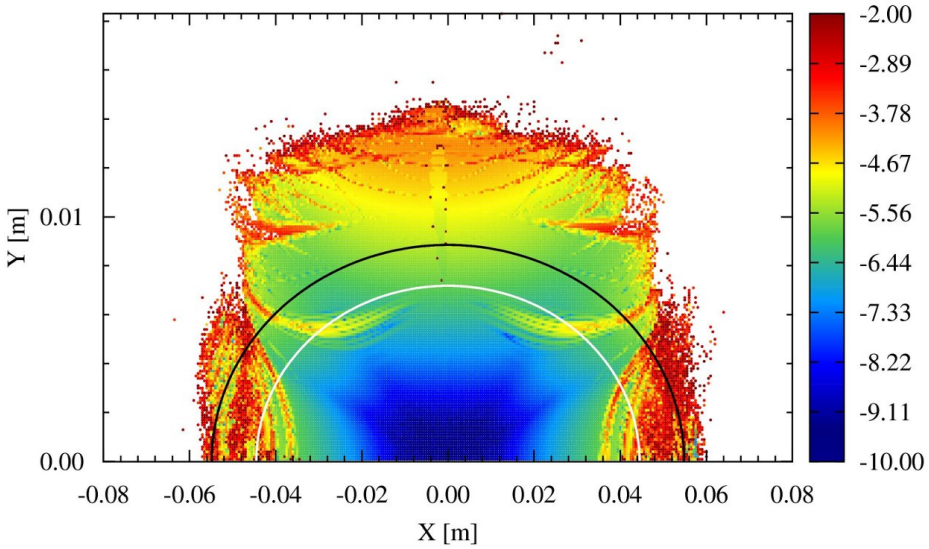

(b) Dynamic aperture for tunes $Q_x = 7.568$, $Q_y = 7.582$

Figure 5.10: Dynamic aperture for different tune settings a) $Q_x = 7.615$, $Q_y = 7.605$ and b) $Q_x = 7.568$, $Q_y = 7.582$. The color scale represent the diffusion coefficient. The geometric acceptance limit is given as a white line whereas the dynamic aperture as a black one.

tion was performed and the results will be incorporated in an optimized quadrupole design.

Already the tune scan reflected the strong 12- and 20-pole field components of the quadrupole magnet design. A reduction of both field components will help to increase the dynamic aperture on one hand and the area with long-term stability in the inner region on the other. The dynamic aperture has been calculated for reduced strengths of the 12- and 20-pole field components. The results of these reductions are shown in Table 5.4.

20-pole \ 12-pole	25.0	12.5	10.0	7.5	5.0
100.0	8.42	8.91	9.06	9.15	9.32
50.0	9.68	10.17	10.30	10.46	10.74
25.0	10.78	11.12	11.29	11.58	12.22
12.5	12.02	12.13	12.57	12.89	13.36
10.0	12.58	13.01	12.94	13.38	13.88
7.5	13.86	13.23	13.19	13.47	14.19
5.0	14.66	13.35	13.90	13.70	14.71

Table 5.4: Dynamic aperture calculated with 12- and 20-pole quadrupole field components at $15\,GeV/c$. The relative field errors include the 10% increase and are given in units of 10^{-4}. The dynamic aperture is given in $mm\,mrad$.

There are some dynamic aperture values which are smaller although the 12- and 20-pole field components are further reduced, for example the size of the dynamic aperture is $13.35\,mm\,mrad$ for $b_5 = 12.5 \cdot 10^{-4}$ and $b_9 = 5.0 \cdot 10^{-4}$ compared to $14.66\,mm\,mrad$ for $b_5 = 25.0 \cdot 10^{-4}$. This can happen due to the chaotic behavior outside the dynamic aperture. Since many driving terms may contribute to a single resonance, some of the driving terms can amplify or compensate each other.

Nevertheless, a clear tendency can be observed. The 20-pole field component restricts the dynamic aperture much more than the 12-pole field component. As one can expect if one field component is dominant, the reduction of the 12-pole field component lead to a smaller increase of the dynamic aperture. The size of the dynamic aperture is heading towards $15\,mm\,mrad$ with the reduction of the 20-pole field component. To further increase the dynamic aperture a simultaneous reduction of both multipole components has to be performed. Based on the reduction of the dipole magnets sextupole field component, a reduction of both strong field components of the quadrupole magnets by roughly a factor five appears to be reasonable. The 20-pole field component is set to $b_9 = 25 \cdot 10^{-4}$ while reducing the 12-pole field component to $b_5 = 10 \cdot 10^{-4}$. The resulting dynamic aperture for the design tunes is shown in Figure 5.11.

The dynamic aperture of $11.29\,mm\,mrad$ corresponds to approximately $183\,\sigma$. This is an increase by 30%. As the dynamic aperture plot shows, the area within the geometric acceptance limit is mostly colored blue with

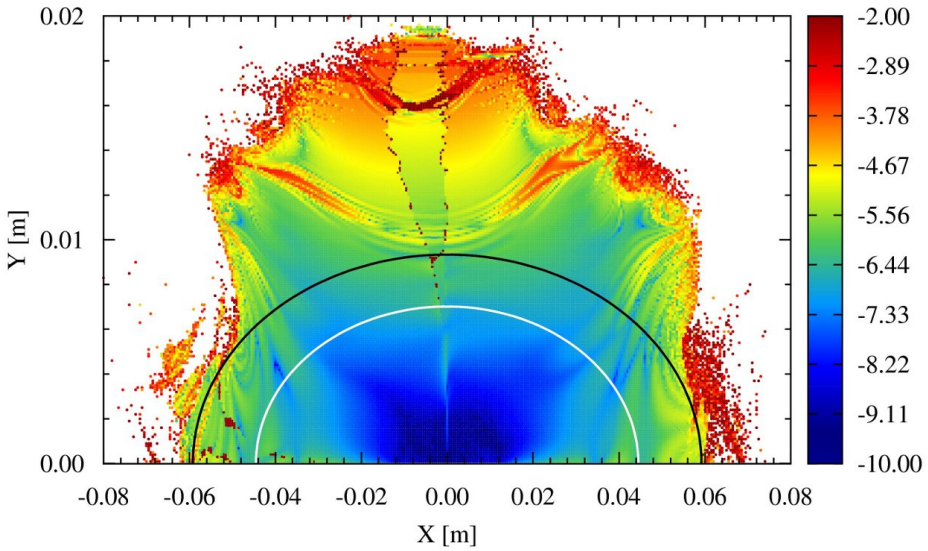

Figure 5.11: Dynamic aperture of $\gamma_{tr} = 6.2$ lattice with reduced quadrupole errors at design tune for on-momentum particles. The color scale represent the diffusion coefficient. The relative field errors of the 12- and 20-pole are reduced to $b_5 = 10 \cdot 10^{-4}$ and $b_9 = 25 \cdot 10^{-4}$. The geometric acceptance limit and the dynamic aperture are plotted with a white and with a black curve respectively.

only a few green parts which means that there are no strong resonances reaching inside and that the area with long-term stability has increased. The observed structure in the center of the plot is mainly created by the skew quadrupole difference resonance $Q_x - Q_y = 0$.

The frequency map with reduced multipoles is more compact and does not show the subtle web of resonances which appeared in the frequency map for full field errors. Nevertheless, the stronger resonances crossing the frequency map are still the same and remain easy to identify.

Combination of different tunes and reduced field components Better results can be achieved with the combination of both investigated optimization methods. Changing the tune settings while reducing the 12- and 20-pole field components can further improve the dynamic aperture. Taking again the same reduced field errors as before and setting the tunes to $Q_x = 7.568$, $Q_y = 7.582$, the dynamic aperture rises to $15.72\,mm\,mrad$ with none of the resonances reaching inside the geometric acceptance limit. The dynamic aperture is different for off-momentum particles: An increase to $15.86\,mm\,mrad$ for $\frac{\Delta p}{p} = 3 \cdot 10^{-4}$ and a decrease to $13.84\,mm\,mrad$ for $\frac{\Delta p}{p} = -3 \cdot 10^{-4}$. This means that the dynamic aperture is more than twice as large as the geometric acceptance limit even for off-momentum particles.

5.5 The $\gamma_{tr} = 13.3$ lattice

The other ion optical setting defined for the PANDA experiment is the $\gamma_{tr} = 13.3$ lattice. It will be used for the low energy region of the HESR in order to optimize the stochastic cooling. The following calculations assume an energy of $1.5\,GeV/c$. The geometric emittance is $\varepsilon = 0.637\,mm\,mrad$
($\varepsilon_{norm} = 1\,mm\,mrad$). The field errors which are taken into account are errors of the dipole magnet at $0.17\,T$ main field and of the quadrupole magnet at gradient of roughly $3.6\,T/m$ ($200\,A$). The design tune are chosen to be $Q_x = 7.614$, $Q_y = 7.615$.

5.5.1 Tune scans

A tune scan has also been performed for the $\gamma_{tr} = 13.3$ lattice and is displayed in Figure 5.12.

Compared to the $\gamma_{tr} = 6.2$ lattice, the $\gamma_{tr} = 13.3$ lattice is even more sensitive to mismatches which is exhibited by an increase of the black area. There is a general decrease of dynamic aperture when given in terms of 1σ-emittance. This is mainly due to the fact that the 1σ-emittance is by one order of magnitude larger caused by the lower energy. Resonances similar to those of the tune scan for the $\gamma_{tr} = 6.2$ lattice can still be observed. Although sextupole resonances are strong and the sextupole magnets for the chromaticity correction do not perform as good as for the $\gamma_{tr} = 6.2$ lattice, these sextupole resonance lines refer either to a 12-pole resonance or a sextupole resonance driven by the 12-pole field component. Since it is a simulation, certain multipoles can be excluded to confirm the assumption. Without the chromatic sextupole magnets, the resonance lines are nearly unchanged which is a strong indication that the resonance lines are not mainly driven by the sextupole magnets. The main contribution to these resonance lines also come from higher-order multipoles like 12- and 20-pole field components.

All upright sextupole resonance lines and the skew sextupole resonance line can be driven in first order by the 12-pole field component. The 20-pole field component can drive in first order the decapole resonance. All upright and skew octupole resonance lines can be 16-pole resonance lines driven in higher order by 12- and 20-pole field components.

5.5.2 Design tunes

The design tunes of the $\gamma_{tr} = 13.3$ lattice are $Q_x = 7.614$, $Q_y = 7.615$. This means that they are even closer to the difference resonance line $Q_x - Q_y = 0$ than the design tunes of the $\gamma_{tr} = 6.2$ lattice. The tunes being so close, a considerable influence of the skew quadrupole difference resonance $Q_x - Q_y = 0$ can be expected. This influence will affect the dynamic

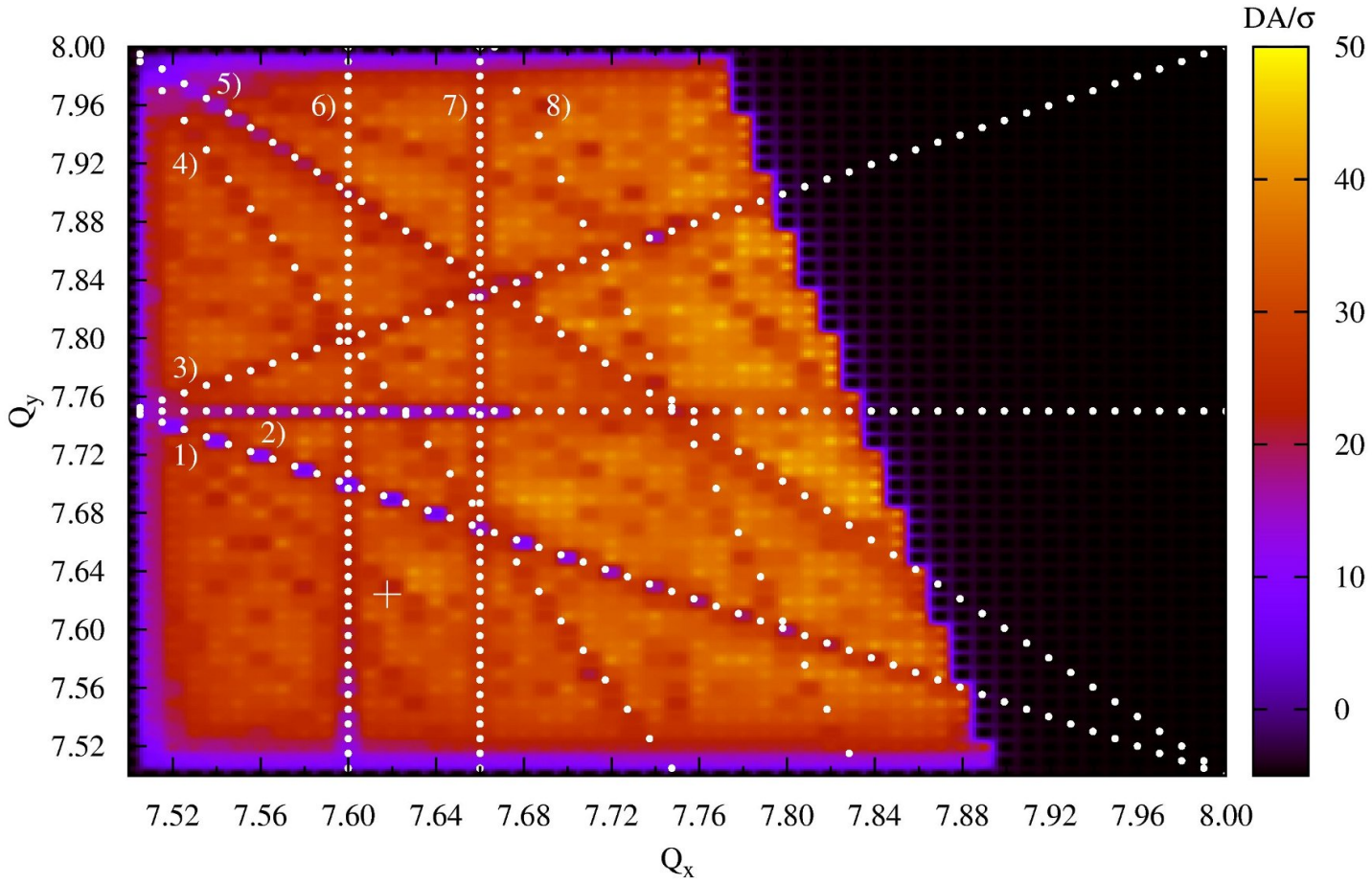

Figure 5.12: Tune scan for DA/σ lattice and 1000 turns. DA/σ represents the dynamic aperture in terms of the 1σ emittance. The negative value (colored black) is not realistic but represent an unstable linear lattice and is used to separate unstable tunes of the linear modell from zero DA. The strongest resonance lines have been identified and marked: 1) Sextupole $Q_x + 2 \cdot Q_y = 23$; 2) Octupole $4 \cdot Q_y = 31$; 3) Sextupole $Q_x - 2 \cdot Q_y = -8$; 4) Skew Sextupole $2 \cdot Q_x + Q_y = 23$; 5) Octupole $2 \cdot Q_x + 2 \cdot Q_y = 31$; 6) Decapole $5 \cdot Q_x = 38$; 7) Sextupole $3 \cdot Q_x = 23$; 8) Skew Octupole $3 \cdot Q_x + Q_y = 31$. The cross indicates the design tunes.

aperture as well as the long term stability. The dynamic aperture can be seen in Figure 5.13.

From the dynamic aperture plot alone it should be clear that the design tunes have to be chosen differently when it comes to non-linear beam dynamics. The particles with long term stability are restricted to an area which is smaller than $\frac{1}{4}\sigma$. The dynamic aperture is $16.78\,mm\,mrad$ for on-momentum particles but increases for particles with a momentum deviation. The largest increase with a value of $17.95\,mm\,mrad$ happens for $\frac{\Delta p}{p} = -3{\cdot}10^{-4}$. A general growth of the dynamic aperture can be observed and can mainly be explained with the different ion optical setting where e.g. the field errors are smaller. Furthermore the maximum beta functions are smaller by a factor two: $150\,m$ compared to the $300\,m$ of the $\gamma_{tr} = 6.2$ lattice. The maximum beta functions in x and y have similar values. This is reflected by the fact that the dynamic aperture is not longer dominated by the horizontal limit only. The vertical limit of the dynamic aperture is close to the edge of the stable area.

The frequency map demonstrates how close the design tunes are to the difference resonance. There is also a folding for on-momentum particles in the frequency map. The analysis of the phase space provide similar information as for the $\gamma_{tr} = 6.2$ lattice.

Since different tunes have to be chosen anyway, the dynamic aperture plot is not shown for off-momentum particles.

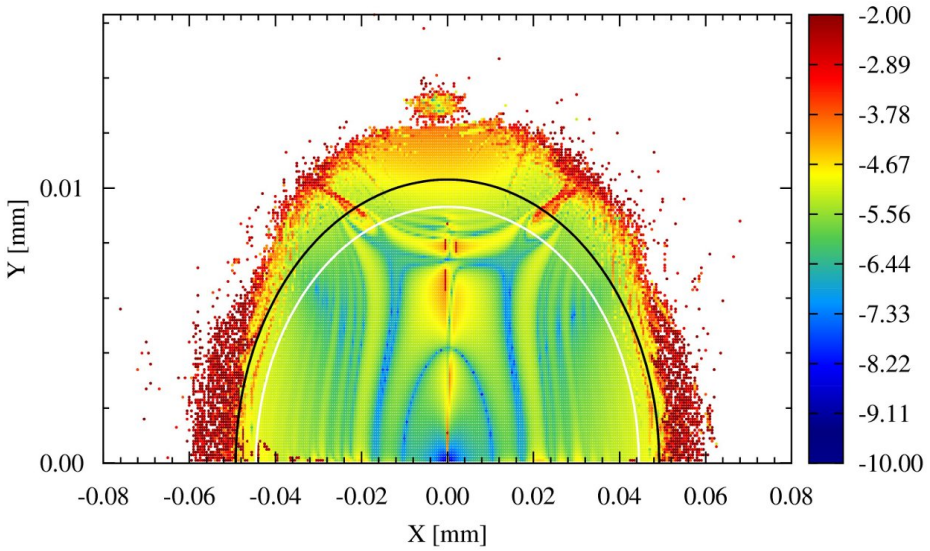

Figure 5.13: Dynamic aperture for on-momentum particles at design tune. The color scale represent the diffusion coefficient. Only a very small area with long-term stability is observed. The geometric acceptance limit is given as a white line whereas the dynamic aperture as a black one.

5.5.3 Optimization

The two main ways of optimization are covered again. The decrease of field errors and the different choice of tunes are investigated.

Tunes An area of large dynamic aperture and as close as possible to the design tune has been selected from the tune scan. This area is closely located to $Q_x = 7.630$, $Q_y = 7.640$. One of the best results has been found at
$Q_x = 7.637$, $Q_y = 7.647$. The dynamic aperture for on-momentum particles is $23.92\,mm\,mrad$ and can be seen in Figure 5.14. This is an increase by 45%. The increase for off-momentum particles is smaller and ranges from 12% for $\frac{\Delta p}{p} = 3 \cdot 10^{-4}$ to 19% for $\frac{\Delta p}{p} = -3 \cdot 10^{-4}$. The most important change is the increase of the area of long term stability which covers 3 to $4\,\sigma$. Also here the calculation have been repeated with different seeds. The results are shown in Table 5.5.

$\Delta p/p$	$-3 \cdot 10^{-4}$	0	$3 \cdot 10^{-4}$
DA $[mm\,mrad]$	21.43 ± 0.08	23.92 ± 0.07	18.92 ± 0.10
DA $[\sigma]$	33.65 ± 0.13	37.55 ± 0.11	29.70 ± 0.16

Table 5.5: Statistics of dynamic aperture calculations for tunes $Q_x = 7.637$, $Q_y = 7.647$ with 100 different seeds.

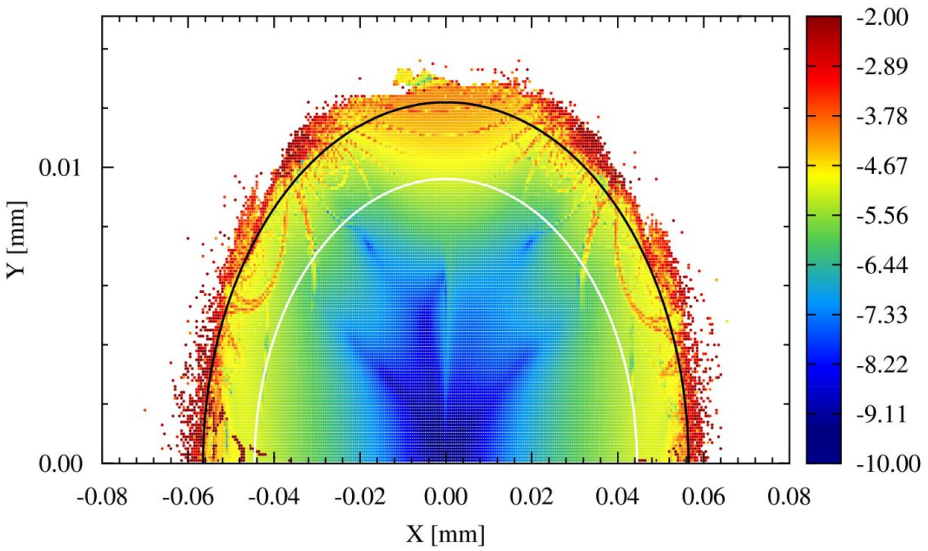

Figure 5.14: Dynamic aperture of the $\gamma_{tr} = 13.3$ lattice for tunes $Q_x = 7.637$, $Q_y = 7.647$. The color scale represent the diffusion coefficient. The geometric acceptance limit is given as a white line whereas the dynamic aperture as a black one.

Field errors The field errors at the lower energy limit are less problematic since the 12-pole field component of the quadrupole magnets is roughly a factor five smaller. Also the 20-pole field component is reduced by more than 20% ($b_9 = 92.03 \cdot 10^{-4}$ compared to the $b_9 = 118.54 \cdot 10^{-4}$). Nevertheless, the 20-pole field components is still absolutely dominant (see Table 5.6) and has to be reduced in order to increase the dynamic aperture and, what is probably more important, the area of long term stability. Since the design tunes had to be changed anyway, this investigation was carried out for the new tunes at $Q_x = 7.637$, $Q_y = 7.647$.

A reduction by a factor five appears to be reasonable also at $1.5\,GeV/c$. The 20-pole field component is therefore set to $b_9 = 20{\cdot}10^{-4}$. The resulting dynamic aperture for on-momentum particles has a size of $31.67\,mm\,mrad$ which is an overall increase of 89%. The dynamic aperture is up to 10.4% smaller for off-momentum particles, namely $27.77\,mm\,mrad$ for $\frac{\Delta p}{p} = 3 \cdot 10^{-4}$ and $26.31\,mm\,mrad$ for $\frac{\Delta p}{p} = -3 \cdot 10^{-4}$.

5.6 Multipole correction

The driving terms provide a way to access resonances. Manipulating the driving terms can be useful to correct certain resonances. For example, this method was applied at RHIC to preserve polarization [92]. This correction was performed using chromatic sextupole families. In contrast to RHIC, the number of sextupole magnet families in the HESR is not sufficient to manipulate the first order resonance driving terms of the sextupole magnets independently. Furthermore, the splitting into four families was based on dynamic aperture and not on resonance driving terms. This means that the phase advances do not fit to correct a specific resonance driving term. Considering this, there is only one way to access the sextupole first order driving terms. With the introduction of geometric sextupole magnets in the straight sections, a correction of sextupole driving terms can be performed independently of the chromatic sextupole magnets. However, there is one drawback. The geometric sextupole magnets introduce additional non-linearities themselves.

Nevertheless, the inclusion of geometric sextupole magnets has been investigated. The effect on the dynamic aperture caused by the additional

12-pole \ 20-pole	50.0	25.0	12.5	10.0	7.5	5.0
10.0	26.13	30.27	33.35	33.96	34.25	34.84
7.5	26.47	30.78	34.26	34.88	35.08	35.57
5.0	26.88	31.52	35.15	35.80	35.99	36.19

Table 5.6: Independent reductions of 12- and 20-pole quadrupole field components at $1.5\,GeV/c$. The relative field errors include the 10% increase and are given in units of 10^{-4}.

non-linearities is worse than the gain for the sextupole resonances. Furthermore, the gain itself is small since the chromaticity correction scheme performs well enough to make sextupole resonances a minor problem. The main problem concerning resonances is related to the 12- and 20-pole field components of the quadrupole magnets. That means that the investigation of a multipole correction scheme has to be delayed until the design of the quadrupole magnet will have been finished.

5.7 Discussion of the results

The reduction of the sextupole field component of the dipole magnets made a chromaticity correction feasible. The developed chromaticity correction scheme does hardly affect the dynamic aperture of the $\gamma_{tr} = 6.2$ lattice. The $\gamma_{tr} = 13.3$ lattice is stronger influenced by the sextupole magnets than the $\gamma_{tr} = 6.2$ lattice. The beta functions and phase advances between sextupole magnets do not fit as good as for the $\gamma_{tr} = 6.2$ lattice and compensating sextupole magnet pairs cannot be found easily. However, the dynamic aperture restrictions caused by the sextupole magnets can be decreased with the grouping into four families.

Nevertheless, the main restrictions of the dynamic aperture is caused by field errors of the quadrupole magnets. Thus an investigation was carried out concerning the improvement of the dynamic aperture. Both investigated ion optical settings, the $\gamma_{tr} = 6.2$ and the $\gamma_{tr} = 13.3$ lattice, provide at least in the short term regime a dynamic aperture which is larger than the geometrical acceptance limit. The acceptance limit of the dynamic aperture itself depends on the beta functions and the dispersion. While the dynamic aperture for the $\gamma_{tr} = 6.2$ lattice is limited horizontally only, it is almost equal for both transverse directions for the $\gamma_{tr} = 13.3$ lattice.

The change of tunes and the reduction of field errors were successfully applied and led to an overall increase of the dynamic aperture by roughly a factor two. Based on the reduction of the sextupole field component of the dipole magnets, a reduction of the dominating field errors (the 12- and 20-pole field components) of a factor five appeared to be reasonable. Further improvements of the field errors led to an additional increase of the dynamic aperture. For the $\gamma_{tr} = 13.3$ lattice a different choice of tunes is crucial since the design tunes provide an area of long term stability which is less than $\frac{1}{4}\sigma$, a value which is not sufficiently large. Without any optimization of field errors, this area could be increased to 3 to $4\,\sigma$ just by choosing a different tune setting.

In general, it can be stated that after correction the area with long term stability became large enough to accept the necessary beam width including the specified closed orbit deviations of $5\,mm$. This implies that the closed orbit should be corrected all the time even during acceleration.

Chapter 6

Summary and outlook

Simulations of the closed orbit have shown that an uncorrected closed orbit in the HESR is larger than the geometric acceptance limited by the beam pipe. Therefore, a closed orbit correction scheme consisting of beam position monitors and closed orbit correction dipole magnets has been developed and verified by numerical simulations. The scheme fulfills the requirements of a resulting closed orbit of $5\,mm$ realized with a maximum correction strength of $1\,mrad$. Local closed orbit bumps, e.g. at the target and at the injection injection have been checked to provide the necessary flexibility.

Furthermore, the effect of the electron cooler's toroid magnets have been investigated and the deflection of the circulating antiproton beam caused by the toroid magnets calculated. The location of compensation dipole magnets and their necessary strength have been determined.

The orbit correction method using the orbit response matrix could be verified at the Cooler Synchrotron COSY. The measurement showed good agreement with the ion optical model of COSY. Although the closed orbit correction at COSY was not as successful as it will have to be for the HESR, the limiting factors have been identified and can be overcome by a different setup of the electron cooler compensation bump.

A chromaticity correction scheme for the HESR has been developed and optimized using dynamic aperture methods. A splitting of the two sextupole families into four families (two horizontal and two vertical) leads to further improvement through an increase of the dynamic aperture. In this context it became evident that the current design of the dipole mangets contained in the upper field range a large sextupole field component. The chromaticities were affected strongly by this sextupole field component and became too large to be correctable. Therefore, the dipole magnet design was optimized by a modification of the iron yoke.

With the inclusion of field errors of dipole and quadrupole magnets, betatron resonances have been simulated. Since the quadrupole magnet design is not finished yet, possible multipole optimizations have been investigated. The 12- and 20-pole field components have been identified

as a major limitation. Furthermore, tune scans revealed areas with large dynamic aperture and presented a global overview of the strongest resonances in the resonance web. The frequency map analysis together with the diffusion coefficient provided additional information about long-term stability and the local resonance structure. This information has been used to improve the tune settings of the HESR. The dynamic aperture was increased by roughly a factor two with reasonable reductions of field errors and different choices of tunes. In order to prevent beam loss due to resonances during injection, acceleration, and storage, closed orbit corrections have to be applied at all times to keep the beam within the specified limits.

In future, dynamic aperture calculations and frequency map analysis for COSY will provide insight into the non-linear motion and the resonance structure. A related optimization strategy could also improve experimental conditions e.g. for spin-filter experiments.

The investigation of a multipole correction scheme for the HESR has to be carried out after the quadrupole magnet design is finished. The latest developments and improvements in the field of supercomputing offer the opportunity to investigate long-term stability while overcoming the limitations of dynamic aperture calculations which were necessary for the thesis work. Other effects for example space charge forces or the non-linear forces created by the electron cooler beam should be taken into account. Since these other effects may act on longer time scales, the long term dynamic aperture has be investigated together with its logarithmic dependence on the number of turns.

List of Tables

3.1 Beam parameter for the injection, requirements of PANDA, and both modes of operation 32

4.1 Alignment errors of elements 39
4.2 Measurement accuracy of beam position monitors 41
4.3 Statistical summary of closed orbit correction simulations 43
4.4 Preferred beta functions at electron cooler 48
4.5 Design parameters of electron cooler toroid magnets . . . 48
4.6 Tune settings during experiment 49

5.1 Relative field errors of the bending dipole magnet 57
5.2 Relative field errors of COSY quadrupole magnets 58
5.3 Statistics of dynamic aperture calculations of $\gamma_{tr} = 6.2$ lattice with 50 different seeds 69
5.4 Dynamic aperture calculated with 12- and 20-pole quadrupole field components at $15\,GeV/c$ 73
5.5 Statistics of dynamic aperture calculations for the $\gamma_{tr} = 13.3$ lattice for tunes $Q_x = 7.637$, $Q_y = 7.647$ with 100 different seeds 78
5.6 Independent reductions of 12- and 20-pole quadrupole components at $1.5\,GeV/c$ 79

List of Figures

2.1 Co-moving coordinate system 4
2.2 Phase space ellipse of the motion of a single particle for one transverse plane 9
2.3 Schematic view of an electron cooler 15

3.1 Schematic view of the FAIR site 25
3.2 Schematic view of HESR lattice 28
3.3 Layout of the HESR electron cooler 33
3.4 Ion optics of the HESR for both lattices ($\gamma_{tr} = 6.2$ and $\gamma_{tr} = 13.3$) 34
3.5 Schematic overview of COSY 36

4.1 Example of uncorrected closed orbits in the vertical plane with ten different seeds 40
4.2 Example of corrected closed orbits in vertical plane with ten different seeds 44
4.3 Histograms of maximum deviation of corrected closed orbits 45
4.4 COSY ion optics with $D \neq 0$ in straights 50
4.5 Closed orbit correction for COSY 52

5.1 Tune scan for $\gamma_{tr} = 6.2$ and $\frac{\Delta p}{p} = 0$. 60
5.2 Tune scan with fixed tunes for the $\gamma_{tr} = 6.2$ lattice 62
5.3 Frequency map and corresponding dynamic aperture for $\gamma_{tr} = 6.2$ lattice with $\frac{\Delta p}{p} = 0$ at design tune 64
5.4 Horizontal phase space plot for $\gamma_{tr} = 6.2$ lattice at design tunes 65
5.5 Enlarged view on main parts of frequency map of Figure 5.3a 66
5.6 Dynamic aperture of $\gamma_{tr} = 6.2$ lattice with $\frac{\Delta p}{p} = +3 \cdot 10^{-4}$ 67
5.7 Dynamic aperture of $\gamma_{tr} = 6.2$ lattice with $\frac{\Delta p}{p} = -3 \cdot 10^{-4}$ 68
5.8 Folding of frequency map for $\frac{\Delta p}{p} = -3 \cdot 10^{-4}$ and $\gamma_{tr} = 6.2$ 69
5.9 Distortion of resonance lines in the dynamic aperture plot of $\gamma_{tr} = 6.2$ lattice for $\frac{\Delta p}{p} = -3 \cdot 10^{-4}$ 70
5.10 Dynamic aperture for $\gamma_{tr} = 6.2$ lattice with different tunes 72
5.11 Dynamic aperture of $\gamma_{tr} = 6.2$ lattice with reduced quadrupole errors at design tune 74

5.12 Tune scan for $\gamma_{tr} = 13.3$ lattice 76
5.13 Dynamic aperture of $\gamma_{tr} = 13.3$ lattice for on-momentum particles at design tune 77
5.14 Dynamic aperture of the $\gamma_{tr} = 13.3$ lattice for tunes $Q_x = 7.637$, $Q_y = 7.647$ 78

Bibliography

[1] *An International Accelerator Facility for Beams of Ions and Antiprotons - Conceptional Design Report*, , 2001
URL `http://www.gsi.de/GSI-Future/cdr/`

[2] *An International Accelerator Facility for Beams of Ions and Antiprotons - Baseline Technical Report*, , Sep 2006
URL `http://www.gsi.de/fair/reports/btr.html`

[3] R. Maier et al., *HESR (normal conducting version with dispersion suppressor)*, 3.1, HESR Consortium, 2008

[4] PANDA collaboration, *Physics Performance Report for: PANDA, Strong Interactions Studies with Antiprotons*, Technical Report, 2009, arXiv:0903.3905v1 [hep-ex]

[5] K. Kilian et al., *Cooler Synchrotron COSY-Jülich*, 1990, user guide

[6] R. Maier et al., *Cooler Synchrotron COSY*, Nuclear Physics A, 626:pp. 395c – 403c, 1997

[7] H. Wiedemann, *Particle Accelerator Physics I + II*, Springer, 2003, ISBN 3–540–00672–9

[8] R. Gupta et al., *RHIC IR quadrupoles and field quality state of the art in superconducting accerlerator magnets*, in *Proceedings of the 1999 Particle Accelerator Conference PAC99*, pp. 185–187, New York, 1999

[9] M. Livingston and J. Blewett, *Particle accelerators*, McGraw-Hill, New York, 1962

[10] F. Iselin, *The MAD Program Physical Methods Manual*, 1994
URL `http://cern.ch/Hans.Grote/mad/mad8/doc/phys_guide.ps.gz`

[11] M. Sands, *The Head-Tail Effect*, SLAC-TN-69-8 and 10, SLAC National Accelerator Laboratory, Menlo Park

[12] S. Guiducci, *Chromaticity*, in *CERN Accelerator School*, CERN 94-01, Jyväskylä, 1994

[13] R. Talman, *Single particle motion*, in *Frontiers of Particle Beams; Observation, Diagnosis and Correction*, volume 343 of *Lecture Notes in Physics*, Springer, New York, 1988

[14] H. Koziol, *Beam diagnostics for accelerators*, in *CERN Accelerator School 94-01*, volume 2, pp. 565–600, 1994

[15] G. H. Hoffstaetter et al., *Orbit-Response Matrix Analysis at HERA*, in *Proceedings of the 2002 European Particle Accelerator Conference EPAC02*, pp. 407–409, Paris, 2002

[16] S. Møller, *Cooling techniques*, in *CERN Accelerator School 94-01*, volume 2, pp. 601–618, 1994

[17] D. Reistad, The Svedberg Laboratory, *private communication*

[18] K. Erdmann and M. J. Wildon, *Introduction to Lie Algebras*, Springer, 2006

[19] L. Laslett, *On Intensity Limitations Imposed by Transverse Space-Charge Effects in Circular Accelerators*, BNL Report, BNL-7534, 1963, reprint in LBL PUB-616 (1987)

[20] A. Luccio and N. D'Imperio, *Simbad User's Manual Version 1.36*, C-A/AP/222, Brookhaven National Labaratory, Upton, NY, 2005

[21] J. Galambos et al., *ORBIT - A Ring Injection Code with Space Charge*, in *Proceedings of the 1999 Particle Accelerator Conference PAC99*, New York, 1999

[22] H. Grote and F. Iselin, *The MAD (Methodical Accelerator Design) program Version 8.19, User's Rerence Manual*, CERN/SL/90-13, Geneva, 1996

[23] *MAD-X, Methodical Accelerator Design*
URL `http://mad.web.cern.ch/mad/`

[24] J.-P. Koutchouk, *The LHC Dynamic Aperture*, in *Proceedings of the 1999 Particle Accelerator Conference PAC99*, pp. 372–374, New York, 1999

[25] J. Bengtsson, *The Sextupole Scheme for the Swiss Light Source (SLS): An Analytic Approach*, SLS Note 9/97, Paul Scherer Institut (PSI), Villingen, 1997

[26] L. Nadolski and J. Laskar, *Review of single particle dynamics for third generation light sources through frequency map analysis*, Phys. Rev. ST Accel. Beams, 6(11):p. 114801, Nov 2003

[27] N. Nekhoroshev, *An Exponential Estimate of the Time of Stability of Nearly-Integrable Hamiltonian Systems*, Russian Mathematical Surveys, 32, 1977

[28] M. Giovannozzi et al., *Inverse Logarithm Decay of Long-Term Dynamic Aperture in Hadron Colliders*, in *Proceedings of the Particle Accelerator Conference PAC97*, pp. 1445–1447, 1997

[29] V. I. Arnold et al., *Mathematical Aspects of Classical and Celestial Mechanics*, Springer, Berlin, 2nd edition, 1991, ISBN 3-540-61224-6

[30] F. Schmidt, *Untersuchung zur dynamischen Akzeptanz von Protonenbeschleunigern und ihre Begrenzung durch chaotische Bewegung*, Ph.D. thesis, 1988, DESY HESR 88-02

[31] B. Chirikov, *A universal instability of many-dimensional oscillator systems*, Physics Reports, 52(5):pp. 263 – 379, 1979

[32] J. von Milczewski et al., *Frequency Analysis of 3D Electronic* $1/r$ *Dynamics: Tuning between Order and Chaos*, Phys. Rev. Lett., 78(8):pp. 1436–1439, Feb 1997

[33] Y. Papaphilippou and J. Laskar, *Frequency map analysis and global dynamics in a galactic potential with two degrees of freedom.*, Astronomy and Astrophysics, 307:pp. 427–449, March 1996

[34] J. Laskar, *Secular evolution of the solar system over 10 million years*, Astronomy and Astrophysics, 198:pp. 341–362, June 1988

[35] R. Bartolini and F. Schmidt, *A Computer Code for Frequency Analysis of Non-Linear Betatron Motion*, SL-Note-98-017-AP, CERN, Geneva, Feb 1998

[36] J. Laskar, *Frequency analysis for multi-dimensional systems. Global dynamics and diffusion*, Physica D Nonlinear Phenomena, 67:pp. 257–281, August 1993

[37] R. B. Blackman and J. W. Tukey, *The Measurement of Power Spectra, From the Point of View of Communications Engineering*, chapter Particular Pairs of Windows., pp. 98–99, Dover, New York, 1958

[38] C. Bocchetta, *Frequency Map Analysis*, July 2003, CERN Accelerator School Lectures
URL `http://cas.web.cern.ch/cas/BRUNNEN/Bocchetta1.html`

[39] Y. Papaphilippou, *Frequency Maps of LHC Models*, in *Proceedings of the 1999 Particle Accelerator Conference PAC99*, New York, 1999

[40] PANDA collaboration, *Strong Interaction Studies with Antiprotons*, 2004, Letter-of-Intent

[41] S. Baird et al., *The Antiproton Decelerator: AD*, 1997
URL `http://psdoc.web.cern.ch/PSdoc/acc/ad/Documents/References/documents/ps-97-036.pdf`

[42] R. Johnson, *Initial Operation of the Tevatron Collider*, in *Proceedings of the Particle Accelerator Conference PAC87*, pp. 8–12, Washington, D.C., 1987

[43] R. Stassen et al., *COSY as Ideal Test Facility for HESR RF and Stochastic Cooling Hardware*, in *Proceedings of the Particle Accelerator Conference PAC09*, Vancouver, 2009

[44] H. Poth, *Electron cooling*, in *CERN accelerator school CERN 87–03*, volume 2, pp. 534–569, 1987

[45] D. Möhl, *Stochastic cooling*, in *CERN accelerator school CERN 87–03*, volume 2, pp. 453–533, 1987

[46] ASSIA collaboration, *A Study of SPIN-dependent Interactions with Antiprotons*, Jan 2004, Letter-of-Intent
URL `http://www.gsi.de/documents/DOC-2004-Jan-152-1.ps`

[47] PAX collaboration, *Antiproton-Proton Scattering Experiments with Polarization*, Jan 2004, Letter-of-Intent
URL `http://www.gsi.de/documents/DOC-2004-Jan-125-1.ps`

[48] F. Rathmann et al., *A method to polarize stored antiprotons to a high degree*, Physical Review Letters, 94(1), 2005

[49] A. Lehrach et al., *Polarized beams in the high-energy storage ring of the future GSI project*, in *Proceedings of the 16th International Spin Physics Symposium SPIN2004*, World Scientific, Trieste, 2004, ISBN 981-256-315-6

[50] A. Lehrach, *Strahl- und Spindynamik von Hadronenstrahlen in Mittelenergie-Ringbeschleunigern*, volume 8 of *Schriften des Forschungszentrum Jülich, Reihe Schlüsseltechnologien*, Jülich, 2008, ISBN 978-3-89336-548-7

[51] L. Groening et al., *The 70-MeV Proton Linac for the Facility for Antiproton and Ion Research FAIR*, in *Proceedings of the Linear Accelerator Conference LINAC2006*, pp. 186–188, Knoxville, 2006

[52] K. Blasche et al., *The SIS Heavy Ion Synchrotron Project*, in *Proceedings of the Particle Accelerator Conference PAC85*, volume NS-32 No. 5, IEEE Transactions on Nuclear Science, 1985

[53] P. Spiller et al., *Status of the FAIR SIS100/300 Synchrotron Design*, in *Proceedings of the Particle Accelerator Conference PAC07*, pp. 1419–1421, Albuquerque, 2007

[54] N. Tahir et al., *Design of a Target for Antiproton Production at the Future FAIR Facility*, in *High Energy Density Physics with Intense Ion and Laser Beams: Annual Report 2006*, GSI Report 2007-2, 2007

[55] A. Dolinskii et al., *Optimized lattice for the Collector Ring (CR)*, Nuclear Instruments and Methods in Physics Research A, 532:pp. 483–487, 2004

[56] P. Beller et al., *Layout of an Accumulator and Decelerator Ring for FAIR*, in *Proceedings of the European Particle Accelerator Conference EPAC06*, pp. 199–201, Edinburgh, 2006

[57] U. Bechstedt, *Status of the Main Magnets for HESR*, Talk at 26th HESR Consortium Meeting in Jülich, 2009

[58] U. Bechstedt, Forschungszentrum Jülich, private communication

[59] D. Reistad et al., *Calculations on High-Energy Elentron Cooling in the HESR*, in *Proceedings of the Workshop on Beam Cooling and Related Topics COOL07*, pp. 44 – 48, Bad Kreuznach, 2007

[60] H. Stockhorst et al., *Stochastic Cooling for the HESR at FAIR*, in *Proceedings of the Workshop on Beam Cooling and Related Topics COOL07*, pp. 30 – 34, Bad Kreuznach, 2007

[61] O. Boine-Frankenheim et al., *Cooling equilibrium and beam loss with internal targets in high energy storage rings*, Nuclear Instruments and Methods in Physics Research A, 560(2):pp. 245 – 255, 2006

[62] A. Lehrach et al., *Beam performance and luminosity limitations in the high-energy storage ring (HESR)*, Nuclear Instruments and Methods in Physics Research A, 561(2):pp. 289 – 296, 2006

[63] *HESR ELECTRON COOLER Design study*, Technical Report, The Svedberg Laboratory, 2009

[64] *Electron cooling for HESR, Technical Feasibility of Fast Electron Cooling of Antiproton Beams in the Energy Range 0.8 to 14.5 GeV*, , Novosibirsk, January 2003

[65] *Electron cooling for HESR, Second Progress Report (Technical Feasibility of Fast Electron Cooling of Antiproton Beams in the Energy Range 0.8 to 14.5 GeV)*, , Novosibirsk, 2003

[66] O. Bazhenov et al., *Electron Cooling for HESR, Final Report (Technical Feasibility of Fast Electron Cooling of Antiproton Beams in the energy range 0.8 to 14.5 GeV)*, , Novosibirsk, 2003

[67] H. Stockhorst et al., *Stochastic Cooling for the HESR at the FAIR Facility*, in *Proceedings of the Particle Accelerator Conference PAC09*, 2009

[68] R. Maier, *Cooler synchrotron COSY - performance and perspectives*, Nuclear Instruments and Methods in Physics Research A, 390:pp. 1 – 8, 1997

[69] H. Stockhorst et al., *Progress and Developments at the Cooler Synchrotron COSY*, in *Proceedings of the European Particle Accelerator Conference EPAC02*, pp. 629–631, Paris, 2002

[70] D. Albers et al., *Proton-Proton Elastic Scattering Excitation Functions at Intermediate Energies*, Phys. Rev. Lett., 78(9):pp. 1652–1655, Mar 1997

[71] V. Schwarz et al., *EDDA as internal high-energy polarimeter*, in *Proceedings of the 13th International Symposium on High-Energy Spin Physics SPIN98*, Protvino, 1998

[72] S. Barsov et al., *ANKE, a new facility for medium energy hadron physics at COSY-Jülich*, Nuclear Instruments and Methods in Physics Research A, 462(3):pp. 364 – 381, 2001, ISSN 0168-9002

[73] J. Ritman, *Experiments with the WASA detector at COSY*, Int. J. Mod. Phys., A20:pp. 525–531, 2005

[74] A. Böhm et al., *The COSY-TOF barrel detector*, Nuclear Instruments and Methods in Physics Research A, 443:pp. 238–253, 2000

[75] J. Dietrich et al., *Status of the 2 MeV Electron Cooler for COSY Juelich*, in *Proceedings of the Workshop on Beam Cooling and Related Topics COOL2009*, Lanzhou, 2009

[76] J. Dietrich et al., *Beam Profile Measurements Based On Light Radiation Of Atoms Excited By The Particle Beam*, in *Proceedings of the Particle Accelerator Conference PAC07*, pp. 3955–3957, Albuquerque, 2007

[77] J. Milutinovic and A. Ruggiero, *Closed orbit analysis for RHIC*, in *Proceedings of the 1989 IEEE Partical Accelerator Conference PAC89*, pp. 1370–1372, Chicago, 1989

[78] D. M. Welsch, *Auslegung eines Orbitkorrektursystems für den Hochenergie Speicherring HESR im Projekt FAIR*, 2006, diploma thesis

[79] G. Krol, Forschungszentrum Jülich, private communication

[80] *FAIR Baseline Technical Report - Volume 2: Accelerator and Science Infrastructure*, , Sep 2006
URL `http://www.gsi.de/documents/DOC-2006-Jul-40-1.pdf`

[81] J. Dietrich, Forschungszentrum Jülich, private communication

[82] F. Schmidt, *MAD-X PTC Integration*, in *Proceedings of the 2005 Particle Accelerator Conference PAC05*, pp. 1272–1274, Knoxville, 2005

[83] D. Oellers et al., *Polarizing a stored proton beam by spin flip?*, Physics Letters B, 674(4-5):pp. 269 – 275, 2009

[84] H. J. Stein, *Some characteristics of the electron-cooled proton beam at COSY: A first summary of experimental results from PAX runs Sept. 2008 and Feb. 2009*, April 2009, working draft

[85] J. Safranek, *Experimental determination of storage ring optics using orbit response measurements*, Nuclear Instruments and Methods in Physics Research A, 388:pp. 27–36, 1997

[86] V. Ziemann, *Resonances driven by the electric field of the electron cooler*, 1998, The Svedberg Laboratory, TSL-Note 98-43

[87] S. Sorge et al., *Studies of non-linear and collective effects relevant for HESR*, 2007, GSI Scientific Report 2006, GSI Report 2007-1

[88] D. M. Welsch et al., *Closed Orbit Correction and Sextupole Compensation Schemes for Normal-conducting HESR*, in *Proceedings of the European Particle Accelerator Conference EPAC08*, pp. 3161–3163, Genoa, 2008

[89] G. Franchetti, Helmholtzzentrum für Schwerionenforschung, private communication

[90] J. de Villiers et al., *Numerical Field Analysis of the HESR Dipole Magnet in 3D*, 2008, Internal Report

[91] J. Laskar, *Frequency Map Analysis and Particle Accelerators*, in *Proceedings of the Particle Accelerator Conference PAC03*, pp. 378–382, 2003

[92] Y. Luo et al., *Measurement and Correction of Third Resonance Driving Term in the RHIC*, in *Proceedings of 2007 Particle Accelerator Conference PAC07*

Acknowledgments

First of all, I want to express my deep gratitude to my doctoral referee Prof. Dr. Rudolf Maier. I am more than thankful to him for the great opportunity to do research and write my dissertation at the institute for nuclear physics of the Forschungszentrum Jülich. His excellent support and his trust in my capabilities and work made this thesis possible.

I thank Prof. Dr. Jens Bisplinghoff who kindly accepted to be co-referee for my thesis.

I am deeply grateful to my supervisor Priv.-Doz. Dr. Andreas Lehrach. His excellent supervision and his constructive criticism as well as his constant readiness for inspiring discussions have been essential for my thesis work. His guidance was substantial for my scientific advancement.

I have enjoyed being a member of the institute for nuclear physics and would like to thank all of its members for the friendly working atmosphere. I am especially thankful to Dr. Ulf Bechstedt, Dr. Klaus Bongardt, Prof. Dr. Dr. h.c. Jürgen Dietrich, Dr. Bernd Lorentz, Dr. Dieter Prasuhn, Prof. Dr. Yury Senichev, Dr. Rolf Stassen, Dr. Hans-Joachim Stein, Dr. Hans Stockhorst, and Dr. Raimund Tölle for their assistance, for the many fruitful discussions, and for providing inspirations.

I am also indebted to Dr. Alfredo U. Luccio and Nicholas L. D'Imperio who provided the tracking code SIMBAD as well as useful information and their help.

I sincerely thank Priv.-Doz. Dr. Frank Rathmann for provding the possibility to benchmark the closed orbit correction method at COSY during a PAX beam time.

My thanks goes also to Dr. Guiliano Franchetti for his help and for introducing me to dynamic aperture calculations.

I am very thankful to Dr. Andrea Raccanelli for proof-reading my thesis.

Finally, I express my deepest thanks to my wife Britta and to my son Max for their love, encouragement, support, and patience.